POLITECNICO DI TORINO

Master's Degree in Nanotechnologies for ICTs

Academic Year 2020/2021
December

Graphene-based and Metal-based Electrodes: A comparative study for molecular electronics.

Master's Degree Thesis

Supervisors:
Prof. Mariagrazia GRAZIANO
Prof. Gianluca PICCININI
Engr. Chiara Elfi SPANO
Engr. Fabrizio MO

Candidate:
Shoaib MANSOORI
276858

Summary

Electronic devices are getting smaller and smaller. Device sizes are approaching the molecular and atomic scale limits. The development of new concepts and techniques to control matter at the single-molecule scale is being aided by the growth of a new field known as molecular electronics.

Molecular electronics is based on controlling the conduction in a molecule that is placed between two electrodes. Molecules have small dimensions in the range of nanometers and are available at low cost. Gold has been widely used as an electrode material for studying molecular devices along with other metals like silver, copper, and titanium. But with the advent of graphene as a promising material, using graphene-based electrodes in molecular electronics is becoming compelling.

Two-dimensional (2D) materials are used in thin-film electronic devices and graphene being a two-dimensional material along with superior strength and conduction properties make it an attractive material for creating 2D molecular devices. Metal electrodes are used because of their property of being a good conductor of electricity but graphene which is based on a non-metal carbon has conduction superior to metals. Besides the current literature containing results showing different conduction features of different molecules still lacks systematic studies on the influence of different contacts on transport. Few studies proved that different contact materials significantly change the transport properties in molecular devices. The aim of this thesis is thus to systematically study and test the conduction properties of graphene-based molecular wires and compare them to the metal electrodes.

The thesis starts by opening a description of the Density Functional Theory (DFT) that forms the basis of the computational calculations that are performed to investigate the proposed molecular wires based on graphene. The next chapter gives an overview of the quantum transport theory describing the conduction models for systems out of equilibrium. These two theories are combined in a software package QuantumATK which has been the platform used to perform all analysis in this work.

In the next chapter, the reader is introduced to a simple two-terminal molecular wire to give a basic theory on its conduction properties. Then in the next chapter, the discussion focuses on graphene, discussing the structure and conduction properties of graphene along with techniques on graphene nanogap creation.

Finally, the characterization of the proposed structures of a two-dimensional molecular wire based on graphene sheets and zigzag graphene nanoribbon are presented along with the results for metal-based molecular wire. An important outcome of the thesis is that even if intrinsic conduction properties depend on the specific molecular channel, the electrodes systematically show a fingerprint in the conduction properties of the molecular systems. Graphene results in a promising material for electrodes in molecular junctions because the more natural conjugation with organic molecules leads to enhanced ON current of devices.

Acknowledgements

I would like to thank Ph.D students C.E. Spano and F. Mo. Their suggestions has been very helpful when I faced computational issues. Their valuable insights on the obtained results has helped me better understand the concepts present in this work and the final thesis report has also been improved through their suggestions.

I would also like to thank Prof. M. Graziano and Prof. G. Piccinini for accepting me in their group for my master's thesis.

Finally, I would like to thank my beloved family for their daily support

Contents

List of Figures

List of Tables

Chapter 1

Introduction

Large single crystals of semiconducting material can be made using silicon this is one of the greatest advantage of silicon. This is well suited to the methods of electronics manufacturing developed over the last few decades, where the game is to shape semiconducting material into useful electronic devices. Silicon's dominance is also a result of our ability to understand its material properties and exploit them to create useful devices. Motivated by practical applications, the advanced silicon technology underwent and is still continuing to undergo a rapid development of miniaturizing the electronic devices over the past decades [**1**].

However, further downscaling cannot meet the higher performance and stable properties any more. This is mainly due to the increasing difficulties and fundamental limitations of that come with miniaturized devices. The design rules for silicon-based integrated circuits were proposed by Gordon E. Moore in 1965 and has been a guide for the semiconductor companies until about 2008 [**2**].

Recently TSMC Corp. has annouced to have a 4nm and 3nm chips by the year 2022[**3**] but it is impossible to shrink the distance between adjacent components forever due to the quantum tunnelling and heat problems. Advances in quantum chemistry and our understanding of solid-state systems have brought us to a point where we are interested in the electronic transport properties of organic molecules that are a few nanometers in size.

Consequently single organic molecules have been considered as a building block of electronic devices and were connected to two metal electrodes by building a metal-molecule-metal (MMM) junction [**4**]. This novel idea is called molecular electronics and has been expected to lead the dimensions of electronic devices to 1 to 3 nm [**5**]. The field of molecular electronics offer not only a way to realize the ultimate miniaturization of electronic devices but also pay the way for understanding charge transfer at molecular level.

The early studies relating to molecular electronics can be traced back to 1970s. Particularly, Mann and Kuhn reported the conductivity measurement though organic monolayers and suggested the electron tunnelling though the monolayer of molecules in 1971 [**6**]. Then in 1974, Aviram and Rater proposed the first theoretical suggestion of applying single molecule circuit to serve as the building block in between of two electrodes [**7**]. Nowadays we also have electrical rectification or diode properties that have been confirmed experimentally [**8**, **9**]. Initially, a main problem was finding a way of attaching molecules to electrodes and making defined electrical measurement through such molecular junctions.

The first significant work relating to the investigation of charge transport properties through single molecular junction was proposed by Mark Reed and James Tour in 1997 [**10**]. In their work they studied a gold-sulfur-aryl-sulfur-gold system using a mechanically controllable break junction with benzene-1,4-dithiol molecules self-assembled onto gold electrodes. This study along with their later works gives us an insight on understanding of how to perform measurements at nanoscale and how electrons flow along the junction.

Scanning tunnelling microscope (STM) and atomic force microscope (AFM) were developed by IBM in Zurich, which paved the way for conductance measurement of single molecules. Further, different techniques were developed using STM and AFM as their basis, for instance, the conducting probe atomic force microscopy (CP-AFM), scanning tunnelling microscopy break junctions (STM BJ) in early 2000s [**11**, **12**, **13**]. The success of these measurement techniques gave rise to a great deal of interests from the scientific community which lead to the true beginning of molecular electronics [**14**].

Studies of solid-state systems sometimes lead to the invention of socially useful devices, the famous example being the transistor. One reason to study molecule conduction is the attempt to make “molecular electronics” - devices that use organic or metallorganic molecules as an integral part of their device structure. There are several reasons why “molecular electronics” would be desirable:

1. Molecules are small. If one, or a few molecules could be used to make a transistor or a sensor, it would be possible to miniaturize electronic components to a few nanometers.

2. Molecules are cheap. Current (2020) cost estimates for a 300 mm wafer production factory are upwards of a billion dollars [**15**]. A lot of this cost stems from the fact that the machines and technology required to create billions of functional devices from silicon that are small (100 nm at present) are expensive. Molecules, on the other hand, are always perfect. If they can be integrated in a useful way into electronic components, presumably the cost of manufacturing them will decrease.

3. Molecules can be found that have special functional properties. Examples of this kind are the materials that go into organic light-emitting diodes, liquid-crystal displays and solar cells.

In this thesis, I will mostly talk about the transport properties of devices made from single molecules. The reader will find a few interesting facts about electron transport through molecules, but nothing that will be useful in the manufacture of socially useful electronic devices.

Due to advancements in theoretical quantum chemistry theoretical models have been developed that make it possible to study electrical properties of single molecule transistors. Advanced tools like QuantumATK are available that combine density functional theory (DFT) with Keldysh-Green formalism for non-equilibrium systems. In this work this tool has been used extensively for all the analysis.

Chapter 2

Density Functional Theory

1 Introduction

Many theories have arisen in an attempt to examine and comprehend the electrical characteristics of molecules; one of the most prominent and common of these theories is density functional theory (DFT). DFT is now widely regarded as a powerful method for calculating the quantum state of atoms, molecules, and solids, as well as ab-initio molecular dynamics. Thomas and Fermi[**16**] proposed an early and approximate version of density functional theory in 1927, shortly after the creation of quantum mechanics. Later, using quantum mechanics as a starting point, Hohenberg, Kohn, and Sham created a density functional theory of the quantum ground state that outperformed both Thomas-Fermi and Hartree-Fock theories, which opened a wide door to applications for realistic physical systems [**17**, **18**]. Density functional theory (DFT) has advanced dramatically since then, and it is now one of the most important tools in theoretical physics and molecular chemistry.

1.1 The Many-Body Problem

This is a technique for resolving any system with a lot of interacting particles. In a microscopic system consisting of charged nuclei surrounded by electron clouds, the Schrödinger equation defines interactions such as electron-nuclei, electron-electron, nuclei-nuclei, and electron correlations.

The complete Hamiltonian operator representing these interactions in a generic system is:

$$H = \sum_{n} -\frac{\hbar^2}{2m_e}\nabla^2_{r_n} + \frac{1}{8\pi\epsilon_0}\sum_{n\neq m}\frac{e^2}{|r_n - r_m|} - \sum_{n}\frac{\hbar^2}{2m_n}\nabla^2_{r_n}$$

$$+\frac{1}{8\pi\epsilon_0}\sum_{n\neq m}\frac{Z_n Z_m e^2}{|R_n - R_m|} - \frac{1}{4\pi\epsilon_0}\sum_{nm}\frac{Z_m e^2}{|r_n - R_m|} \tag{2.1}$$

The mass, atomic number, and position of the n-th atom in the solid are represented by m_n, Z_n, and R_n respectively. The characters r_n, r_m, m_e signify the position of the $n-th$ electron and the mass of a single electron. The electron kinetic energy, electron-electron interactions, nucleon kinetic energy, nucleon-nucleon interactions, and electron-nucleon interactions are the five elements of this Hamiltonian. The mass of nucleons is around a few orders of magnitude greater than that of electrons, and in terms of velocities, the nuclei might be considered a classical particle that creates an external potential, while electrons are exposed to this potential as quantum particles.

Equation (2.1) can then be expressed as follows, using the Born-Oppenheimer approximation [**19**] and the assumption that the nucleon wavefunction is independent of the electron position:

$$H = T_e + U_{e-e} + V_{e-nuc} \tag{2.2}$$

The first part of equation (2.2) presents the kinetic energy of all electrons, which is described by:

$$T_e = \sum_n \frac{\hbar^2}{2m_e}\nabla_n^2 \tag{2.3}$$

The electron-electron interaction is represented in the second part of equation (2.2), which is given by:

$$U_{e-e} = \sum_{n,m,n\neq m}\frac{e^2}{4\pi\epsilon_0}\frac{1}{|r_n - r_m|} \tag{2.4}$$

U_{e-e} describes the sum of all potentials acting on a given electron at position r_n by all other electrons at position r_m

The third part of equation (2.2) describes the interactions between electrons and nuclei, which is expressed by;

$$V_{e-nuc} = \sum_N \sum_n \nu_{nuc}(r_n - R_N) \tag{2.5}$$

V_{e-nuc} interaction between electrons and nuclei; it depends on the positions of electrons r_n and nuclei R_N The electron and nucleon degrees of freedom can be dissociated using the Born-Oppenheimer approximation [**19**].

1.2 The Hohenberg-Kohen theorems

Essentially, the development of density functional theory (DFT) was based on two deceptively simple theorems proposed and proved by Hohenberg and Kohn in 1964 [25]. These two powerful statements are the theorems: Theorem No. 1: The density of any system of interacting particles in an external potential V_{ext} is unique. In other words, the density's external potential is a one-of-a-kind function. Assume that two external potentials $V_{ext}^{(1)}$ and $V_{ext}^{(2)}$ differ by more than a constant and give rise to the same ground state density, $\rho_{0(r)}$ to prove this theorem. It is obvious that these potentials belong to various Hamiltonians, which are denoted $H^{(1)}$ and $H^{(2)}$ and They produce different ground-state wavefunctions $\psi^{(1)}$ and $\psi^{(2)}$ Since $\psi^{(2)}$ is not a ground state of $H^{(1)}$ so:

$$E^{(1)} = \langle\psi^{(1)}|H^{(1)}|\psi^{(1)}\rangle < \langle\psi^{(2)}|H^{(1)}|\psi^{(2)}\rangle \tag{2.6}$$

and, similarly:

$$E^{(2)} = \langle\psi^{(2)}|H^{(2)}|\psi^{(2)}\rangle < \langle\psi^{(1)}|H^{(2)}|\psi^{(1)}\rangle \tag{2.7}$$

Assuming that the ground states are non-degenerate, one could rewrite equation (2.6) as follows:

$$\begin{aligned}\langle\psi^{(2)}|H^{(1)}|\psi^{(2)}\rangle &= \langle\psi^{(2)}|H^{(2)}|\psi^{(2)}\rangle + \langle\psi^{(2)}|H^{(1)-H^{(2)}}|\psi^{(2)}\rangle \\ &= E^{(2)} + \int dr(V_{ext}^{(1)}(r) - V_{ext}^{(2)}(r))\rho_0(r)\end{aligned} \tag{2.8}$$

asumming that $|\psi^{(1)}\rangle$ has the same density $\rho_0(r)$ as $|\psi^{(2)}\rangle$:

$$\langle\psi^{(2)}|H^{(1)}|\psi^{(2)}\rangle = E^{(1)} + \int dr(V_{ext}^{(2)}(r) - V_{ext}^{(1)}(r))\rho_0(r) \tag{2.9}$$

Comibinig the equations we get:

$$E^{(1)} + E^{(2)} < E^{(1)} + E^{(2)} \tag{2.10}$$

This equation proves the two different external potentials cannot produce the same ground-state density.

Theorem II: The density can be used to define a universal functional $F[\rho]$ or the energy $E[\rho]$. The global lowest value of this functional is the precise ground state. In other words, the functional $F[\rho]$ determines the system's ground state energy. The functional $F[\rho]$ would supply the least energy if the input and ground-state densities are the same. As a result, the functional might be minimised by adjusting the density to obtain the external potential's ground-state energy. Consider the formula for the total energy, E, of the system with density ρ to prove the second theorem:

$$E[\rho] = T[\rho] + E_{int}[\rho] + \int drV_{ext}(r)\rho(r) \tag{2.11}$$

The kinetic term, T, and internal interaction of the electrons, E_{int}, depend only on the charge density, and so are universal. The first theorem reported that the ground-state density ρ_0 for a system with external potential V_{ext} wavefunction ψ_0 determines the Hamiltonian of that system, so for any density, ρ and wavefunction, ψ, other than the ground state, it could be found:

$$E_0 = \langle \psi_0 | H | \psi_0 \rangle < \langle \psi | H | \psi \rangle = E \tag{2.12}$$

Hence, the ground-state density, ρ_0, minimizes the functional (equation 2.11). If the functional $T[\rho] + E_{int}[\rho]$ is then by minimizing equation 2.11, the ground-state of the system could be obtained, and then all ground-state characteristics could be calculated, which are the subject of the interest.

1.3 The Kohn-Sham Method

For over fifty years, the Kohn-Sham approach has been employed in solid state physics. By now, the method has gained a large following among physicists and chemists, owing to the development of increasingly accurate density functionals, especially because it allows for accurate treatment of molecular systems in many cases not possible with more traditional quantum mechanical methods [**20**, **21**]. The ground-state density is obtained by computing the ground-state energy, as mentioned in the previous section. The exact form of the functional indicated in equation (2.11), however, is unknown. In general, the kinetic term as well as the internal energy of interacting particles cannot be described as density functionals. Kohn and Sham proposed in 1965 [3] that the original Hamiltonian of the system may be replaced by an effective Hamiltonian of non-interacting particles in an effective external potential, resulting in the same ground state density as the original system [**22**, **23**]. The Kohn-Sham ansatz's energy functional form is:

$$E_{KS}[\rho] = T_{KS}[\rho] + \int dr V_{ext}(r)\rho(r) + E_H[\rho] + E_{xc}[\rho] \tag{2.13}$$

The kinetic energy of the non-interacting system is T_{KS}. For the interacting system, the kinetic energy, T, in equation (2.11) was employed. The exchange correlation, Exc, functional, which is specified in equation 1, is responsible for this discrimination (2.15). E_H is the Hartree functional, which uses the Hartree-Fock technique to characterise the electron-electron interaction.

$$E_H[\rho] = \frac{1}{2} \int \frac{\rho(r)\rho(r')}{|r - r'|} dr dr' \tag{2.14}$$

This is an approximated version of the previously defined internal electron interaction, $Eint$. The discrepancy, once again, referred to the exchange correlation,Exc. As a result, Exc was used to indicate the discrepancies between the exact and approximate solutions for the kinetic energy and electron-electron interaction components.

$$E_{xc}[\rho] = (E_{int}[\rho] - E_H[\rho]) + (T[\rho] - T_{KS}[\rho]) \tag{2.15}$$

Consequently, the Kohn-Sham method could be a powerful approach to obtain an accurate ground-state density if the exchange correlation, E_{xc} is known precisely.

1.4 The Exchange Correlation Functionals

Finding correct approximations to the exchange correlation energy, E_{xc}, is the most difficult task in Kohn-Sham DFT. The best approximation could be created to gain the best knowledge of exact functional [**24**]. Numerous forms have been presented in an attempt to obtain the best approximation for the exchange-correlation functional. This section gives a quick overview of two of the most used approximation methods. The local density approximation (LDA) [**25**] is the first. The generalised gradient approximation (GGA) [**26**] is the second method. When comparing the accuracy of LDA and GGA, it was discovered that GGA is the more accurate approximation since it is based on density and density gradients, but LDA is the simplest because it is based on local density.

Local Density Approximation

The most basic approach is to treat the density as if it were a uniform electron gas. The exchange-correlation energy for a density ρ can be calculated using this approximation, which was first presented by Kohn and Sham [3].

$$E_{xc}^{LDA}[\rho] = \int dr\rho(r)(\epsilon_x^{hom}(\rho(r)) + \epsilon_c^{hom}(\rho(r))) \tag{2.16}$$

The exchange and correlation energy densities for the homogeneous electron gas are denoted by the words ϵ_x^{hom} and ϵ_c^{hom}. In the literature [**27**], the analytical exchange energy, ϵ_c^{hom}, can be found:

$$\epsilon_x^{hom} = -\frac{3}{4\pi}\sqrt[3]{3\pi^2\rho} \tag{2.17}$$

Ceperley and Alder [**28**] used the quantum Monte-Carlo approach to determine the correlation energy ϵ_c^{hom} numerically, then Perdew and Zunger [**29**] fitted the numerical data to analytical equations and discovered:

$$\epsilon_c^{hom} = \begin{cases} -0.048 + 0.031\ln r_s - 0.0116 r_s + 0.002 r_s \ln(r_s) r_s > 1 \\ -\frac{0.1423}{(1+1.9529\sqrt{r_s}+0.3334 r_s)} r_s < 1 \end{cases} \tag{2.18}$$

Here, $r_s = (\frac{3}{4\pi\rho})^{\frac{1}{3}}$ in a homogeneous electron plasma of density, is the radius of a sphere containing one electron. The LDA is typically surprisingly precise, and it produces excellent results in systems like graphene and carbon nanotubes, where the electron density varies slowly. Despite the LDA's exceptional effectiveness [**30**, **31**], caution should be exercised in its application. LDA, for example, predicts an inaccurate ground state for the titanium atom and provides a poor description of hydrogen bonding [**32**, **33**], as well as an incorrect band gap value in semiconductors and insulators [**34**, **35**].

Generalized Gradient Approximation

Because of the drawbacks of the local density approximation (LDA) and the reality that real systems are inhomogeneous, an alternate approximation, the extended gradient approximation, is required (GGA). Because there is no analytical form for the exchange energy in GGA, it has been estimated numerically along with the correlation term. Nowadays, a variety of parameterizations are employed in this approximation; one of the most popular and reliable is the PBE functional form, developed by Perdew, Burke, and Ernzherhof [**36**] in 1996:

$$E_{xc}^{GGA} = E_x^{GGA}[\rho] + E_c^{GGA}[\rho] \tag{2.19}$$

The exchange part is given by:

$$E_x^{GGA}[\rho] = \int \epsilon_x(\rho(r)) V_x(\rho(r)\nabla\rho(r))\rho(r)dr$$

$\mathrm{V}_x(\rho, \nabla\rho) = 1 + k - \frac{k}{1+\frac{\mu s^2}{k}}$(2.20)

Here, k $= 0.804$, $\mu = 0.21951$ and $s = \frac{|\nabla\rho|}{2k_F\rho}$is the dimensionless density gradient and k_F is the Fermi wavelength and $V_x(\rho, \nabla\rho)$ represents the enhancement factor. The correlation energy form is given by:

$$E_c^{GGA}[\rho] = \int \rho(r)[\epsilon_c(\rho(r)) + F(\rho(r), \nabla\rho(r))]dr \tag{2.21}$$

$$F(\rho(r), \nabla\rho(r)) = \frac{2}{a_0} \ln[1 + \frac{\beta t^2}{\gamma}(\frac{1 + At^2}{1 + At^2 + A^2t^4})],$$

$$A = \frac{\beta}{\gamma}\frac{1}{e^{\epsilon_c(\rho)/\gamma - 1}}, \beta = 0.066725, \gamma = \frac{(1 - \ln 2)}{\pi^2}, a_0 = \frac{\hbar}{m^2}$$

and the dimensionless gradient is $\frac{|\nabla\rho|}{2k_{TF}\rho}$ where $k_{TF} = \frac{\sqrt[3]{\frac{12}{\pi}}}{\sqrt{r_s}}$ is known as the Thomas-Fermi screening wavelength and r_s is defined as the local Seitz radius. The PBE-GGA functional has had a huge impact, both in terms of real calculations and as a foundation for functionals with greater derivatives and accurate exchange [**37**].

Chapter 3

Quantum transport theory

1 Transport regimes

Existing theories of electrical transport have been pushed to their limits by the development of electronic devices on a single-molecule scale. The quantum property of the electron must be considered due to the small size of these devices. In quantum mechanics, the electron acts like waves, which can cause interference.

Different methodologies have been employed for each transport regime in the realm of electron transport in mesoscopic and nanoscopic systems. As a result, we must first specify the transport regime for each problem before proceeding with the transport calculation. The momentum relaxation length, L_m, and the phase relaxation length, L_ϕ [**38**], are two distinctive lengths used to distinguish the transport regime.

The phase relaxation length (or electron mean free path) is the average distance an electron may travel before losing its original phase, whereas the momentum relaxation length (or electron mean free path) is the average distance an electron can travel before losing its original momentum. If the device's length, L, is significantly greater than L_m and L_ϕ, the conductance is determined by the length of the wire, according to Ohm's law. That is why it is known as the ohmic regime.

We can divide electron transport into three transport regimes based on two characteristic lengths:

(1) Ballistic transport regime, $L << L_m, L_\phi$

Electrons can readily propagate from one lead to the other without scattering in this transport regime. In the electron transport process via a device, there is no appreciable momentum or phase relaxation. The backscattered electron at the contact location can cause resistance. Ballistic conduction is most commonly observed in quasi-1D structures with quantized conductance ($G_0 = 2e^2/h$, where e is the electron charge and h is the Plank constant), such as metallic nanowires or carbon nanotubes. The length of such a device has no influence on its conductivity.

(2) Elastic and coherent transport regime, $L < L_\phi$

Electrons move too quickly for molecular vibration to interact with a short molecule. As a result, the energy of electrons is retained, but the phase memory of dispersed wave functions is preserved. The transmission loss caused by elastic scattering does not affect L_ϕ, but simply L_m.

(3) Inelastic and incoherent transport regime, $L > L_\phi$

In a long molecule bridge, the incoherent transport regime can be seen in general. Because electrons have such a long traverse time, they might interact with other electrons or phonons, resulting in phase-breaking or incoherent scattering. As a result, along with the change in electron momentum, the phase of the electron waves is lost. Instead of the molecule-lead contact, the molecular chain's dynamic plays an important part in transmission.

The Landauer method and the Non-Equilibrium Green's Function (NEGF) method are two extensively used approaches for studying the transport problem. The Landauer approach may be used to represent noninteracting electron transport in the ballistic or coherent transport regimes, whereas the NEGF approach is a more complex method that can be utilised in all three. The Landauer and NEGF approaches will be briefly described in the following parts.

2 Landauer approach

We can visualize a system of two macroscopic leads connecting to the molecule or nanoscale structure in the Landauer technique. The system comprises of an electron reservoir-connected central area (C) sandwiched between left (L) and right (R) leads. The left and right leads are held at two separate electrochemical potentials, μ_L and μ_R, in most situations, where $\mu_L = \mu_R$ at zero applied voltage. The current flow is caused by the electrochemical potential difference between two leads. This difference is adjusted by applied bias voltage.

The problem can be understood as a scattering problem in such a geometrical model. A potential connecting the two leads scatters an incident wave function travelling along the core region, which is subsequently transmitted to the other lead. The current flow, according to Landauer, is the chance of an electron being transported from one lead to the other. Here a straightforward technique to derive the Landauer formula is discussed. This method's rigorous derivation may be found in Ref. [**39**, **40**].

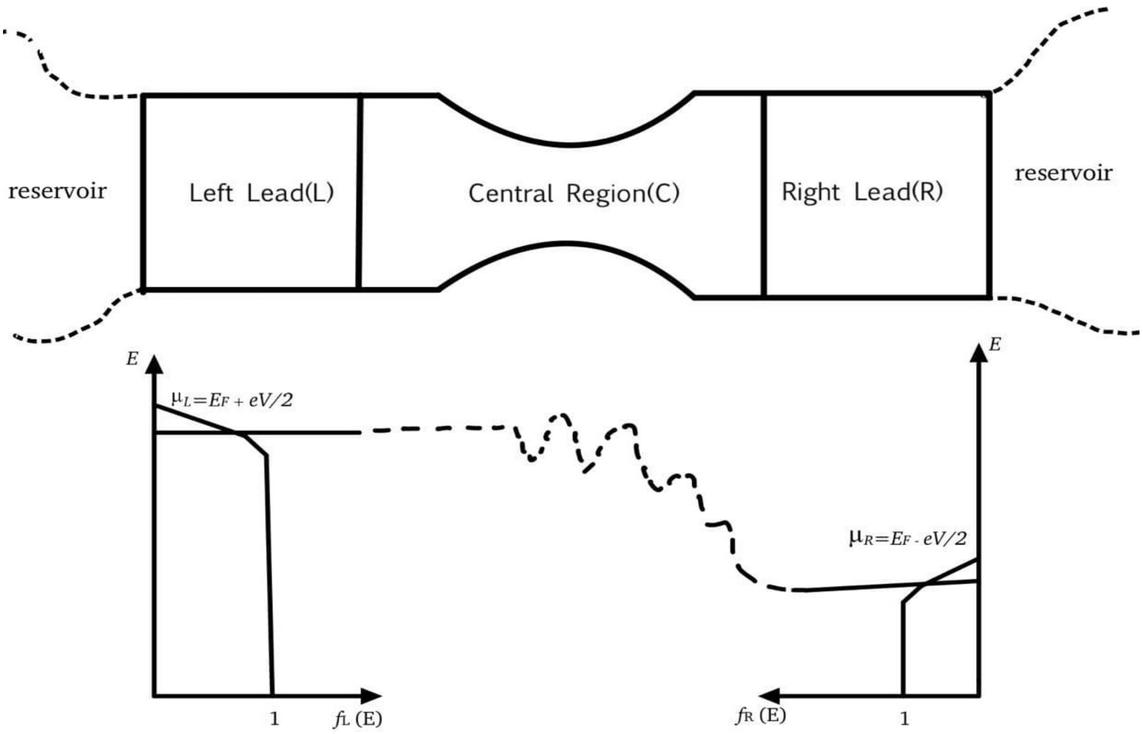

Figure 3.1: Schematic of the 'open system' described within the Landauer approach. The setup of the Landauer approach: left and right leads (L,R) are connected to two reservoirs held in equilibrium at two different electrochemical potentials (μ_L, μ_R). Both leads are connected to a central region (C), in which scattering can take place. The electrochemical potential is almost flat inside the leads, and the potential drop occurs across the junction.

Consider a one-dimensional wire with a length L that connects two leads.It is presumed that this system is in the ballistic transport regime. States in the direction normal to propagation are quantized in the 1D-wire. Where $f(k)$ is the Fermi distribution function, the electron density per unit length corresponding to a given perpendicular state in the momentum range between k and k+dk, including spin is

$$n(k)dk = 2\frac{1}{L}\frac{L}{2\pi}dk = 2\frac{1}{2\pi}f(k)dk \tag{3.1}$$

where $f(k)$ is the Fermi distribution function.

The leads connected to reservoirs are in equilibrium at finite bias, with Fermi distribution functions $f_L(k)$ and $f_R(k)$ for the left and right leads, respectively. The current that circulates in the system is:

$$I = 2\int_0^\infty ev(k)n(k)dk = 2\int_0^\infty e\frac{\hbar k}{m_e}\left(\frac{f_L(k)}{2\pi} - \frac{f_R(k)}{2\pi}\right)dk, \tag{3.2}$$

where $\nu(k)$ is the electron velocity along the wire and me is the electron effective mass. At the zero temperature, the Fermi distributions are step functions, and the Eq. (3.2) becomes

$$I = 2\int_{\sqrt{2m_e\mu_R}/\hbar}^{\sqrt{2m_e\mu_L}/\hbar} e\frac{\hbar k}{m_e}\frac{1}{2\pi}dk = 2\frac{e^2}{h}\frac{\mu_L - \mu_R}{e} = 2\frac{e^2}{h}V_B, \tag{3.3}$$

where μ_L and μ_R are the electrochemical potential of the left and right leads, respectively. V_B is the bias voltage due to a shift in the electrochemical potentials of both leads, where $\mu_L - \mu_R = eV_B$. From the Eq. (3.3), the maximum conductance of a one conduction channel with two spin states, G_0, is

$$G_0 = \frac{2e^2}{h} = (12.9k\omega)^{-1} \tag{3.4}$$

This is the so-called quantum of conductance. Generally, the nanodevice and its connection to the leads is not ideal due to scattering. Therefore, the formula for the conductance can be written as

$$G_0 = \frac{2e^2}{h}T(E_f) \tag{3.5}$$

where E_F is the Fermi energy of the system. The Eq (3.4) is used for the 1D wire, where there is only one conducting mode in the direction normal to the propagation. For the finite width device, the number of quantum modes carrying electrons is to be considered. The Landauer formula can be generalized to

$$G_0 = \frac{2e^2}{h}\sum_{i,j}T(E_f) \tag{3.6}$$

where T_{ij} is the probability of electrons passing from ith conducting mode at the left of the device to the jth conducting mode at the right of the device. More generally, the current at a finite bias can be expressed as

$$I = \frac{2e}{h}\int_{-\infty}^{\infty} T(E, V_b)[f(E-\mu_L) - f(E-\mu_R)]dE \tag{3.7}$$

According to Landauer formula, Eq. (3.7), only one ingredient required is the energy dependent transmission function. This is typically derived from the Green's function of the central region connected to both leads, as we will discuss in the following section.

3 Non-equilibrium Green function (NEGF)

Because electron transport is studied at the atomic level, integrating the NEGF method with DFT has a significant advantage over other approaches. Many books and papers [**39**, **41**, **42**] describe the NEGF approach in detail. The NEGF method for calculating current-voltage characteristics of molecular devices will be described in general here. The Hamiltonian of the system is determined by starting with the screening approximation and partitioning the system into the central area, left and right leads. The charge density is estimated in a self-consistent manner using the NEGF technique. Each region's wave function in relation to an incoming wave function is described. The section concludes with a discussion of how to use the NEGF method to compute the electron current.

Screening Approximation

Figure 3.2 shows a two-probe system with three parts: semiinfinite left (L) and right (R) leads, as well as the centre region (C). The semi-infinite lead has a regular periodic structure in the transport direction, resulting in the Hamiltonian's infinite dimension. We can divide the effective potential and charge density into the core region and the left/right lead region considered as a bulk system using a screening approximation.

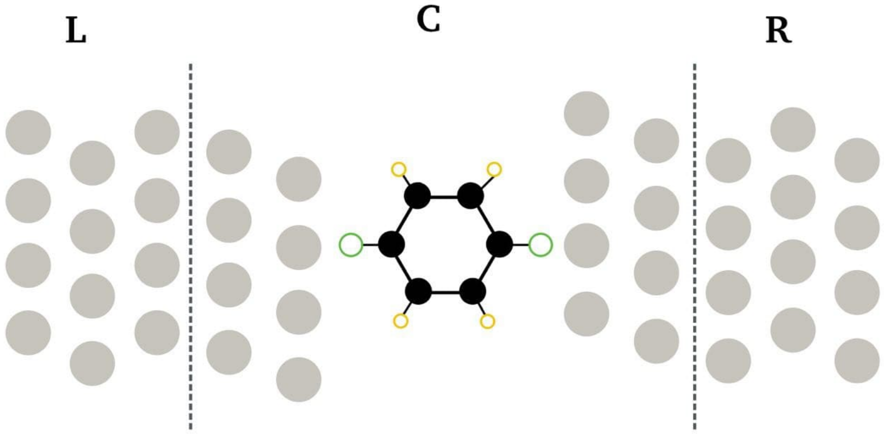

Figure 3.2: Schematic illustration of a two-probe system containing a molecule connected to left (L) and right (R) leads

Surface effects caused by a molecule being perturbed at a contact, such as charge transfer, atomic relaxation, and potential disturbance, are minimised by adding a few layers of leads to the central region, essentially blocking them from the bulk of the electrodes. We may express the whole Hamiltonian as follows using the screening approximation:

$$\begin{pmatrix} H_L & \tau_L & 0 \\ \tau_L^{\dagger} & H_C & \tau_R^{\dagger} \\ 0 & \tau_R & H_R \end{pmatrix} \tag{3.8}$$

The Hamiltonian matrices of the left, centre, and right parts are denoted as H_L, H_C, and H_R, respectively. The interaction between the left lead and the central area is represented by τ_L and the interaction between the right lead and the central area is represented by τ_R. There is no direct tunnelling between leads L and R, we assume. The Schrödinger equation must be solved once the open system has been partitioned into separate sections. The Schrödinger equation is solved using the Non-equilibrium Green function (NEGF) method, which is discussed in the next section.

Green's functions and self energies

The retarded Green's function G corresponding to the Hamiltonian matrix H is defined as:

$$[ES - H]G^R = I \tag{3.9}$$

$$\begin{pmatrix} ES_L - H_L & -\tau_L & 0 \\ -\tau_L^{\dagger} & ES_C - H_C & -\tau_R^{\dagger} \\ 0 & -\tau_R & ES_R - H_R \end{pmatrix} \begin{pmatrix} G_L^R & G_{LC}^R & 0 \\ G_{CL}^R & G_C^R & G_{CR}^R \\ 0 & G_{RC}^R & G_R^R \end{pmatrix} = \begin{pmatrix} 1 & 0 & 0 \\ 0 & 1 & 0 \\ 0 & 0 & 1 \end{pmatrix} \tag{3.10}$$

After solving the above matrix we can obtain the following equations:

$$G^R = [ES_C - H_C - \Sigma_L - \Sigma_R]^{-1} \tag{3.11}$$

where,

$$\Sigma_L(E) = \tau_L^{\dagger} g_L \tau_L \tag{3.12}$$

and

$$\Sigma_R(E) = \tau_R^{\dagger} g_R \tau_R \tag{3.13}$$

We call $\Sigma_{L/R}$ a "self-energy". In Fig. 3.3, the self-energy is linked to the energy level broadening Γ:

$$\Gamma_{L/R}(E) = i[\Sigma_{L/R}(E) - \Sigma_{L/R}(E)^{\dagger}] = -2Im[\Sigma_{L/R}(E)] \tag{3.14}$$

Furthermore, the lifespan of electronic states on molecules is linked to the widening of the molecular level. When the molecule is connected to the leads, electrons can escape into the right or left leads, spending time in the centre area. The widening of electrons is inversely proportional to the lifespan of state: $\tau_{L/R}\Gamma = \hbar$

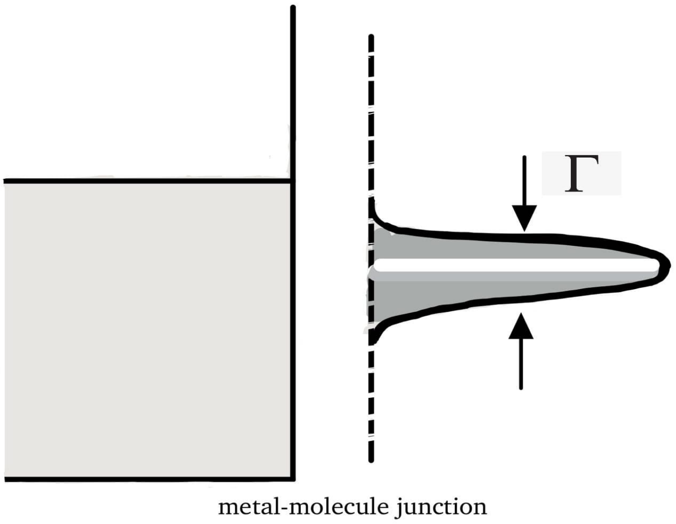

Figure 3.3: The energy level broadening due to the coupling to the contact is given by Γ

According to Eq. (3.11), the infinite-dimensional Hamiltonian is reduced to the central part's dimension, where the self-energies Σ_L and Σ_R incorporate all information about the leads' semi-infinite characteristics. Only the limited component of the right and left leads interact directly with the central section. As a result, we may concentrate just on the centre region's Green's function matrix and consider the influence of semi-infinite leads in terms of effective interaction. The Hamiltonian's effective expression is:

$$H_{eff} = H_C + \Sigma_L(E) + \Sigma_R(E) \tag{3.15}$$

Finally, after a rigorous treatment which can be found in the references the current through the device connected to two contacts at chemical potential μ_R and μ_L is written as:

$$I = \frac{e}{\pi\hbar}\int_{-\infty}^{\infty} Tr(\Gamma_L G^R \Gamma_R G^A)(f(E-\mu_L) - f(E-\mu_R))dE \tag{3.16}$$

This equation has the same form as Landauer formula which means we can rewrite the above equation with the transmission spectrum giving us:

$$I = \frac{e}{\pi\hbar}\int_{-\infty}^{\infty} T(E)(f(E-\mu_L) - f(E-\mu_R))dE \tag{3.17}$$

The quantum transport theories, Landauer theory and non-equilibrium Green's function (NEGF) method, have been introduced in this chapter. In the limit of a coherent transport regime, the NEGF technique may be simplified to Landauer formalism. There are three areas in the system: a left lead, a right lead, and a middle region. To use the NEGF formalism, the Hamiltonian of lead-molecule-lead must be calculated in order to produce single-particle Green functions; hence, DFT is coupled in the selfconsistent NEGF+DFT method. NEGF+DFT is now a robust and rigorous technique that, in many circumstances, provides quantitative agreement with experiments. We can compute the charge density in open systems, as well as the transmission coefficients and current voltage characteristics, using this approach. The NEGF+DFT technique was used to explore the electron transport characteristics of the molecular wire using the QuantumATK Toolkit.

Chapter 4

Brief insight on the Molecular Wire

A molecular wire is a two probe system wherein a single molecule is placed in between two electrodes. A simple diagram of a molecular wire is shown in figure 4.1. Under the influence of an electric field there is a transfer of charge from the left electrode to right electrode which results in the current flow.

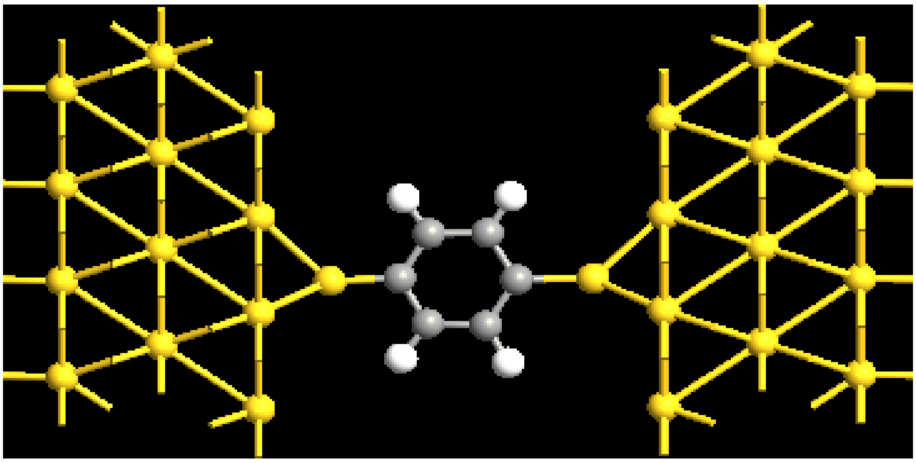

Figure 4.1: A simple molecular wire with gold electrodes and benzene channel

To design and control the charge transport in a molecular wire we need a to understand the theory behind the metal-molecule-metal will be very beneficial. Lets start with a bulk inorganic metal material, an important parameter that we define here is the work function ϕ_B which can be viewed as the amount of work that will be needed to move an electron from metal to a point just outside the solid which is in vacuum. Next the concept of Fermi level, E_f, of the metal which tells us about the occupation of electrons. E_f is at the topmost filled level at 0K and at half filled level for a finite temperature T.

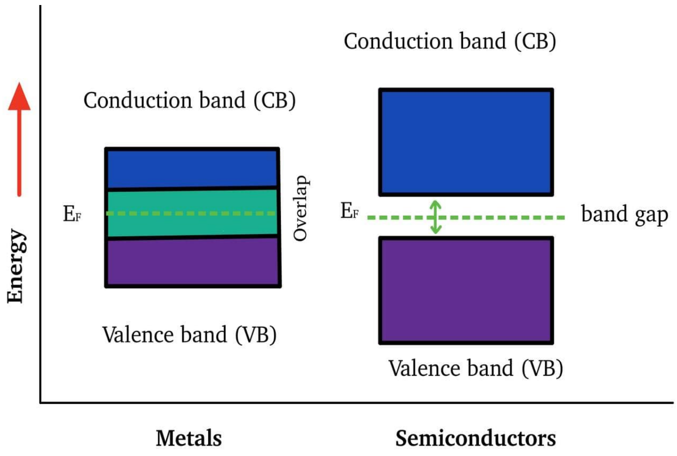

Figure 4.2: The Fermi level of the metals and semiconductors

For a semiconductor material the Fermi level is placed statistically at a distance half way between the valence and conduction band. Then the work function is the difference of energy between E_f and the vacuum level and the band gap E_g is the energy difference between the bottom of the conduction band and top of the valence band[**43**].

For a molecule an important consideration is of the frontier orbitals i.e. HOMO (Highest Occupied Molecular Level) and the LUMO (Lowest Unoccupied Molecular Level). The difference between the HOMO and LUMO level is called the HOMO-LUMO gap which is analogous to the concept of band gap for inorganic materials[**44**].

When a metal-molecule junction is formed an important property for the interaction between them is the alignment of the Fermi level of the metal and the HOMO/LUMO of the molecule[**45**]. When they align there can be a transfer of electron. In a molecular wire a simple charge transfer can be understood by electron hopping wherein an electron first hop from electrode to molecule and then hops again from molecule to electrode. So we need to also consider the how easily the electron can hop which depends on the how well the two are coupled called the strength of coupling between the metal and molecule. There are three possible cases weak coupling , intermediate coupling and strong coupling. To better understand this concept we introduce the coupling parameter(Γ) and the additional energy(U)[**46**].

Weak Coupling ($\Gamma \leq U$)

The wavefunctions of the HOMO and LUMO have negligible mixing with the electronic states of the electrodes.

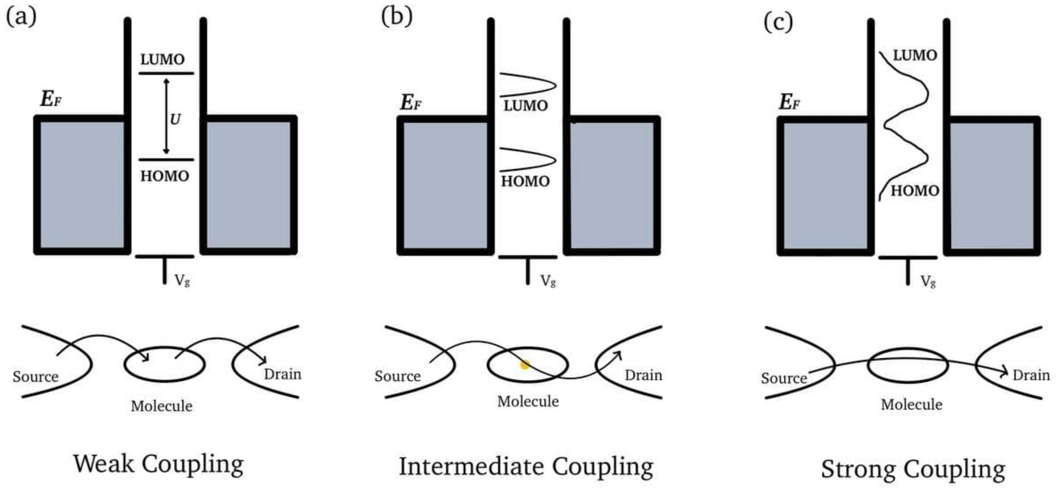

Figure 4.3: The schematic diagram of the charge transport mechanisms with different coupling strength of molecules and electrodes. (a) In the weak coupling, the electron transport follows a two-step process. (b) In the intermediate coupling, the electron transport through the molecules interacting with the electrons on the molecules. (c) In the strong coupling, the electron transport from the source to the drain by a one-step process.

Intermediate Coupling

In this case when an electron is transferred in the molecule it can interact with the electrons of the molecule as well. For instance it can change the spin of an electron in the molecule leading to new transport channels as well.

Strong Coupling($\Gamma \geq U$)

The wavefunctions of the HOMO and LUMO in this case have a significant overlap with the electronic states of electrodes. This leads to a very efficient transport of electrons. They move completely free across the interface in a single step coherent process[**47**].

Let us further understand the current flow through molecules. A dominant process in short molecular films is quantum mechanical tunneling. To explain tunneling the electron can be considered as a wave having a barrier to cross. The amplitude of the wave function approaches zero with distance. Depending on the interaction of the electron wave with the medium we can have elastic or inelastic transport. In eleastic transport(ballistic) there is no interaction of the electron wave with the medium thus no scattering. Whereas in inelastic transport the electron wave interacts with the phonons and excitons leading to some scattering. We can also have coherent (phase of the wave is conserved) or incoherent transport (phase of the wave is not conserved as the electrons spend time localized in intermediate state)[**47**]. Coherent tunnelling is modelled using Landauer formula:

$$G = \frac{I}{V} = \frac{2e^2}{\hbar} T_L T_R T_{Mol}$$

where, I is the current through the molecular junction, V is the applied bias, e is the elementary charge, $\hbar$ is the Plank's constant and T_L, T_R and T_{mol} are transmission coefficients of electrons through the left contact, the right contact and the molecule, respectively.

In the non-resonant case when the Fermi level does not align with molecular energy level i.e. it is between the HOMO and LUMO level the conductance depends on the both the offset in energy level and the coupling strength at the interface. While in the resonant case since there is alignment of levels only coupling strength at the interface plays a role in conductance. When we investigate the charge transport we need to consider both the coupling strength and energy level alignments.

Chapter 5

Graphene State-of-art

1 Introduction

Graphite has been used as a pencil lead for ages, and it is a well-known material. Graphene is a single layer of graphite that exists in two dimensions. Many theoretical works have been written about it in the past, but it has never received the level of attention that it has now. The first group to synthesise graphene (in two dimensions) was Novoselov et al. in back in 2004. Following the first isolation of graphene—a single sheet of carbon atoms organised in a honeycomb structure[1], a two-dimensional materials gold rush began. Large mobilities [**47**], the ability to transport high current densities [**48**], and superior thermal conductivity [**49**] make graphene a promising material for future device applications[**50**].

The use of graphene in organic electronics appears intriguing as well [**53**], given its excellent transparency [**51**] and outstanding flexibility [**52**]. The discovery of two-dimensional carbon as a potential transistor material comes at an ideal time, as silicon-based transistor downsizing is reaching its limits. As a result, numerous experiments have been—and continue to be—conducted to investigate the fascinating features of graphene and graphene-related compounds.

The lack of a band gap in graphene's pure form is its largest limitation in terms of electrical applications [**47**]. This gap is required to turn on and off a device's current flow. Cutting graphene into narrow strips, known as graphene nanoribbons (GNRs), is one technique to change its electrical structure. As a result of quantum confinement, the much-needed band gap emerges [**54**].

2 Theoretical Basis

Carbon is a very adaptable element that forms the basis of life due to its capacity to build a wide range of complexes with a wide range of binding partners in a variety of geometries. It can appear in a variety of dimensionalities in its purest form. Figure 5.1 depicts a few examples. Carbon atoms can join in three dimensions (3D) to create diamond or graphite, graphene in two dimensions (2D), carbon nanotubes (CNTs) and graphene nanoribbons (not represented here but described in detail later) in one dimension (1D), and fullerenes in zero dimensions (0D). The electronic configuration of carbon, which is $1s^2 2s^2 2p^2$ in its ground state [**55**], is linked to its adaptability.

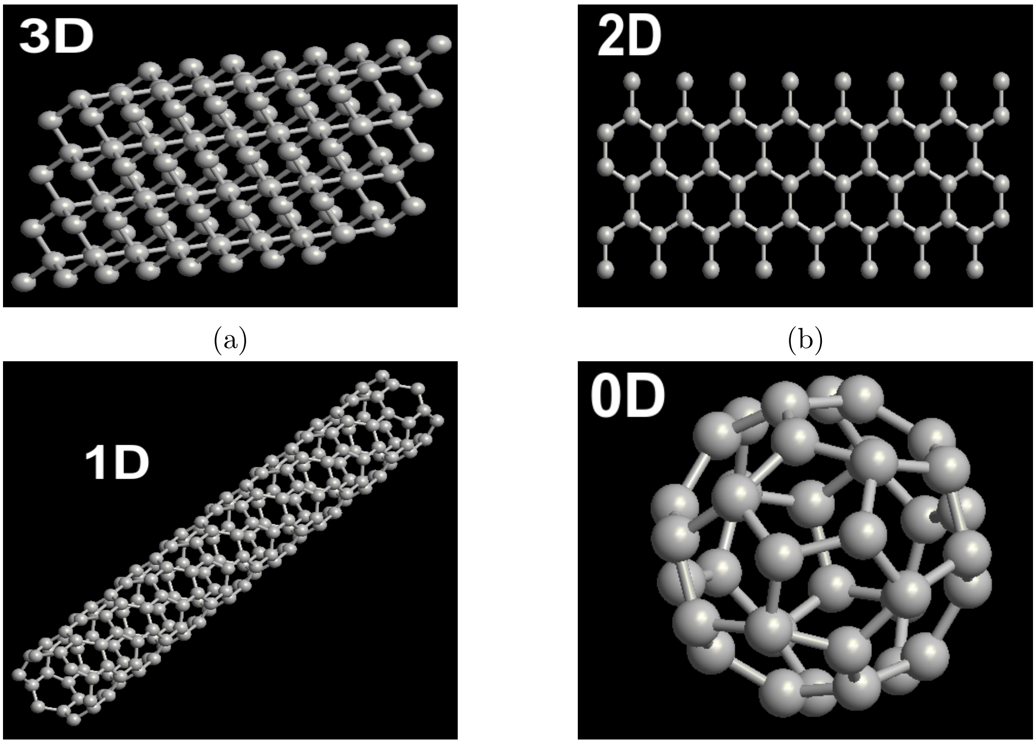

(a) (b)

(c) (d)

Figure 5.1: Allotropes of graphene: Various forms of carbon atom arrangement in different dimensions. From 3D (diamond) over 2D (graphene) and 1D (carbon nanotubes) to 0D (fullerenes) [Taken from QuantumATK].

Carbon, on the other hand, may make several types of covalent bonds (single, double, and triple) and generate varied structures by forming hybrid orbitals by mixing s and p orbitals [**56**]. It can have a variety of qualities depending on how it is arranged. For example, while diamond is electrically insulating, graphite is conducting. The carbon atoms of graphene, a 2D allotrope of carbon, are sp^2 hybridised and form a planar honeycomb lattice with bonding angles of 120 degrees. Three of the four valence electrons form strong σ bonds with the atoms next to them. The p_z orbital, which is perpendicular to the graphene plane, houses the remaining valence electron.

Bonds form as a result of lateral overlap with adjoining p_z orbitals. These are

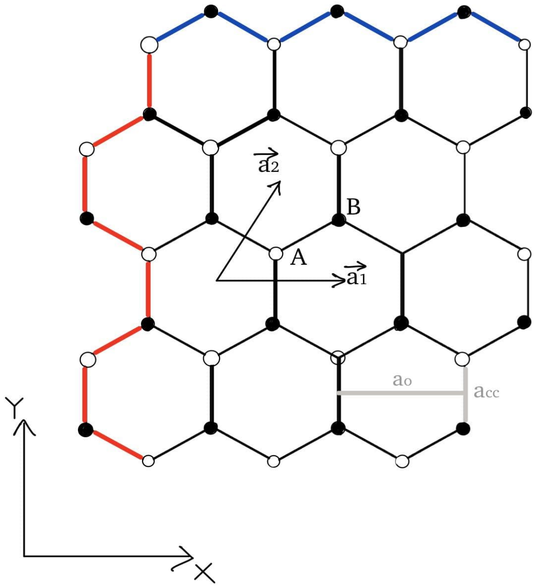

Figure 5.2: Honeycomb structure of graphene composed of sublattice atoms A (white circles) and B (black circles) with nearest neighbor distance a_{CC}. The lattice vectors $\overrightarrow{a_1}$ and $\overrightarrow{a_2}$ span the unit cell (with the lattice constant a_0. The armchair direction is emphasized by a red line, the zigzag direction by a blue one.

delocalized over the graphene plane and are responsible for graphene conductivity [**57**].

Figure 5.2 shows the hexagonal lattice of graphene, which is made up of two trigonal sublattices named A (white atoms) and B (black atoms) [**55**]. A unit cell includes one atom of each sublattice, and the lattice vectors $\overrightarrow{a_1} = (a_0, 0)$ and $\overrightarrow{a_1} = (\frac{1}{2}a_0, \frac{\sqrt{3}}{2}a_0)$ span it. The lattice constant is $a_0 = \sqrt{3}a_{cc} = 2.46\text{Å}$, while the distance between two nearby carbon atoms is $a_{cc} = 1.42\text{Å}$.

The hexagonal reciprocal lattice is also hexagonal. The reciprocal lattice vectors b_1 and b_2 and the high symmetry points Γ in the centre of the Brillouin zone(BZ), K and $K^{'}$ at the corners of the BZ, and M halfway between them are shown in Fig. 5.3. Because graphene has two unique trigonal sublattices, K and $K^{'}$ are not equal.

A tight-binding technique can be used to calculate graphene's band structure. Wallace had earlier done this for graphite in 1947 [**58**]. In its most basic version, only interactions between nearest neighbours are considered. The electrons in the tight-biding model are thought to be confined to carbon atoms (one electron per atom) and hop from one p_z orbital to the p_z orbital of an adjacent carbon atom. In the simplest model, nearest-neighbor hopping and electron coulomb interaction are ignored, but they can be implemented. The band structure's derivation is not shown here, but may be explored in detail in Refs.[**56**, **57**, **59**].

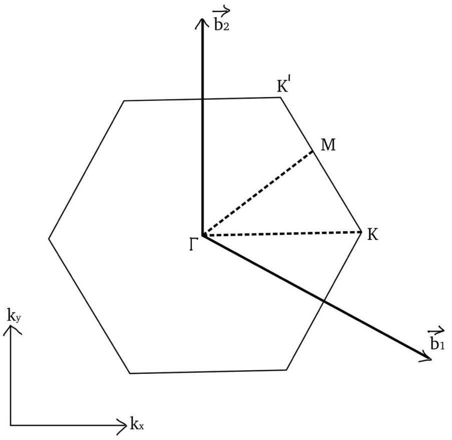

Figure 5.3: First Brillouin zone of graphene with the reciprocal basis vectors $\overrightarrow{b_1}$ and $\overrightarrow{b_2}$. The high symmetry points Γ, K, K' and M are marked.

In summary, the Schrödinger equation may be solved and the following dispersion relation obtained by representing the eigenfunctions of graphene as a linear combination of Bloch waves[**56**, **57**].

$$E(k) = \pm t\sqrt{1 + 4cos(\frac{\sqrt{3a_0k_x}}{2})cos(a_0k_y2) + cos^2(\frac{a_0k_y}{2})} \tag{5.1}$$

The wave vector is given by $\overrightarrow{k} = (k_x, k_y)$, and the nearest-neighbor hopping energy is given by $t \approx$ 3eV. (also referred to as transfer integral or hopping parameter). The bonding π band (represented by the " − " sign in Eq. 5.1 and corresponding to the valence band (VB)) and antibonding $\pi^\star$ band (defined by the " + " sign, corresponding to the conduction band (CB)) are depicted in figure 5.4 along the dashed line shown in figure 5.3 .

In the 3D form of the energy dispersion (not shown here) the bands have a conical shape near the K and K' points and exhibit linear dispersion. The electrons can be characterised as quasi-relativistic (massless) particles in the absence of band curvature. As a result, the K and K' points are also referred to as Dirac points. Close to the Dirac points, the energy dispersion can be approximated by

$$E(\overrightarrow{k}) = \pm\hbar\nu_F|\overrightarrow{k}| \tag{5.2}$$

with the reduced Planck constant and the energy-independent Fermi velocity $\nu_F = 3ta_{cc}/(2\hbar) \approx 10^6 m/s$

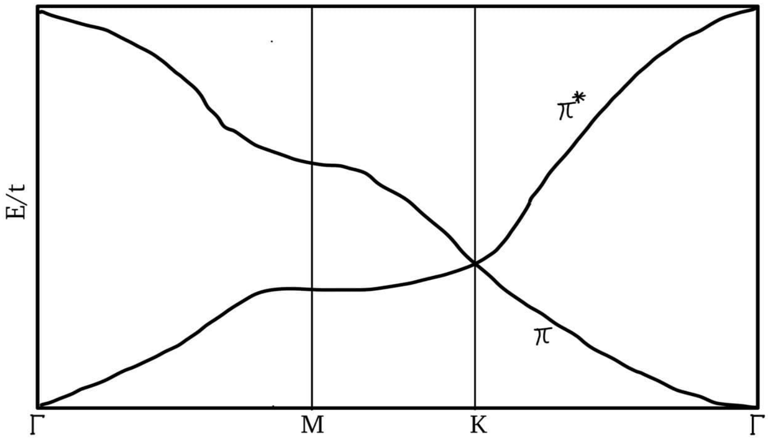

Figure 5.4: Band structure along the dashed line in (b). The energy is given in units of t.

3 GNR

As seen in the previous section, there is no band gap in virgin graphene, which is required for use as a transistor material. Cutting graphene into narrow strips, known as graphene nanoribbons, can be used to create a gap. Then quantum confinement can cause a band gap to open [**54**].

Graphene edges come in two fundamental forms [**60**]. When cutting a graphene sheet along the blue line in Fig. 2.2, one problem develops (a). The resulting edge is known as a zigzag edge, and the matching GNRs are known as zigzag GNRs, due to the zigzag arrangement of the carbon atoms along this line (zGNRs). Cutting graphene along the red line, for example, produces armchair edges and armchair GNRs (aGNRs).

Other varieties of GNR edges exist, but they can be thought of as (often periodic) combinations of armchair and zigzag cusps running along the edge. Because the transversal wave vector depends not only on the zGNR width but also on the longitudinal wave vector, the situation for zGNRs is slightly more complicated than for aGNRs. Details are not explored in this paper, but can be found in references [**57**, **61**].

To summarise, tight-binding calculations for zGNRs result in partially flat bands, which lead to magnetic order along the zigzag edges. It's worth noting that the sign of the magnetic moments is the same for all atoms on one sublattice and the polar opposite for atoms on the other. As a result, all magnetic moments along a single zigzag edge point the same way.

Magnetic moments are strongest at the zigzag edges but weaken as one approaches the zGNR centre. zGNRs are invariably metallic, according to tight-binding calculations. The addition of Coulomb interaction in the framework of Hubbard model, on the other hand, results in the opening of a band gap in zGNRs. Using a Hubbard model still yields flat bands and therefore magnetic moments at the zGNR edges.

4 Fabrication of Graphene

It is possible to distinguish between two major ways in order to properly prepare graphene. Graphite is a layered substance, with each layer made up of a single graphene sheet. Separating the graphite into its constituent layers is one of the procedures that may be used to make this material. Top-down techniques are approaches that begin with a three-dimensional structure and lead to the complete, or nearly complete, disassembly of the crystal into its constituent layers; this category includes mechanical exfoliation techniques such as rubbing and scotch tape exfoliation, as well as chemical exfoliation techniques. On the other hand, bottom-up techniques, which are devoted to the creation of monolayer graphene utilising a material other than graphite as a growth substrate, are positioned on the opposite side. Thermal dissociation of SiC and Chemical Vapor Deposition are two of these methods (CVD)

Top Down Approaches

Micromechanical exfoliation

The true genesis of the notion of graphene exfoliation may be traced back to the development of the pencil as a writing instrument, in chronological sequence. The trace of a pencil might be considered the earliest example of graphite exfoliation [**63**]. A Highly-Oriented Pyrolitic Graphite (HOPG) block, accessible in many typologies in commerce, serves as the starting point for micromechanical exfoliation. Typically, the HOPG surface layer is removed from the block with a mild push and subsequent removal of a conventional adhesive tape. This operation is carried out to avoid any changes in the exfoliation, since the surface may get oxidised accidentally[**47**]. The tape is then used to peel off a layer of HOPG from the block, as implemented by Geim's group [**47**]. A mono-layer thin sample can be made by continually peeling off layers from the initial cleft flake.

After that, the graphitic pieces may be transferred to any substrate by simply pressing the tape against it. Unfortunately, the existence of adhesive residues dispersed inside the flakes is an inherent downside of this approach. As a result, several additional options for mechanically exfoliating HOPG include using polymeric films instead of tapes. Because of their simple interaction with graphene, such polymers provide a cleaner transfer of the material onto any substrate, avoiding adhesive residues and the need for further cleaning. Although micromechanical exfoliation gives generated graphene a high quality, it has considerable drawbacks in terms of large-scale production. Nonetheless, because graphene flakes adhere to the substrate entirely by Van der Waals interactions, it is still the preferred approach for studying its characteristics.

Liquid phase exfoliation (LPE)

Intercalating agents, which are molecules that position themselves between layers, and surfactants are used in liquid-phase exfoliation (LPE) to distribute graphite flakes into a solution. Mechanical processing stages, such as controlled ball milling, as well as solvothermal and sonochemical processes, help to support it. This approach produces a scalable version of graphene with several layers at a cheap cost, resulting in micron-scale platelets known as graphene nanoplatelets (GNPs). After each of these procedures has been accomplished, the graphene is ready to use in an organic solvent, semidispersed. The graphene must be further processed to get nanosheets.[**81**]

Sonication At relatively high concentrations, sonication is one of the stages utilised in LPE techniques, and it creates monolayer or few-layer graphene. The activation of cavitation bubbles is the primary process by which sonication causes physical or chemical changes. As ultrasonic waves propagate through the medium, cavitation bubbles form, creating both high-pressure and low-pressure zones that push and pull on the molecules.

High-shear mixing

As an exfoliation process, LPE employs high-shear mixing. High-shear mixing and sonication are similar in that aqueous liquids may be used to exfoliate graphite and generate stable graphene dispersions, eliminating the requirement for hazardous organic liquids. The main difference between high-shear mixing and sonification is that high-shear mixing is far more efficient as a method.

Microfluidization

Microfluidization is a method of homogenization that uses high pressure. It applies high pressure to the fluid, forcing it through a microchannel. Microfluidization's key advantage is that the moderate exfoliation it induces can reduce the amount of flaws in graphene.

Microfluidization methods have recently been used to create quantum dots and graphene-based conductive inks. When compared to sonication and high-shear mixing, microfluidization is preferable since the high shear rate is present throughout the fluid area. Cavitation, shear stress, and collision produce exfoliation in microfluidization, and the dispersion of graphite is driven into the chamber channel, resulting in shear force-controlled exfoliation.

Micro jets induce collisions and shear stresses, allowing monolayer or few-layer graphene to self-peel down due to its lateral self-lubrication capability. Cavitation has a similar function to sonication-assisted LPEs.

Bottom-up approaches

Growth on silicon carbide

The main component of this approach is a vacuum thermal treatment of a Si-terminated SiC {0001} substrate [**64**]. Two key processes are confirmed under particular conditions: the sublimation of silicon atoms near the surface and the rearranging of carbon atoms in graphene's honeycomb-structure lattice. The key advantages of this approach are the ease with which SiC substrates may be obtained and, more importantly, the lack of the difficulty of transferring the material onto a substrate, which, as shown in the previous method, is a critical obstacle in the material's research.

The difference in vapour pressure between carbon and silicon is a critical component of graphene epitaxial development on the so-prepared Si terminated SiC surface. SiC moves through distinct crystallographic phases, which correspond to transient rearrangements of the atoms at the surface, when the temperature rises under correct pressure circumstances. Sublimation of silicon and graphitization of carbon atoms occur as a thermodynamically beneficial process when temperature and pressure levels above the threshold of vaporisation of silicon. Despite this, SiC may have a variety of crystal shapes known as polytypes [**65**]. A correct polytype should be employed in order to accomplish successful graphene synthesis.

Chemical Vapor Deposition(CVD)

The heating of a metal substrate immersed in a carbonaceous gas combination, mostly methane and ethylene hydrocarbons, is another method for producing single- and few-layer graphene. Chemical Vapor Deposition is the name for this method. The breakdown of precursor molecules to generate active carbon species and their absorption into the substrate to form a solid solution are the processes involved in this approach. Transition metal substrates are employed for this because they have a much larger atomic radius than carbon, allowing for its solubilization. As a result, the metal substrate serves as both a catalyst for the dissociation of carbonaceous molecules and a solvent in which carbon is dissolved first. Carbon atoms tend to nucleate on the metal surface at a later stage, when the system is progressively cooled, until a hexagonal-lattice crystalline layer is formed. This is due to the decrease in carbon's solubility in the metal.[**66**, **67**]

An alternate CVD synthesis approach involves creating a plasma phase in the gaseous mixture to improve the same process at a lower temperature. Plasma-Enhanced CVD is the term given to this method. In comparison to traditional CVD, the standard experimental setup includes the use of an electrode. Ionization of the gaseous mixture by electrical discharge up to the plasma phase is required for effective graphene production. The production of active atomic carbon is aided by the stimulation of inactive species in the mixture. As a result, the energy necessary to dissolve carbon into the underlying metal sheet is delivered by the plasma rather than by a thermal process. Because electrons have a smaller mass than ions and require less energy to sustain an excited state, this approach requires a lower temperature [**68**]. The plasma, on the other hand, has the potential to harm the developing substance.

5 Fabrication of GNRs

There are several ways to obtain GNRs and depending on the synthesis technique, the structure and physical characteristics of GNRs differ greatly. GNRs can be fabricated by etching lithographically structured graphene sheets, unzipping carbon nanotubes, etc. These methods are called top-down approaches because they start with a larger entity which is then reduced to a GNR.

Top Down Methods

Lithography

On a substrate surface, this method produces single-layer GNRs. This technique has a substantial number of papers. The usage of lithographically manufactured GNRs is restricted to situations in which the GNRs are laid flat on a surface. Lithographic processes cannot be used to generate large volumes. Furthermore, lithographically manufactured GNRs have rough edges due to intrinsic limitations in the lateral resolution of lithography-based technologies [**69**, **70**]. While this approach creates extremely accurate and thin GNRs, the uncontrolled jagged edges that arise make controlling the electrical characteristics of the materials problematic.

Unzipping CNTs

The longitudinal opening, or unzipping, of multi-walled carbon nanotubes is the third method for fabricating GNRs (MWCNTs)[**71**, **72**]. Although the methodologies presented differ, they are virtually all solution-based approaches. The ability to mass produce on a kilogramme scale is a key benefit of this strategy over the prior two. Another benefit is the significantly cheaper cost. Furthermore, based on the number of recent publications, these CNT-derived GNRs are expected to be the first to discover real-world applications.

The disadvantage of top-down method is the lack of atomic precision with which the GNR edges are obtained. This negatively influences the transport properties of the GNRs [**73**].

Bottom-Up Approach

An alternative path was opened by advances in on-surface chemistry. During the so-called bottom-up approach, GNRs are formed by fusing small building blocks on a catalytic metal surface [**74**, **75**]. These surface synthesized GNRs can be fabricated with atomic precision. Their fabrication process relies on a surface assisted bottomup assembly of precursor molecules in UHV [**74**]. By choosing the right precursor molecule, almost all GNR geometries can be realized. This method allows for the creation of very narrow ribbons with atomically precise edge configuration. Until recently, this type of GNRs could only be prepared on the surface of a substrate, limiting the potential for bulk production. Despite the fact that such ribbons have been recently synthesized in a scale of hundreds of milligrams, it is difficult to see their actual applications in the near future. While the great accuracy and narrow size distribution of GNRs produced via bottom-up synthesis may have future applications, there are presently no ready-to-use methodologies for further processing these small structures. This technology hasn't been thoroughly utilised yet, and it's tough to see it being used in the near future.

An advantage of on-surface synthesized GNRs is that no solvents have to be involved in the ribbon growth. Since the process takes place in UHV, the surface stays extremely clean. Additionally, there is an enormous number of precursor molecules, allowing a huge variety of possible GNR shapes. On the other hand, performing the synthesis in UHV demands sophisticated equipment. Additionally, the GNRs are typically grown on metallic substrates which prevents their direct electronic characterization, since the GNR states hybridize with the states of the metal substrate. This requires a transfer of the GNRs to an insulating substrate which usually involves etchants leaving residues that contaminate the GNRs [**76**]. There are possibilities to grow GNRs on the semiconducting surfaces of TiO2 [**77**] and Ge(001) [**78**], but those GNRs cannot compete with the ones synthesized on metals in terms of edge quality. To circumvent these problems, one can use solution-processable GNRs [**79**]. They offer a large variety of different shapes as well. Additionally, they are typically longer than their on-surface synthesized counterparts and easy to process. Typically, the synthesized GNR powder is dispersed in a solvent and drop-cast onto an arbitrary surface.

6 Nanogap Creation

One of the main challenges in fabricating nanogapped carbon electrodes is precise control of the gap size. One of the methods to do this is performing electroburning. The feedback-controlled electroburning takes place in room-temperature air. The feedback control approach is based on electromigration of metallic nanowires using comparable methods. The graphite flake is typically subjected to a voltage (V) ramp (1 V/s), while the current (I) is constantly recorded at a particulaar sample rate. With a feedback setup the fluctuations in conductance (G= I/V) are monitored. When such a drop occurs, the voltage is swept back to zero. Following that, a fresh sweep is started from zero voltage and the procedure is repeated, gradually narrowing the flake. In the Ref. paper [**80**] nanogaps of a few nanometers were aheived using this technique.

Another technique is using Atomic Force Microscopy(AFM) to tailor the nanogaps on graphene. The AFM tip is used to cut small gaps on the sheet of graphene. But, AFM tip is not directly used on the sheet rather the etching is done by placing the sheet on SiO2/Si subtrates or any other substrate which gets removed easily.[**82**]

Chapter 6

Metal-based Electrodes Analysis

1 Introduction to QuantumATK

QuantumATK (Atomistix Tool Kit)[**83**] is an integrated set of atomic-scale modelling tools created in partnership with academic researchers by professional software engineers. The QuantumATK platform's simulation engines enable electronic-structure calculations using density functional theory. It comes with a comprehensive collection of tools for performing atomistic simulations. The advantage of QuantumATK is its Virtual Nano Lab Graphical User Interface (GUI) (VNL). It's easy to use and understand.

VNL can be used as a graphical user interface (GUI) for other programmes because it can import and export a variety of file types. Within the context of DFT, QuantumATK can model the electronic characteristics of closed and open quantum systems. Linear Combination of Atomic Orbitals (LCAO) basis sets are used numerically. The density matrix, which defines electron density, is a critical parameter in the self-consistent calculation of the Kohn-Sham equations. For open systems, the tool calculates the density matrix using non-equilibrium Green's functions (NEGFs), whereas for closed systems, the density matrix is computed using diagonalization of the Kohn-Sham Hamiltonian.

The Hartree, external, and exchange-correlation potentials are used to determine an effective potential based on the computed electron density. The QuantumATK platform includes simulation engines that support the full range of atomic-scale simulation methodologies used in the semiconductor industry and in material research in general. This platform offers a comprehensive set of exchange-correlation capabilities. The tool primarily supports LDA, GGA, MGGA, and Hybrid functionalities. ATK also includes a library of pseudopotentials for all elements in the periodic table and uses norm-conserving pseudopotentials to avoid explicit DFT computations of core electrons. SG15 and PseudoDojo are the default pseudopotentials in QuantumATK.

The first part of the thesis was focused on learning how to setup DFT calculations in QuantumATK. For this an exercise was done focused on the possible application of the molecular transistor as a gas sensor. The basic principle is that the presence of a target chemical species (in this case chromium) is able to significantly influence the transport and change the current flowing in the structure. The designed molecular wire was based on cyclophane molecule[**84**]. The results of the exercise are summarized in the Appendix A. Through this exercise I acquired a good working knowledge of QuantumATK.

After this the work was shifted to reproducing the results reported in [**85**]. In this paper pyridine was used as a central molecule for the molecular wire. Keeping the central molecule same five different electrodes were used viz. gold, silver, copper, zigzag graphene nanoribbon(ZGNR) and graphene nanosheets(GNS). Similar results were obtained for all expect the GNS case. First principle calculations are based on self consistent loops were to acheive the result a convergence is to be reached. A major problem with GNS was reaching this convergence at high biases. This was eventually solved at a later stage and the setting used are mentioned in the results chapter of graphene electrodes. The simulation results obtained are reported in Appendix B.

Now, I will discuss the different structures that were analyzed. Starting with metal electrodes viz. gold(Au) electrode and then to silver(Ag) and copper(Cu) all having Face-Centered-Cube (FCC) with the Miller Indices of (111). For the central region two molecules were used namely oligo phenylene ethynylene(OPE) with the functional unit repeated three times thus referred as OPE3 and the second molecule being a derivative of oligo thiophenes (OT) with the functional unit repeated twice and will be referred as 2TT. Using QuantumATK DFT simulations was performed to obatin three main quantities the transmission spectrum T(E), the density of states(DOS) and the IV Curve. The table 6.1 shows the settings that were used.

2 OPE3

The device geometry for the molecular wire based on gold electrode is shown in figure 6.1. The geometry for copper and silver case is also similar as seen in the following figures 6.2 and 6.3.

Table 6.1: ATK DFT-LCAO equilibrium calculator settings.

LCAO Calculator	
LCAO Basis Set	Exchange Correlation: GGA-PBE Basis Set: DZP
Numerical Accuracy	k point: 5 × 5 × 50 Density Mesh Cutoff: 75K
Iteration Control	Tolerance: 1e-5 Maximum Steps: 300
Device Algorithm	Default
Contour integral parameter	Default
Poisson Solver	Type: [Parallel] Conjugate Gradient Front,Back,Top,Bottom: Periodic Left, Right: Dirichlet

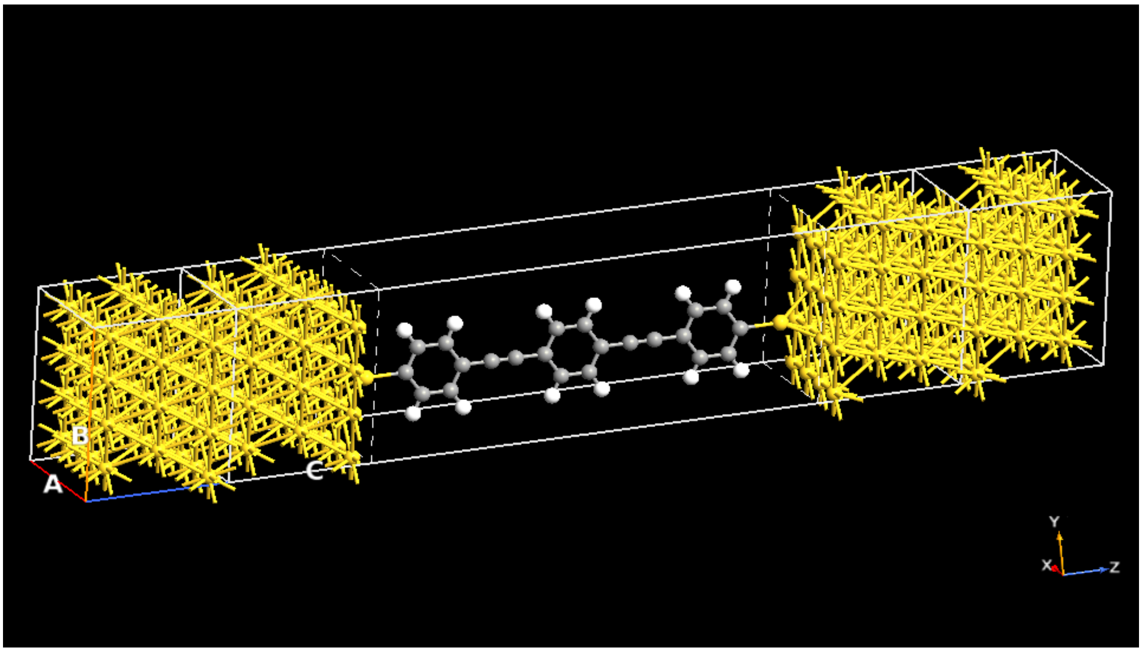

Figure 6.1: Configuration for Gold Electrodes taken from QuantumATK

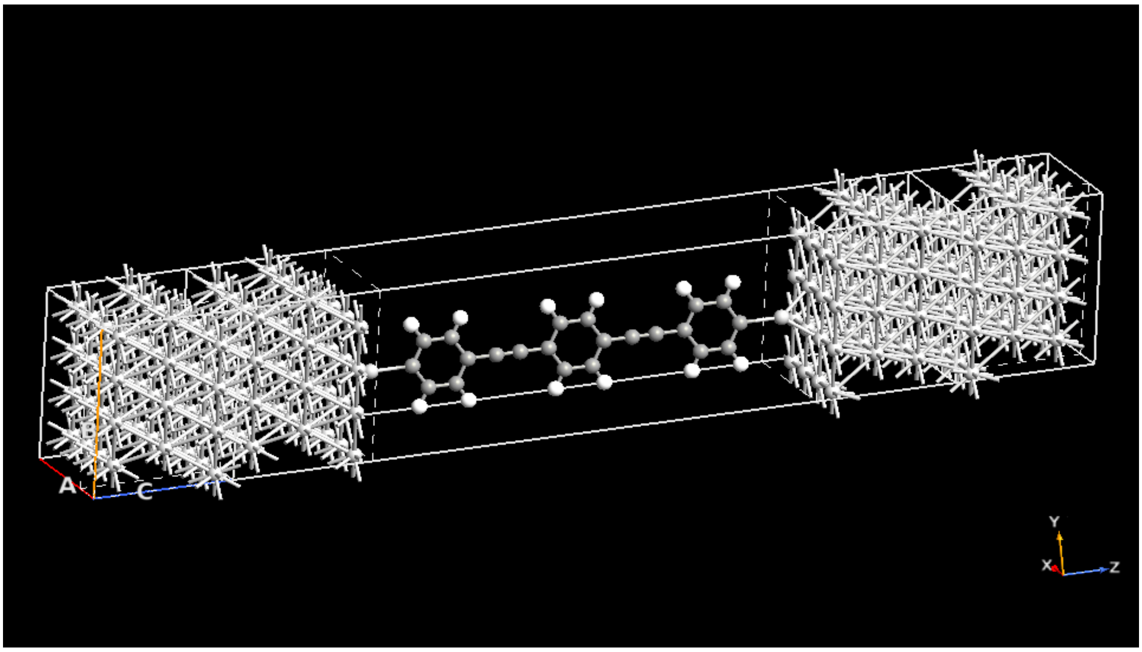

Figure 6.2: Configuration for Silver Electrodes taken from QuantumATK

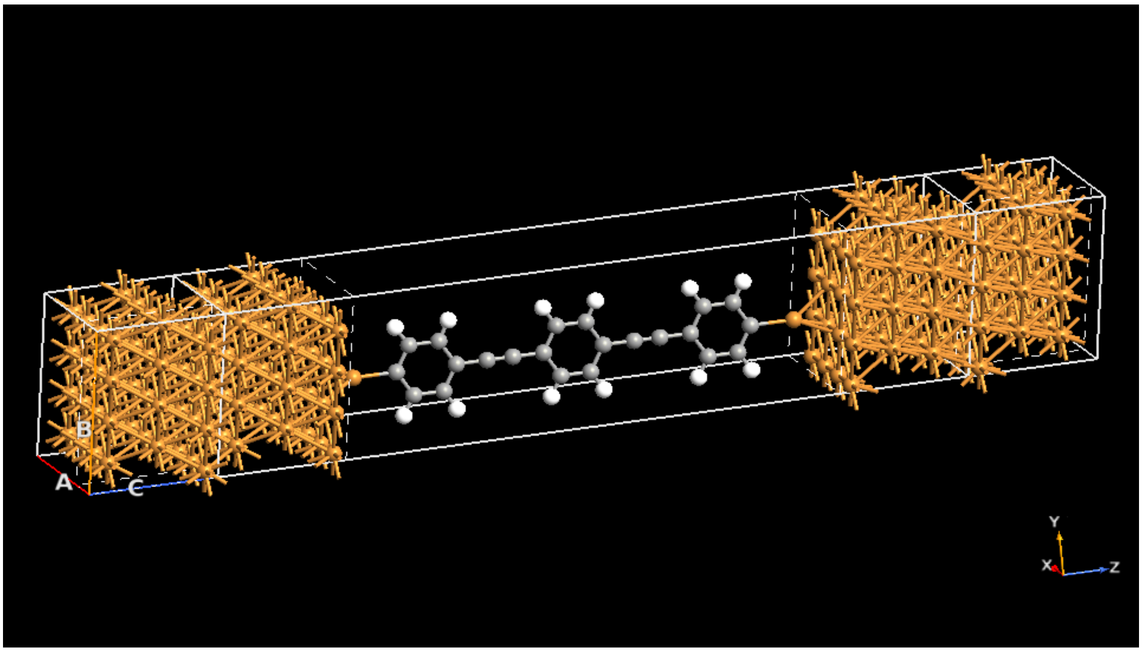

Figure 6.3: Configuration for Copper Electrodes taken from QuantumATK

Firstly the transmission spectrum T(E) is reported and the plots obtained for this case are shown below:

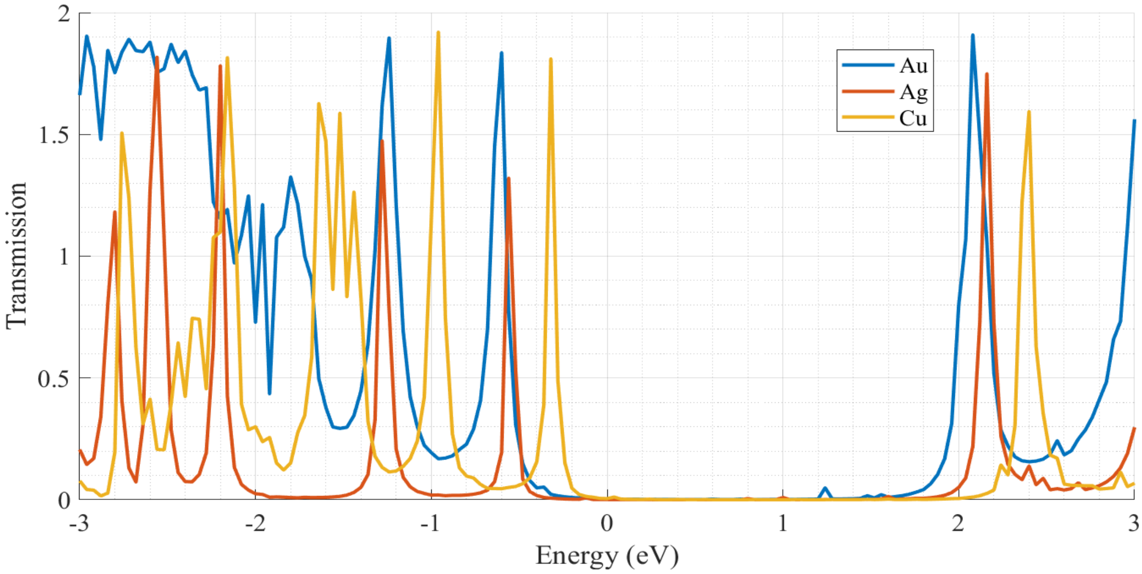

Figure 6.4: Transmission Spectrum for Metal Based Electrodes

Since from Landauer formula the current is proportional to the integral of the transmission spectra (weightened by Fermi-Dirac functions), the analysis of the transmission spectra is of crucial importance to understand the reason of an obtained I(V) curve. In figure 6.4 the transmission spectra for the OPE3-wire are reported for gold, silver and copper. Discrete and less broadened peaks are present close to Fermi energy (0 eV), while for lower energies broadened peaks are present. At lower energies there is also a greater number of transmission peaks and the discrete nature of the system is less evident. From these consideration it is possible to suppose that the independent peaks close to 0 eV are probably due to the discrete OPE3 energy levels (broadened because of the presence of the contacts); while for lower energies the (few) molecular states are dominated by the electrode DOS. In order to confirm these hypotheses an additional analysis of the DOS should performed. Before doing that, a comment of the obtained I(V) is reported.

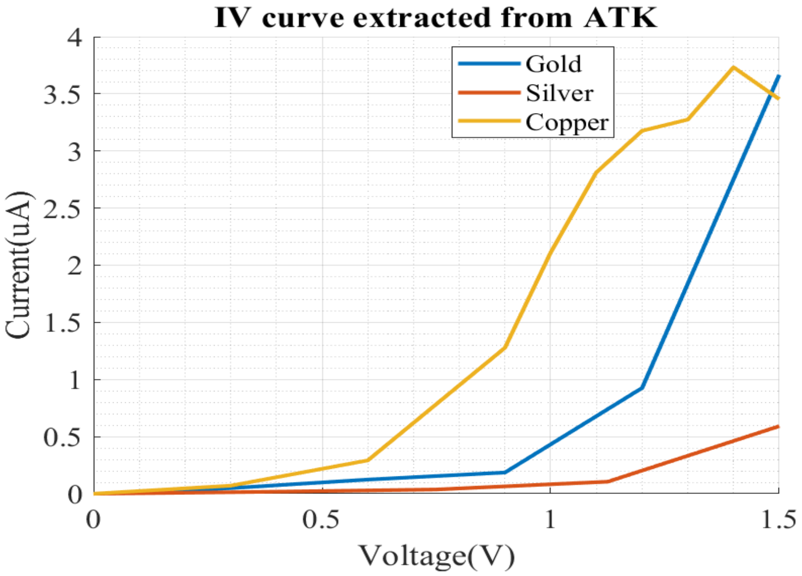

Figure 6.5: IV curve for Metal Based Electrodes

Since from Landauer formula the current corresponds to the integral in energy domain of the transmission peaks, the obtained I(V) curves are expected from the transmission spectra of figure 6.4. Even if with gold the transmission peaks are more broadened than with copper and silver, a greater current is obtained with copper. Indeed, the first peaks that conduct (below Fermi level), are farther from 0 eV in the case of gold and silver, while they are closest to Fermi level for copper. This makes the current increasing more sharply with copper than with the other two metals (yellow peak). Nevertheless, at voltages above 1.25 V, the first copper peak is completely included in the bias window and a saturation of current occurs. Instead, the corresponding peak with gold electrodes is entering in the bias window, thus producing a relevant increase of current. Even if also the peak with silver enters in the bias window, it is less broadened and presents less transmission probability, leading to a corresponding current smaller in magnitude w.r.t. gold.

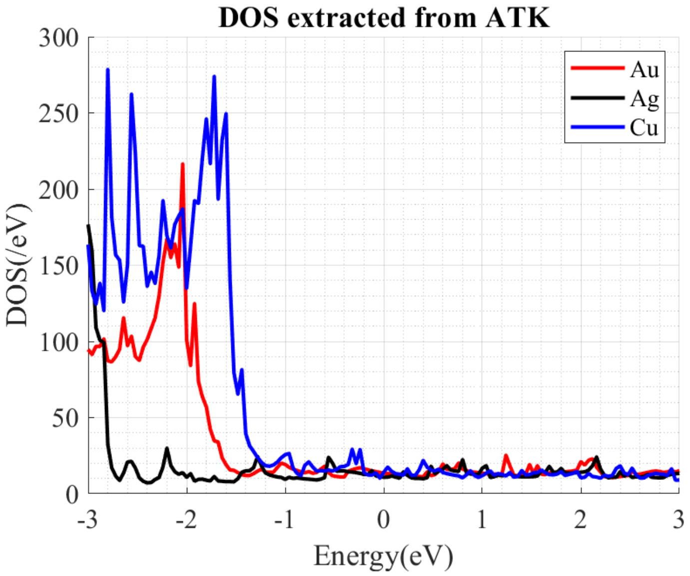

Figure 6.6: Device Denssity of States(DDOS) for Metal Based Electrodes

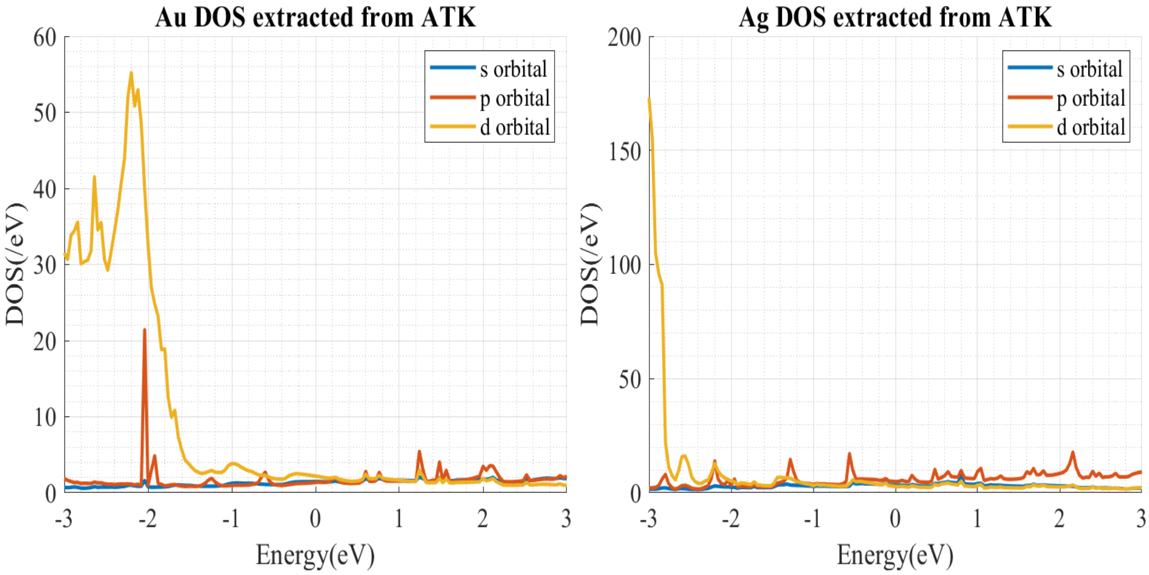

(a)

(b)

Figure 6.7: Orbital Contribution for Gold(a) and Silver(b) Electrodes

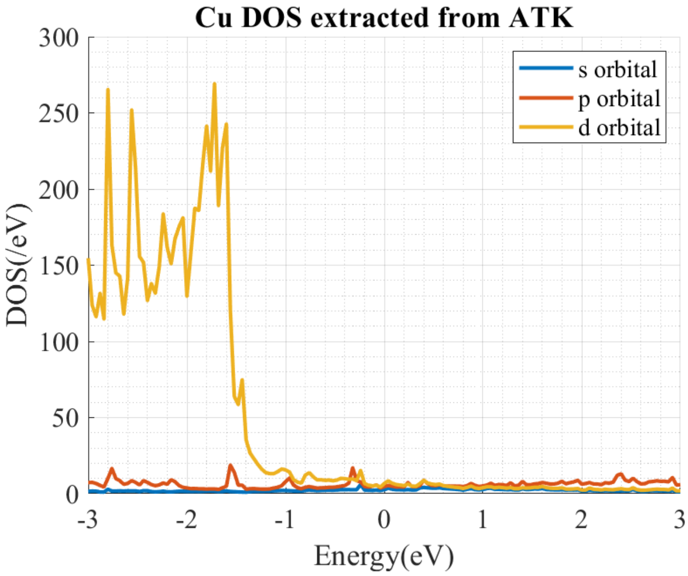

Figure 6.8: Orbital Contribution for Copper Electrodes

Coming back to the transmission spectra and the DOS, by comparing the transmission spectra of figure 6.4 with the contact DOS (figure 6.6) it is possible to confirm the above mentioned hypothesis: The transmission spectra peaks close to Fermi level (0 eV) are not present in the electrode DOS. This means that such peaks are related to molecular (OPE3) energy levels. Indeed they appear more spaced in energy, and less merged (i.e. more localized states) w.r.t. other transmission spectra peaks. Moreover, such peaks are less broadened w.r.t other transmission peaks at other energies. This makes sense if one thinks to the lesser influence of the electrodes on central states of the channel (that are farther from contacts w.r.t anchoring groups, thus having less wavefunction hybridization with electrode ones). Instead, concerning the peaks well below the Fermi level (at energies lower than -1 eV), by comparing them with the DOS of the electrodes (figure 6.6), there is good match of such transmission peaks and the contact DOS. This is likely related to a contact dominated transport mechanism: The transport is no more dominated by OPE3 states but by contact states. To further confirm this one can consider figures 6.7 and 6.8 where the contacts DOS are split in their orbital contributions. The dominant states of the contacts are d-type. The total contact DOS (figure 6.6) well resembles the d-type only DOS (figures 6.7, 6.8). This means that the dominant contribution in the contact DOS is from d-type orbital, and this reflects in the transmission spectra shape below -1 eV. Indeed, the transmission spectra resemble the contact DOS, and since it is mainly due to d-type states, such transmission states cannot come from the OPE3 orbitals (that is an organic molecule with p-type valence orbitals). Furthermore, the fact the transmission peaks below -1 eV are due to contact contribution is also evident from the peculiar shape of that states, that resembles an energy band (as expected in crystalline metal conductors).

In conclusion, the main effect of the contact is to dominate the transmission states at low energies, while the peculiarity of the molecular channel (in this case OPE3) is dominant close to Fermi levels (0 eV) and above it. This in turn means that for low applied biases (i.e. with a small bias window centered around 0 eV) the current is mainly dominated by molecular channel states. Instead at high bias the effect of the contacts become more important or even dominant: Indeed, the transmission spectra integrals of the low energy peaks (i.e. their area) is evidently larger than the discrete peak one.

For the sake of clarity, the transmission spectra are also reported in appendix.

Next, the orbitals were visualized for HOMO level at equilibrium which are reported here:

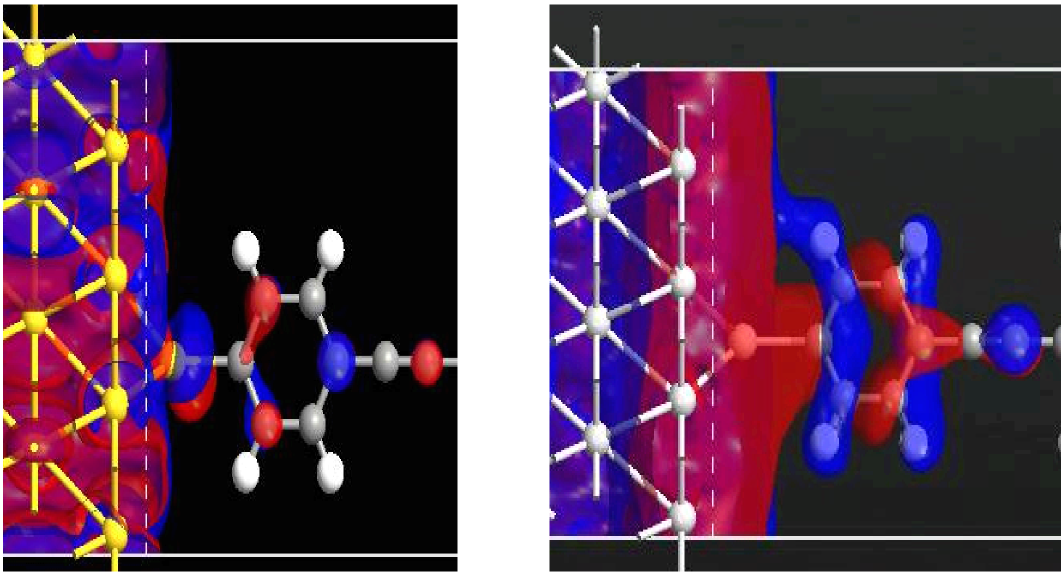

(a) (b)

Figure 6.9: HOMO Level for Gold(a) and Silver(b) Electrodes

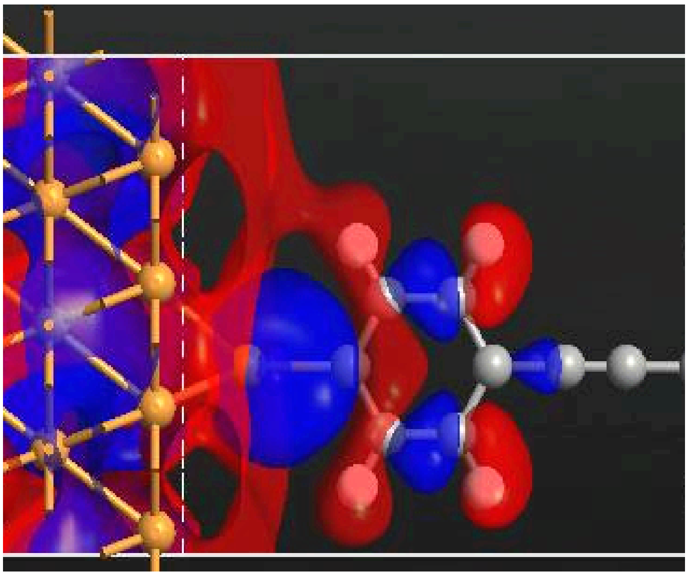

Figure 6.10: HOMO Level for Copper Electrodes

The system HOMO levels are reported in figures 6.9 and 6.10. It is evident that d-type orbitals within the contacts are not well merged, i.e. conjugated, with the OPE3 p-type ones. Indeed, there are barriers (i.e. absence of iso-surfaces) at the contact-molecule interface. According to the basic chemistry principle of maximum overlap of orbitals, there is not enough overlap between d-type contact orbitals and p-type OPE3 ones, resulting thus in a break of the conjugation. This probably means that metal electrodes are not the best one if the final purpose is to have perfect or maximum conjugation of orbitals, in terms of wavefunction delocalization. This could reduce the maximum saturation current that can be obtained with metal electrodes through coherent tunneling.

Additional orbital plots are reported in the appendix. Similar comments hold for them.

Next, I proceeded with analyzing the major transmission peak that was in the bias window. I will focus on the first transmission peak which are Au -0.64eV for Au, -0.56eV for Ag, and -0.32eV for Cu. The transmission eigenstate at these peaks is projected onto the Molecular Projected Self-Consistent Hamiltonian (MPSH) states of the molecule.

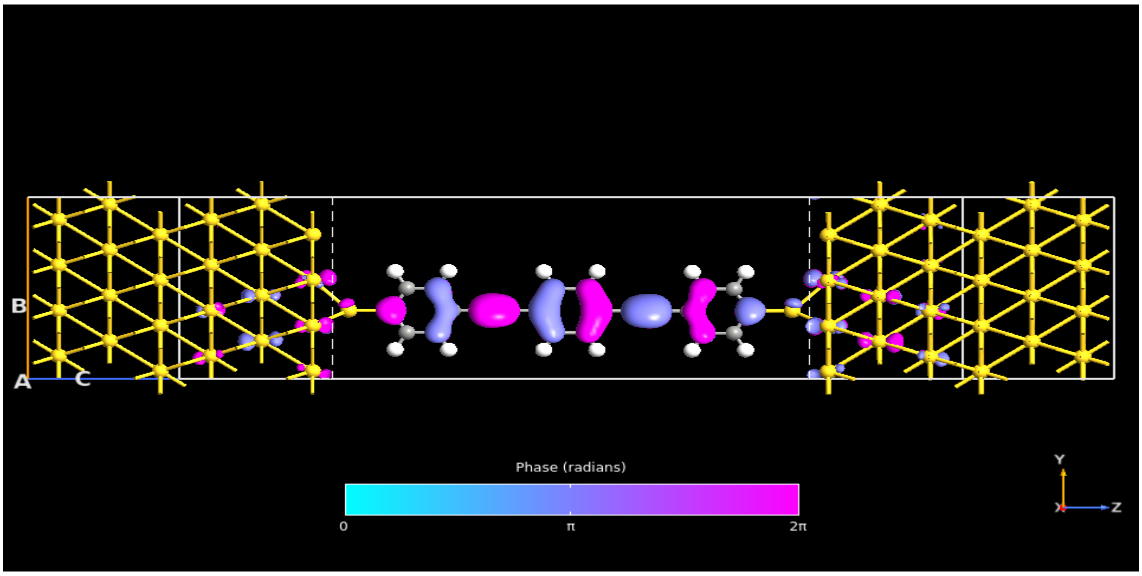

Figure 6.11: MPSH for Gold Electrodes

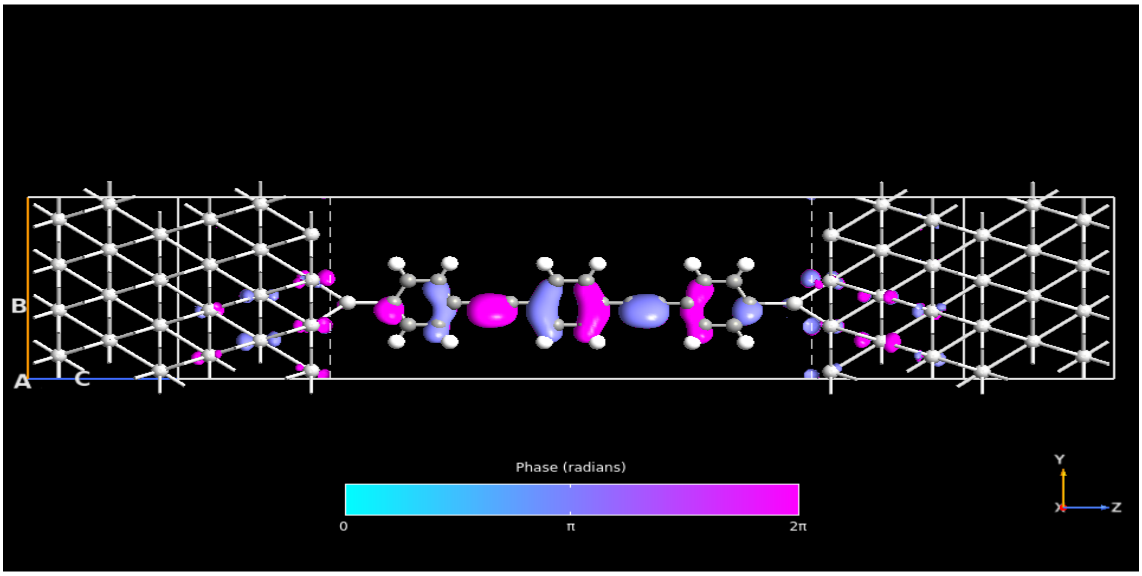

Figure 6.12: MPSH for Silver Electrodes

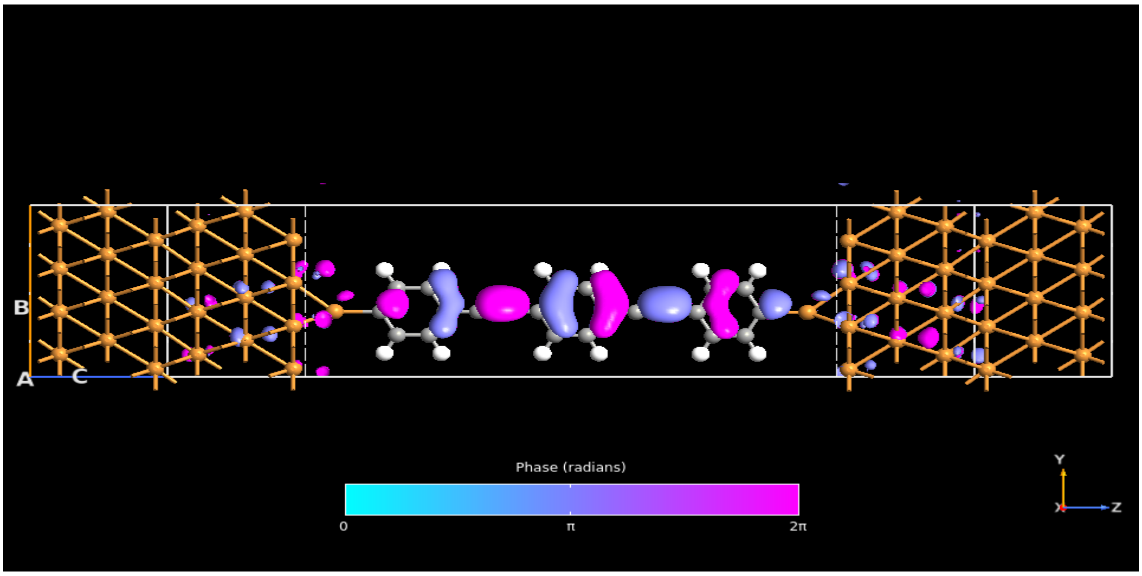

Figure 6.13: MPSH for Copper Electrodes

In figures 6.11, 6.12, 6.13 the main transmission eigenstates of the system HOMO contributing to the transmission peaks in the transmission spectra are reported. Their inspection reveals that transmission occurs through molecular states, and the main transport mechanism is coherent tunneling through molecule OPE3 orbitals. Indeed, the OPE3 is enveloped by the transmission eigenstate lobes, meaning that it contributes to transmission. Furthermore, the lobes are wider in the OPE3 than in the contacts (where a negligible transmission iso-surface is present), meaning higher transmission probability. If transport were contact-to-contact non-resonant tunneling the OPE3 molecule would not be enveloped by the transmission eigenstate surface, thing that does not happen here, proving the resonant tunneling transmission feature. Same considerations hold for all the three contacts. These analyses further confirm that the transmission peaks closest to Fermi level in the transmission spectra reported previously are related to molecular channel states.

For a better visualization of the available states PDOS was also calculated which gives a representation of the available states resolved in space and energy. The x-axis shows the co-ordinates of molecular wire with the value 0 assigned to begininging of the left contact. The y-axis is the energy range of -3eV to 3eV. And on this graph DOS is plotted using a color scheme thus giving us colorful visual on the available states at each point on the molecular wire. Dark colors indicate no states and very bright pink color indicates maximum states for a particular graph. The scale for each plot is different.

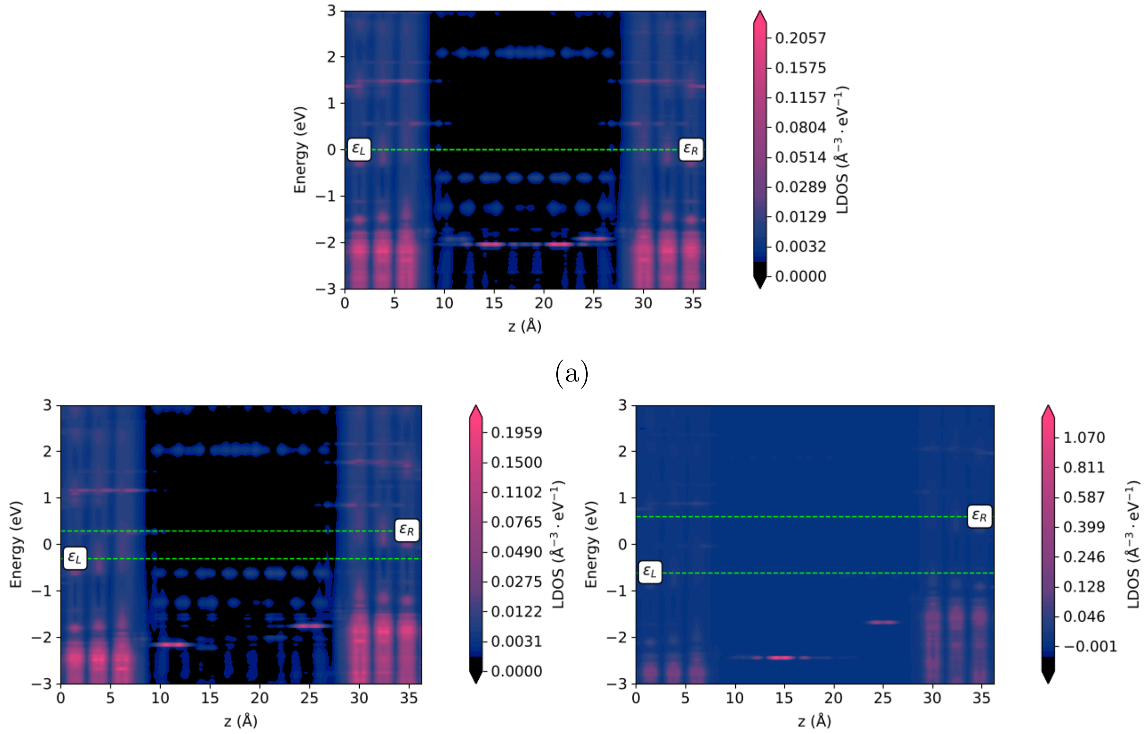

(a)

(b)

(c)

Figure 6.14: PDOS for Gold Electrodes for a bias of 0V (a), 0.6V (b) and 1.2V (c)

Concerning the PDOS reported in figure 6.14, the most evident fact is that the transport is mainly determined by the molecular channel states, as expected from theory. Ineed, this is evident at low bias (fgure 6.14 – b). The PDOS in the contacts is periodic (vertical lines) that is expected since in metal electrodes Bloch states, that are periodic in space, are expected. In addition, in the region of the device where the molecule is placed, there are few electron states. Since from mesoscopic system theory it is well known that transport is mainly determined by the region of the device in which there are less electron states (that is like a “bottleneck” for transport), one concludes that at low bias the transport is mainly determined by the molecule. Concerning the figure 6.14 (c), additional analyses should probably be performed to extract useful information.

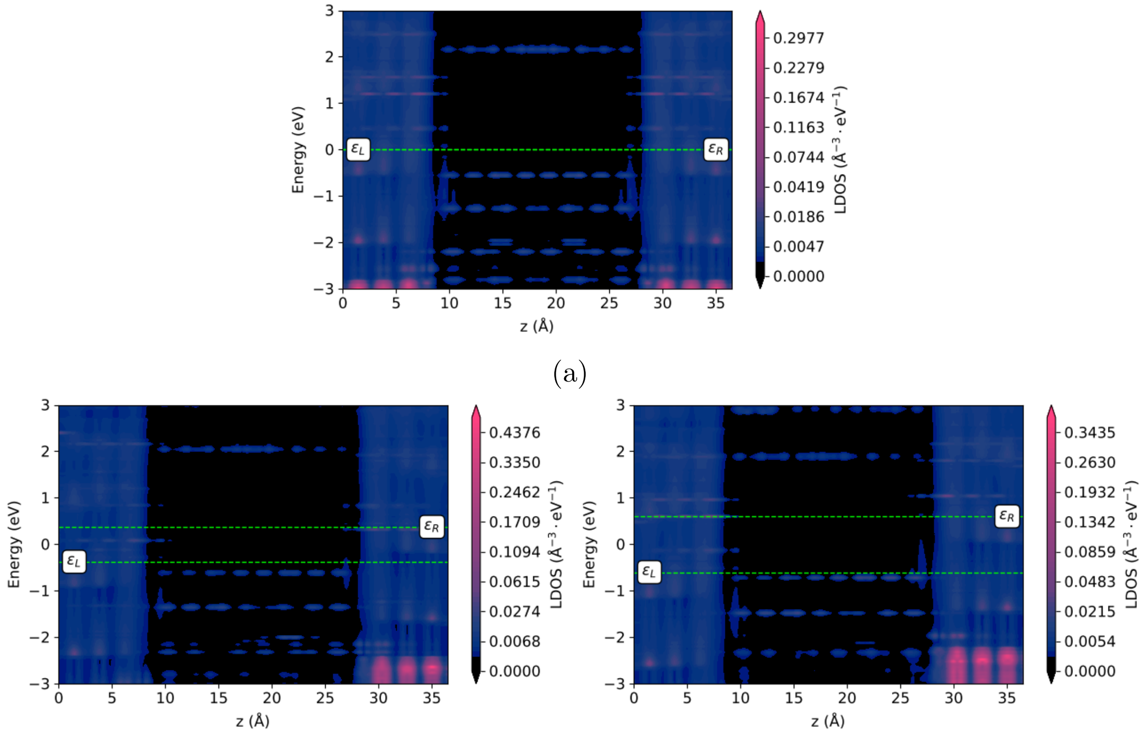

(a)

(b)

(c)

Figure 6.15: PDOS for Silver Electrodes for a bias of 0V (a), 0.6V (b) and 1.2V (c)

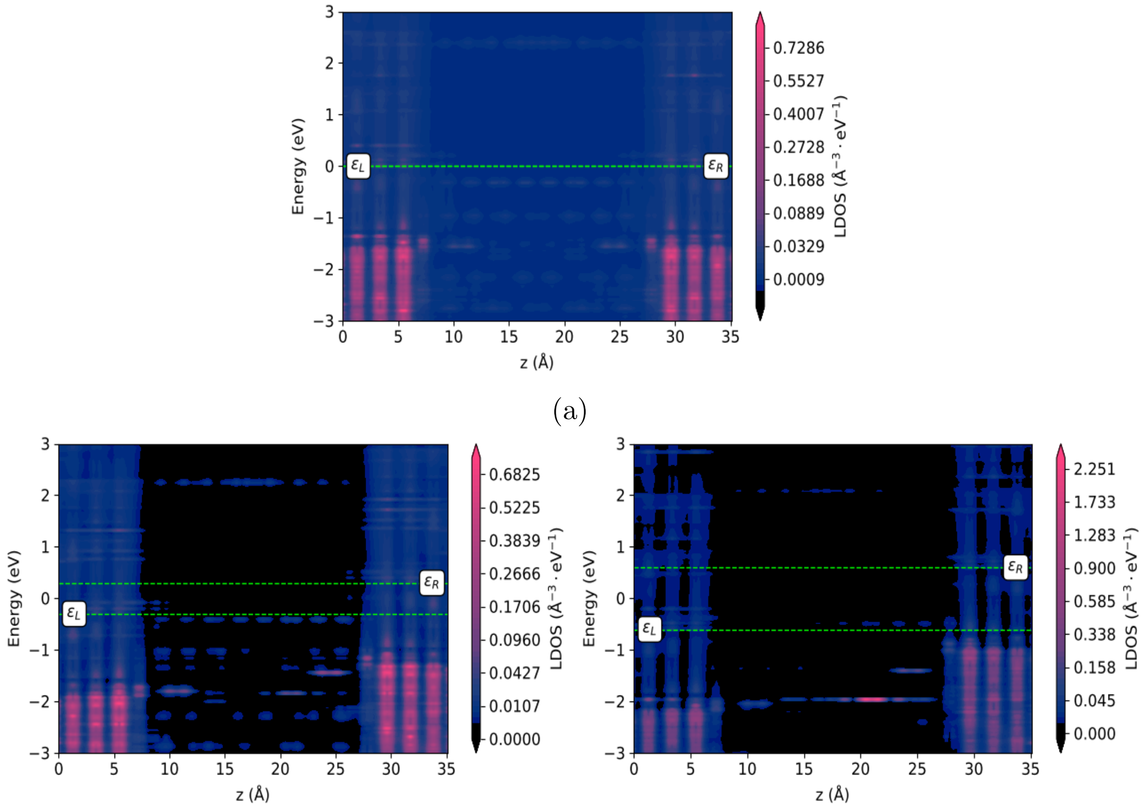

(a)

(b)

(c)

Figure 6.16: PDOS for Copper Electrodes for a bias of 0V (a), 0.6V (b) and 1.2V (c)

By comparing the PDOS with gold electrodes with those obtained with silver and copper (figures 6.15 and 6.16), and by concentrating especially on the (b) case (i.e. 0.6 V), it is possible to notice what follows. By passing from silver to gold and to copper the number of states in between the bias window are increasing in number, meaning that more and more states are involved in conduction. This explains the greater amount of current that is obtained passing from silver to gold and from gold to copper at voltage fixed at 0.6 V (see previously reported I(V) curves).

3 2TT

Just like in the last case the device configuration is shown here for various metal electrodes.

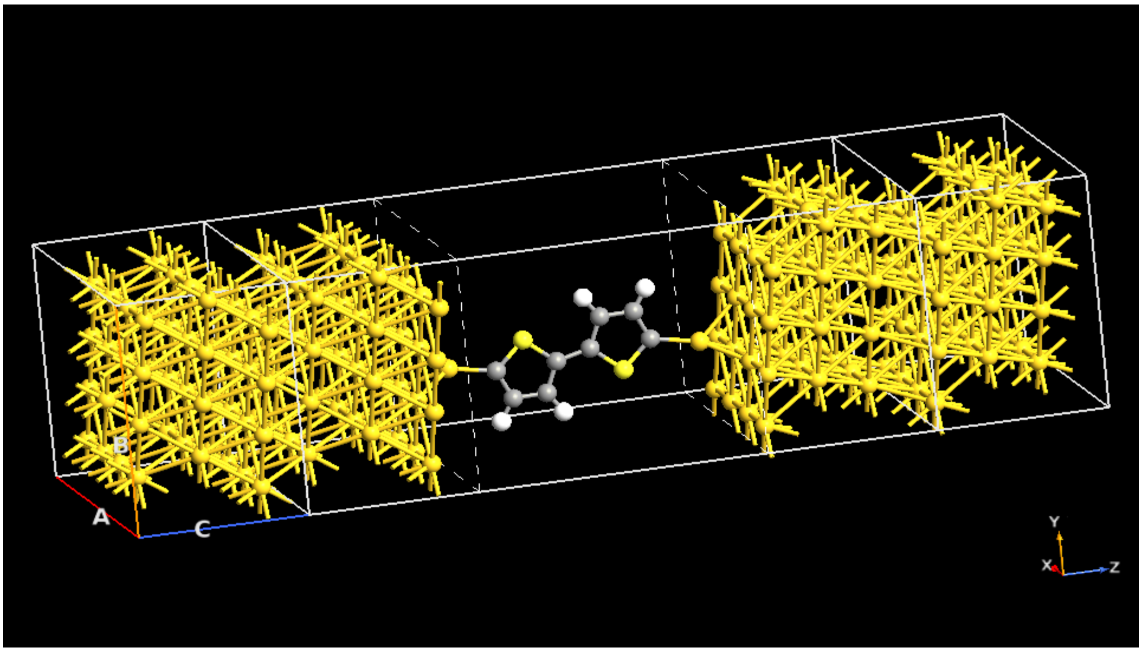

Figure 6.17: Configuration for Gold Electrodes taken from QuantumATK

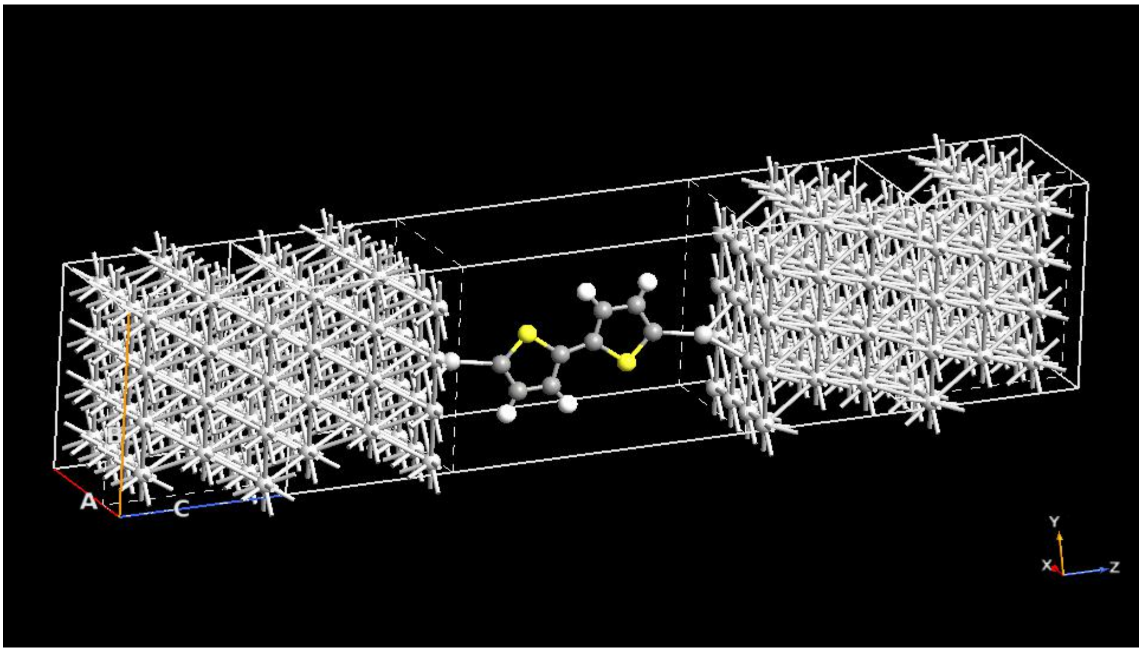

Figure 6.18: Configuration for Silver Electrodes taken from QuantumATK

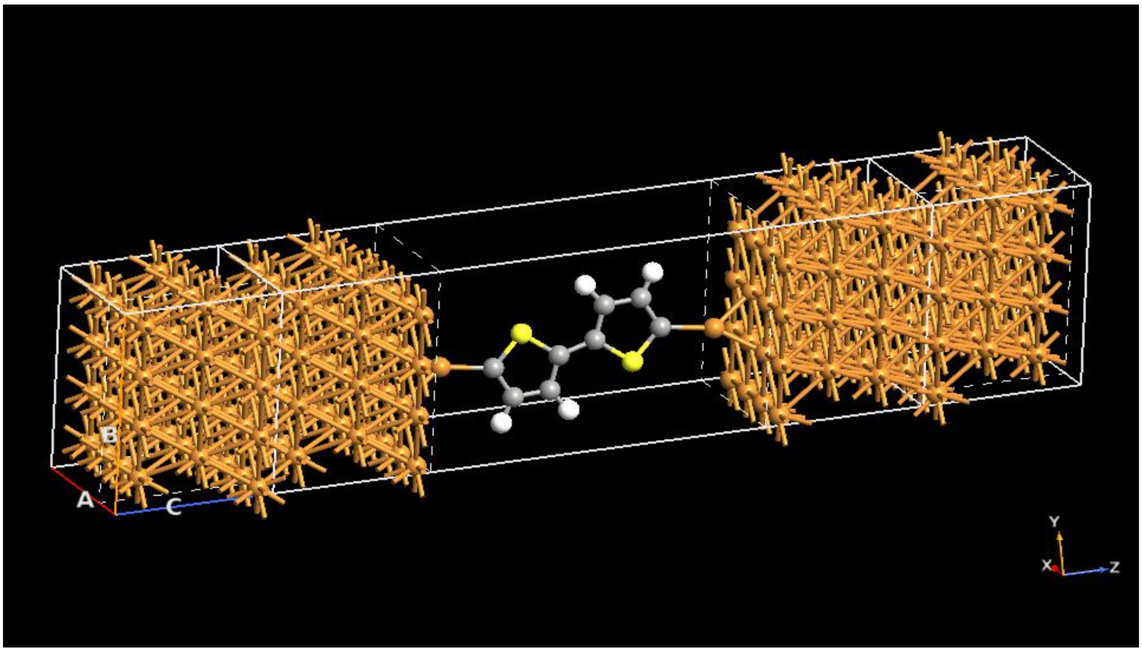

Figure 6.19: Configuration for Copper Electrodes taken from QuantumATK

The transmission spectrum(TS) and the corresponding IV curve plots are then reported below.

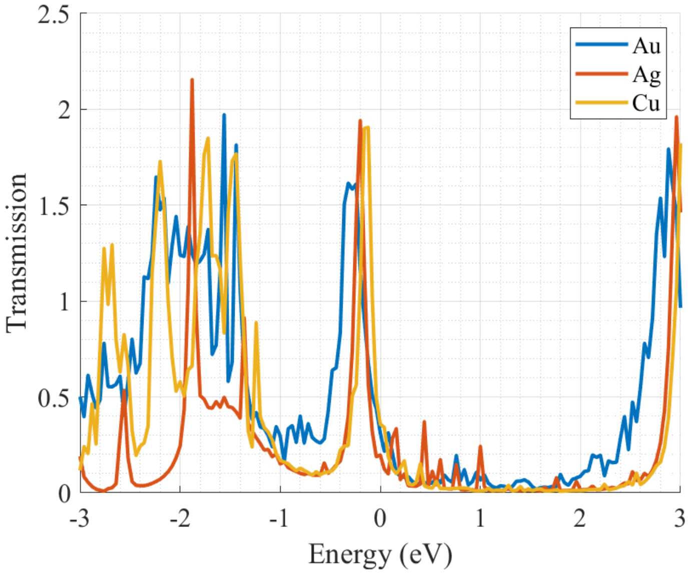

Figure 6.20: Transmission Spectrum for Metal Based Electrodes

By inspecting the transmission spectra in figure 6.20 it is possible to find a fingerprint of the contact material in the transmission spectra. Indeed, broadening is increased by passing from silver to copper to gold (as in the case of OPE3 molecule).

This is probably related to the wavefunction conjugation that is maximum with gold electrodes, and minimum with silver ones. The fact that this trend is independent from the molecule (2TT and OPE3) is a sign that it is typical of the contact material, like a sort of fingerprint of the electrode (as mentioned above). Even if in this case there are more localized states (i.e. sharp barely broadened peaks in the transmission spectra), the same trend as for OPE3 is found. Indeed, states close to Fermi level resemble discrete states of the 2TT molecule just with Lorentzian broadening, while states far below -1 eV are resembling contact DOS (that are discussed in the following).

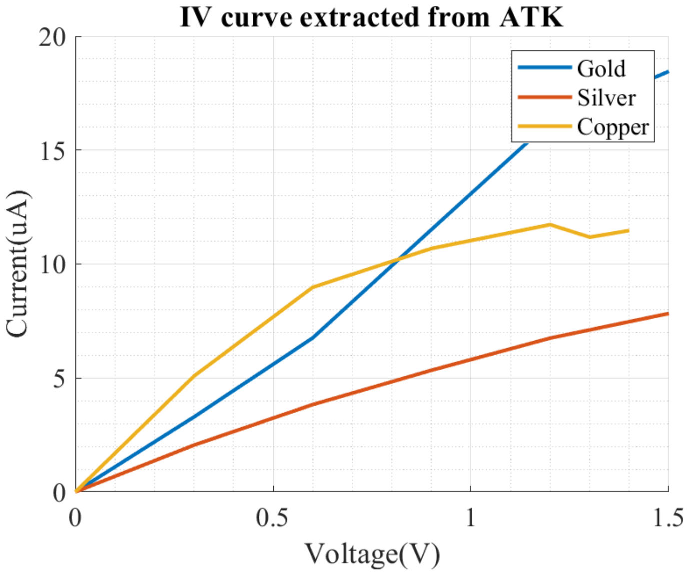

Figure 6.21: IV Curve for Metal Based Electrodes

Analogously to the OPE3 case the copper has highest current at small bias. Then, because of the inclusion of the full system HOMO peak in the bias window, current with copper electrodes saturates (after 1 V) while the current with gold electrodes increases. The latter is justified by the inclusion of a more broadened peak of transmission in the bias window for voltages above 1 V. In the case of silver, even if the HOMO peak starts to conduct in the very same way of the one with copper, since it is less broadened, it results in a smaller current for same voltages.

Differences with OPE3 case are present and are mainly related to an energy shift of the system HOMO peaks closer to Fermi levels. This is the reason of current saturation with copper at smaller voltages w.r.t. OPE3 case. These differences are probably related to intrinsic levels of the two considered molecules.

Next just we saw in the previous case the DOS was plotted and individual contribution from each shell was plotted.

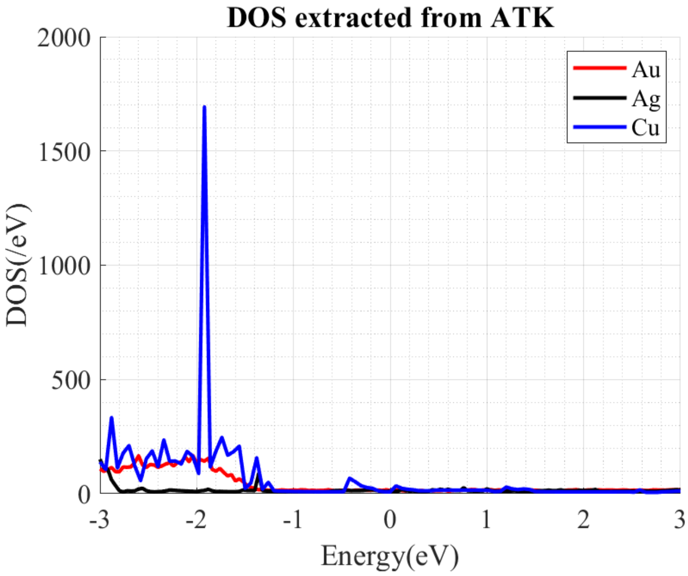

Figure 6.22: Device Denssity of States(DDOS) for Metal Based Electrodes

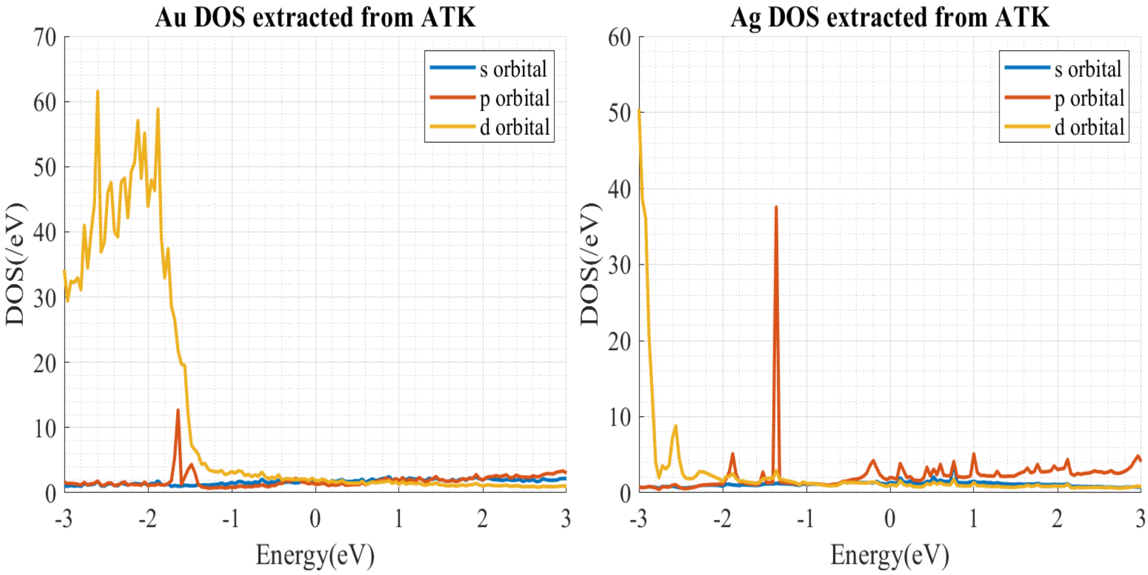

Figure 6.23: Orbital Contribution for Gold(a) and Silver(b) Electrodes

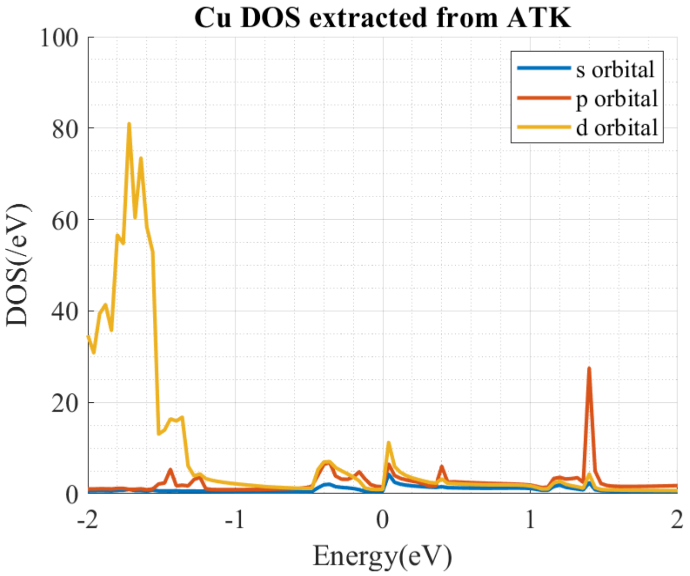

Figure 6.24: Orbital Contribution for Copper Electrodes

Coming back to the transmission spectra and the DOS, by comparing the transmission spectra of figure 6.20 with the contact DOS (figure 6.22) it is possible to confirm the same trend with OPE3 molecule: The transmission spectra peaks close to Fermi level (0 eV) are not present in the electrode DOS. This means that such peaks are related to molecular (2TT) energy levels. Indeed, they appear more spaced in energy, and less merged (i.e. more localized states) w.r.t. other transmission spectra peaks. Instead, concerning the peaks well below the Fermi level (at energies lower than -1 eV), by comparing them with the DOS of the electrodes (figure 6.22), there is good match of such transmission peaks and the contact DOS. This is likely related to a contact dominated transport mechanism: The transport is no more dominated by 2TT states but by contact states. To further confirm this, one can consider figures 6.23 and 6.24 where the contacts DOS are split in their orbital contributions. The dominant states of the contacts are d-type. The total contact DOS resembles the d-type orbital distribution in energy. This means that the dominant contribution in the contact DOS is from d-type orbital, and this reflects in the transmission spectra, exactly like in the case of OPE3. Moreover, the fact the transmission peaks below -1 eV are due to contact contribution is also evident from the peculiar shape of that states, that resembles an energy band (as expected in crystalline metal conductors) and as for the OPE3 case.

In conclusion, it can be confirmed that irrespectively from the considered molecular channel (2TT or OPE3) the contact states dominate the transmission states at low bias, while the peculiarity of the molecular channel (2TT and OPE3) is dominant close to Fermi levels (0 eV). This in turn means that for low applied biases (i.e. with a small bias window centered around 0 eV) the current is mainly dominated by molecular channel states. Instead at high bias the effect of the contacts become more important or even dominant.

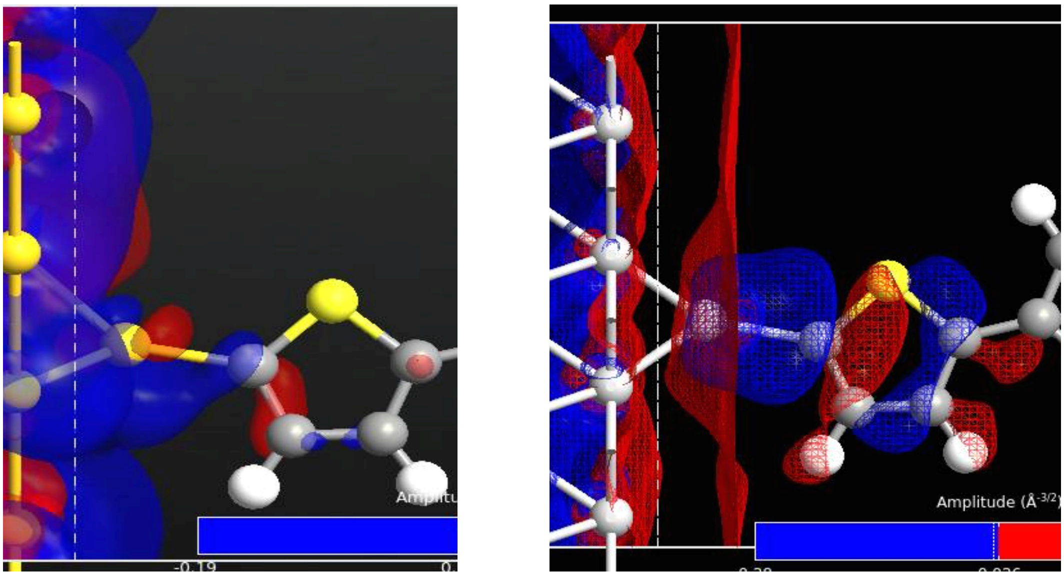

(a)

(b)

Figure 6.25: HOMO Level for Gold(a) and Silver(b) Electrodes

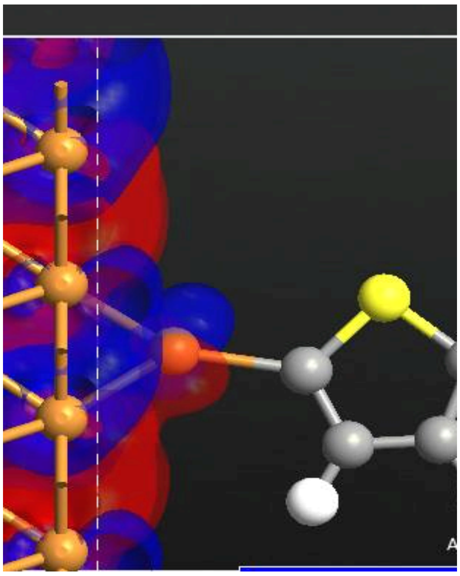

Figure 6.26: HOMO Level for Copper Electrodes

Same considerations hold for the system orbital also in the case of 2TT. Indeed, also in this case d-type orbitals within the contacts are not well merged, i.e. conjugated, with the 2TT p-type ones. Indeed, there are barriers (i.e. absence of iso-surfaces) at the contact-molecule interface. Again, according to the basic chemistry principle of maximum overlap of orbitals, there is not enough overlap between d-type contact orbitals and p-type 2TT ones, resulting thus in a break of the conjugation. This confirms that, irrespectively from the molecular channel, metal electrodes are not the best ones if the final purpose is to have perfect conjugation of orbitals. This indeed might reduce the maximum saturation current that can be obtained with metal electrodes through coherent tunneling.

Next, the MPSH states will be shown at the transmission peaks at equilibrium.

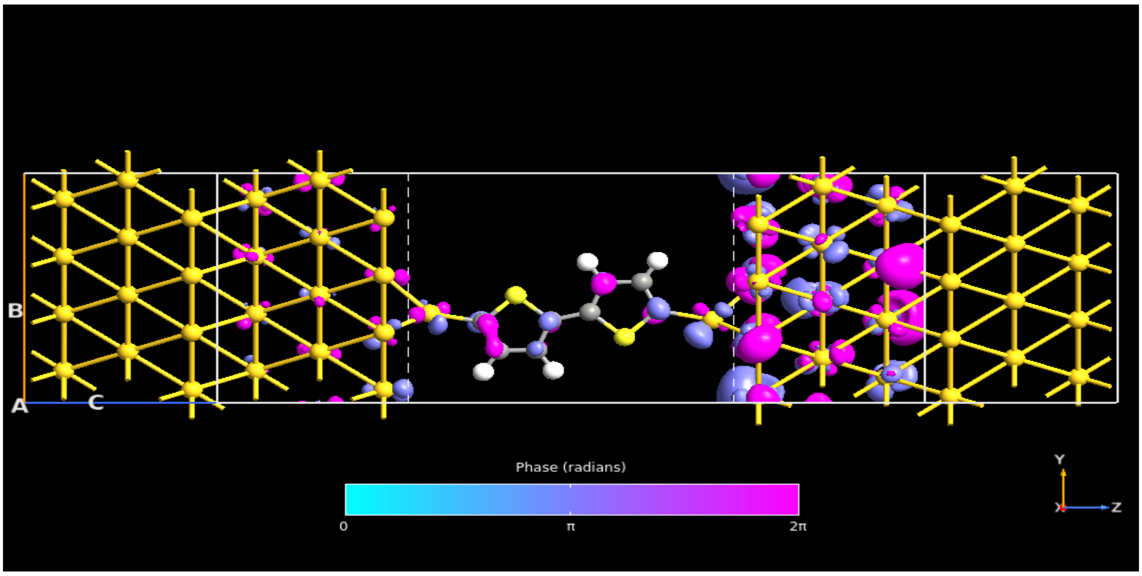

Figure 6.27: MPSH for Gold Electrodes

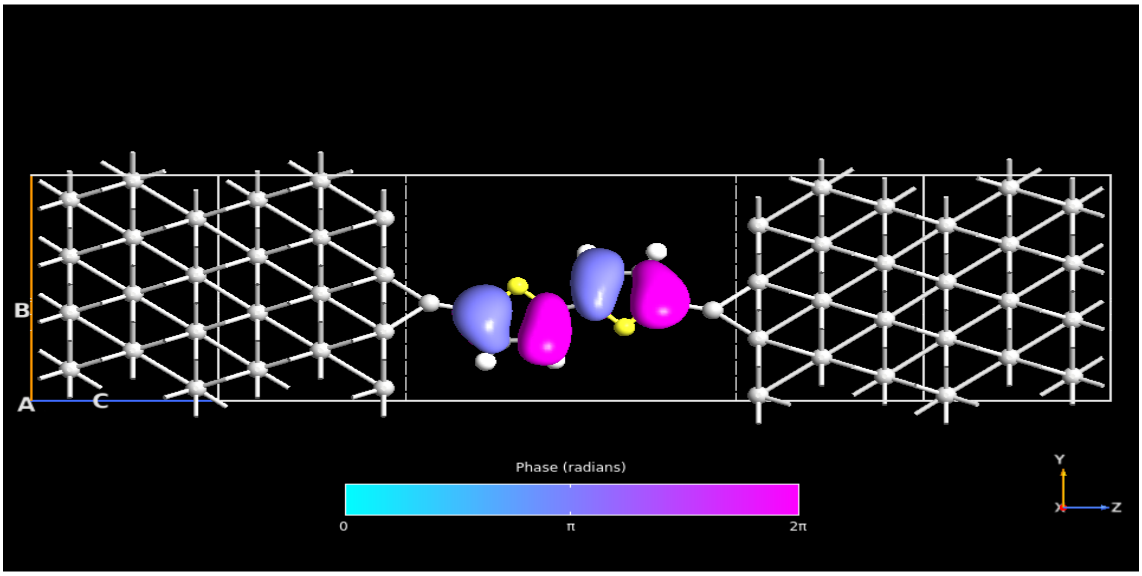

Figure 6.28: MPSH for Silver Electrodes

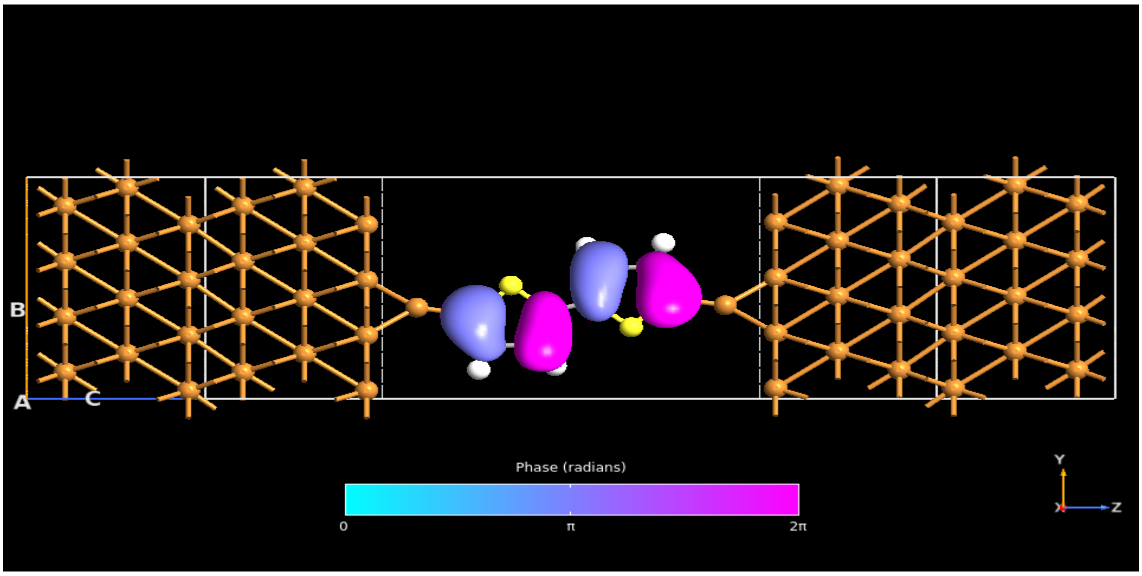

Figure 6.29: MPSH for Copper Electrodes

Same considerations for the OPE3 case hold also in the 2TT case. In figures 6.27, 6.28, 6.29 the main transmission eigenstates of the system HOMO contributing to the transmission peaks in the transmission spectra are reported. In all the three cases transmission occurs through molecular states, even if this is more evident for silver and copper. In all cases there is non-negligible iso-surface of transmission through the 2TT molecule, meaning that is relevantly contributes to transmission. In the case of gold, this is less marked, but comparable iso-transmission surfaces are present in the 2TT and in the drain electrode (left), meaning that transport occurs through the 2TT. In the case of silver and copper, the 2TT is enveloped by the transmission eigenstate lobes, meaning that it totally determines the transmission properties of the system. These analyses again confirm that the transmission peaks closest to Fermi level in the transmission spectra reported previously are related to molecular channel states.

Finally, the PDOS are visualized for metal electrodes with 2TT molecule.

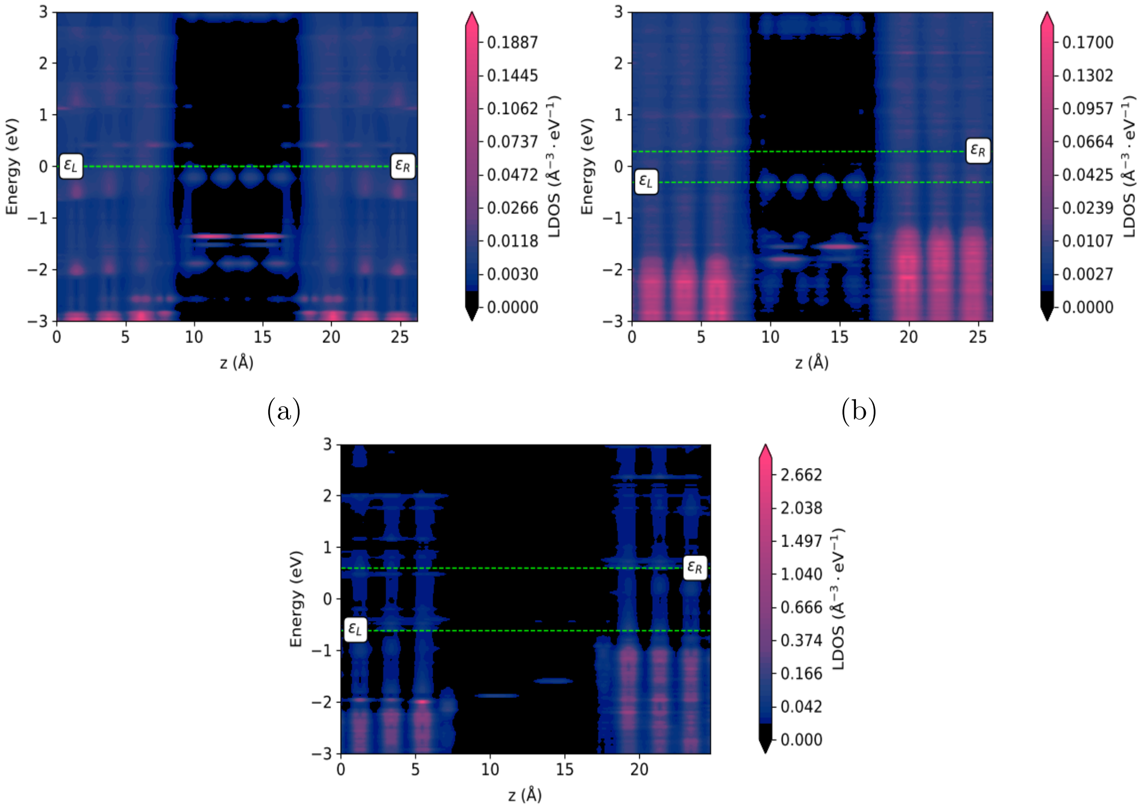

(a) (b)

(c)

Figure 6.30: PDOS for Gold Electrodes for a bias of 0V(a) ,0.6V (b) and 1.2V (c)

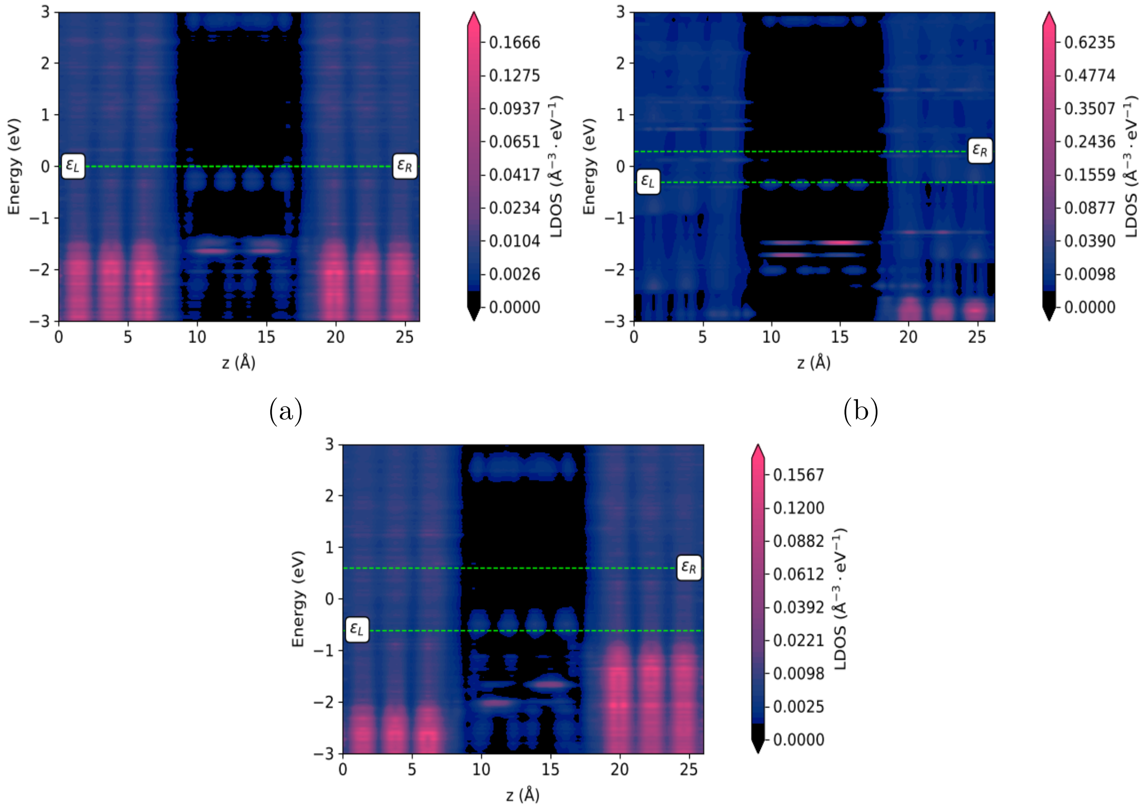

(a)

(b)

(c)

Figure 6.31: PDOS for Silver Electrodes for a bias of 0V(a), 0.6V (b) and 1.2V (c)

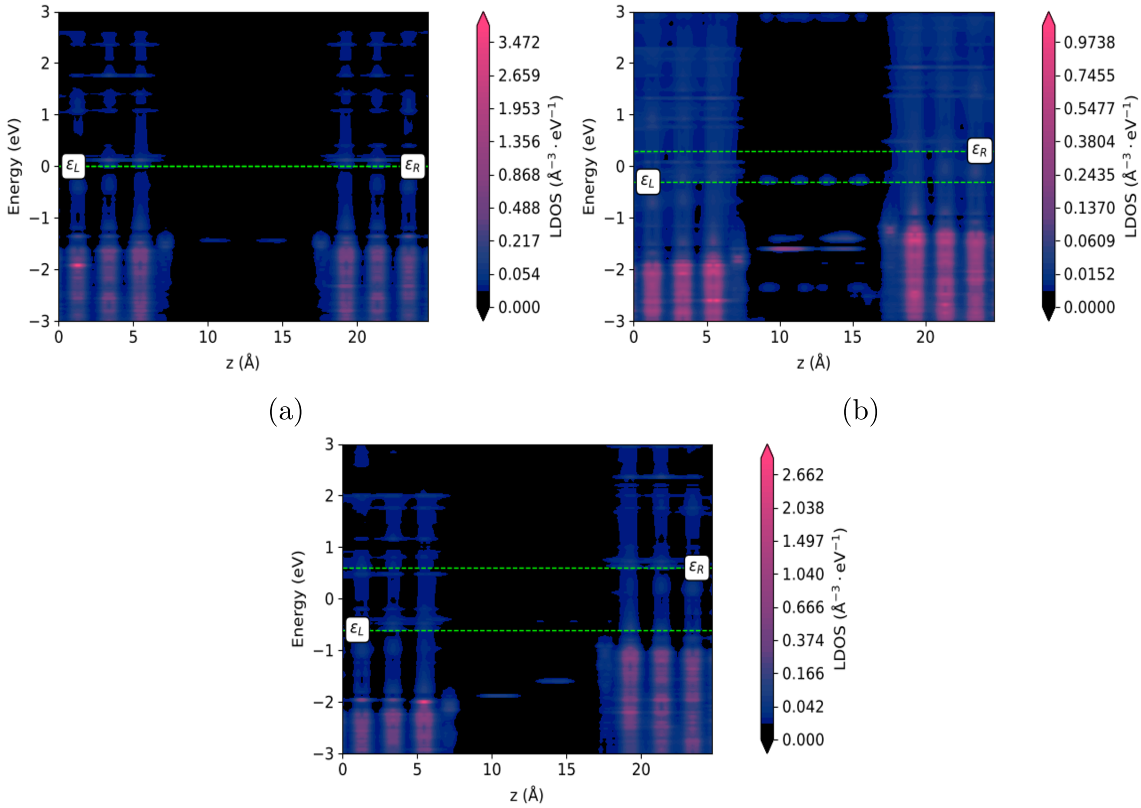

(a)

(b)

(c)

Figure 6.32: PDOS for Copper Electrodes for a bias of 0V (a), 0.6V (b) and 1.2V (c)

Similar considerations hold again for 2TT meaning that a fingerprint of the electrodes is evident in the PDOS. The transport results mainly determined by the molecular channel states, as expected from theory. The PDOS in the contacts is again periodic (vertical lines) as expected since in metal electrodes Bloch states, that are periodic in space, are present. In addition, in the region of the device where the molecule is placed, there are few electron states. Since from mesoscopic system theory it is well known that transport is mainly determined by the region of the device in which there are less electron states, one concludes that at low bias the transport is mainly determined by the molecule (figure 6.30 b). In this case the same considerations are evident and present also for figures 6.31, 6.32. By passing from silver to gold and to copper the number of states in between the bias window are increasing in number, meaning that more and more states are involved in conduction. This explains the greater amount of current that is obtained passing from silver to gold and from gold to copper at voltage fixed at 0.6 V (see previously reported I(V) curves). Pay attention to the scale of the considered graphs to avoid misinterpretation.

Chapter 7

Graphene-based Electrodes Analysis

Next, I move on to the graphene case wherein two types of zigzag graphene nano ribbons(ZGNR) viz. number of atoms(N) = 4 and N = 10 were studied. Since for a good current flow we want a big reservoir of electrons the case of N = 10 was included in the analysis. And then lastly graphene nanosheet(GNS) electrodes were used. For the central region the same two molecules that were discussed in the previous chapter were used namely OPE3 and 2TT. Using QuantumATK DFT simulations was performed to obtain three main quantities the transmission spectrum T(E), the density of states(DOS) and the IV Curve.

As it was mentioned in the metal based electrodes section while trying to reproduce the results for GNS electrodes convergence was not reached easily. At first number of k-points were increased along with trying different values for the iteration control block which was not fruitful. Then the boundary conditions were changed from Dirichlet to Neumann although convergence was better than previous case still high biases was a problem. More complex pseudopotentials were used (OMX-High) but even these did not lead to convergence at high biases. Finally the problem was solved by increasing the length of the electrodes reducing the tolerance and increasing the number of steps. The following table shows the settings that were used:

Table 7.1: ATK DFT-LCAO equilibrium calculator settings.(ZGNR)

LCAO Calculator	
LCAO Basis Set	Exchange Correlation: GGA-PBE Basis Set: DZP
Numerical Accuracy	k point: $1 \times 5 \times 200$ Density Mesh Cutoff: 75K
Iteration Control	Tolerance: 1e-5 Maximum Steps: 300 Damping Factor = 0.01 History Steps = 5
Device Algorithm	Default
Contour integral parameter	Default
Poisson Solver	Type: [Parallel] Conjugate Gradient Front,Back,Top,Bottom: Periodic Left, Right: Dirichlet

These settings were used for all configurations except for graphene nanosheets(GNS) case for both the molecules, changed settings are mentioned below:

Table 7.2: ATK DFT-LCAO equilibrium calculator settings.(GNS)

LCAO Calculator	
LCAO Basis Set	Exchange Correlation: GGA-PBE Basis Set: DZP
Numerical Accuracy	k point: $1 \times 4 \times 401$ Density Mesh Cutoff: 75K
Iteration Control	Tolerance: 1e-4 Maximum Steps: 1500 Damping Factor = 0.01 History Steps = 5
Device Algorithm	Default
Contour integral parameter	Default
Poisson Solver	Type: [Parallel] Conjugate Gradient Front,Back,Top,Bottom: Periodic Left, Right: Neumann

1 OPE3

The device configuration for various cases is shown in the following figures:

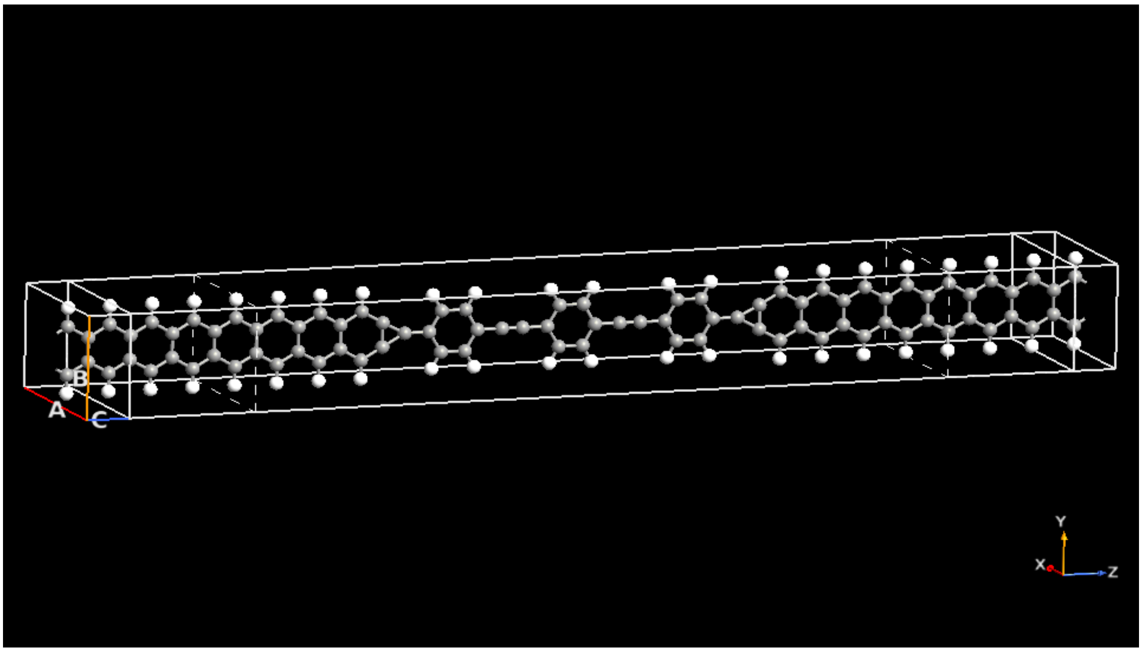

Figure 7.1: Configuration for ZGNR (N = 4) based electrodes

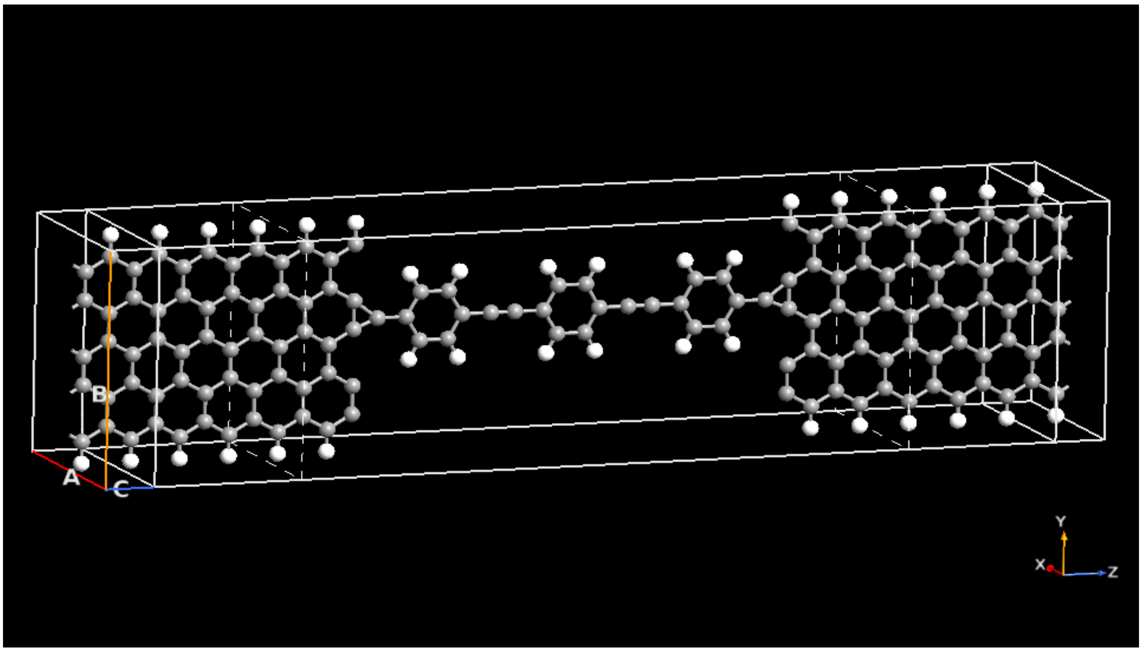

Figure 7.2: Configuration for ZGNR (N = 10) based electrodes

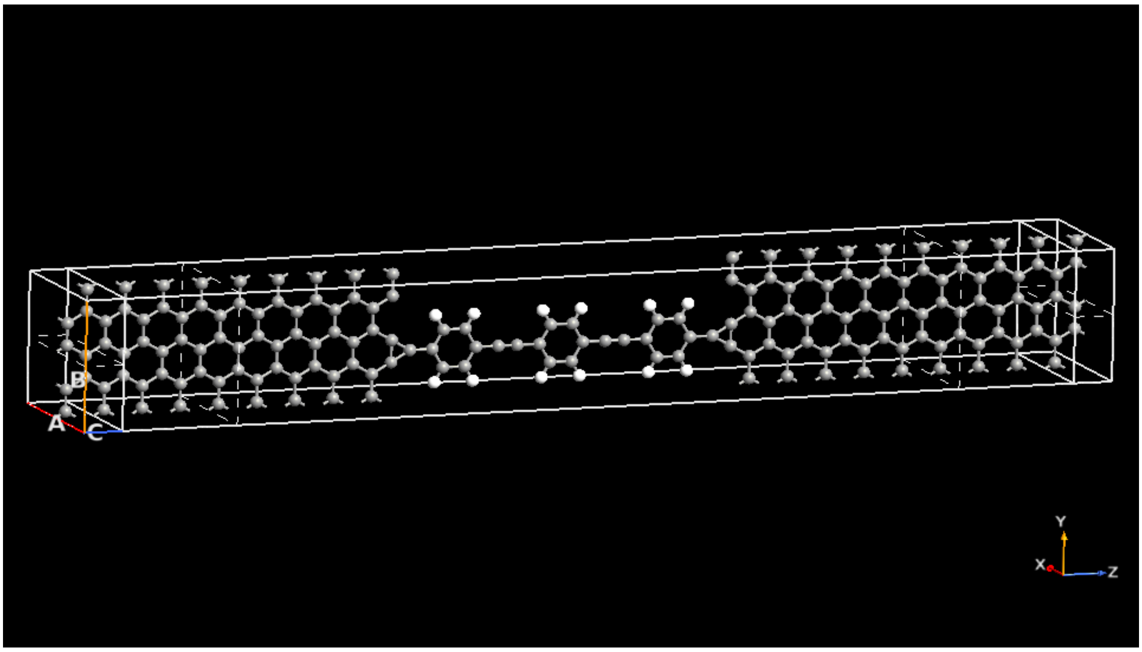

Figure 7.3: Configuration for GNS based electrodes

Firstly the transmission spectrum T(E) is reported and the plots obtained for this case are shown below:

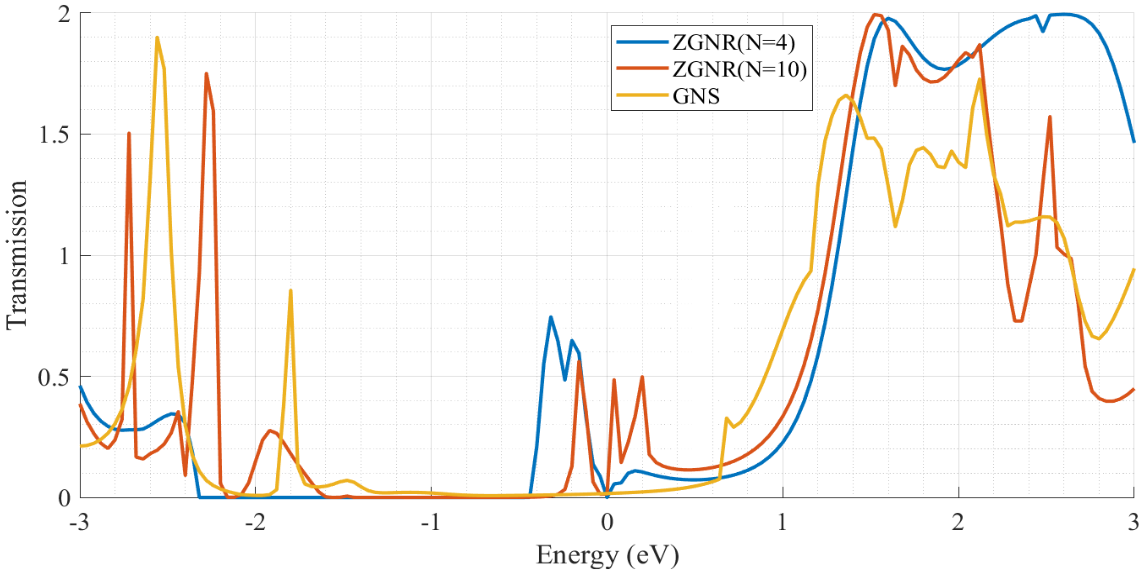

Figure 7.4: Transmission Spectrum for Graphene Based Electrodes

In the case of graphene contacts differences are evident w.r.t. metal contacts. In particular, transmission peaks below Fermi level are less broadened w.r.t. ones above it. It is evident an overall transmission band (i.e. widely broadened and merged transmission peaks) above the Fermi level (0 eV). By comparing the transmission spectra with the graphene contact DOS it is possible to link the transmission spectra shape to the graphene DOS in all the three considered cases (GNS, ZGNR 4, ZGNR 10), meaning that the graphene states are strongly involved in conduction at all the voltages. It is less evident the exclusive behavior of the molecule. Additional comments are reported after the current-voltage analysis

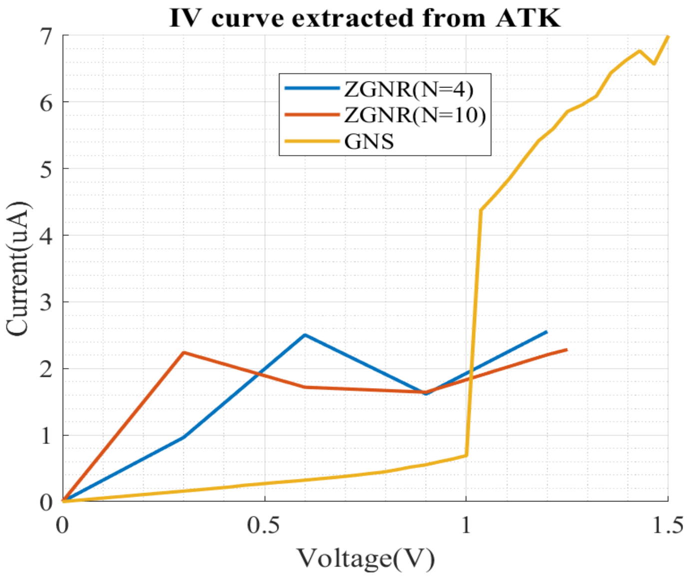

Figure 7.5: IV Curve for Graphene Based Electrodes

In figure 7.5 is reported the I(V) curve. Since more broadened peaks in the transmission spectra are present slightly above the Fermi energy with ZGNR 10 than with ZGNR 4, the current increases sharply in the first case than in the second one. Nevertheless, at saturation, since the ZGNR 4 transmission peak is more broadened the current result higher. Furthermore such current saturation occurs for lower voltage with ZGNR 10 than ZGNR 4 because of the full inclusion of the transmission peaks at lower voltages (i.e. smaller bias window). It is interesting that with GNS there are very few transmitting states around Fermi level (0 eV), while above 0.5 eV there are plenty very broadened states conducting. This probably means that molecule (OPE3) states are not influencing much the transport. Indeed, if we relate the transmission peaks close to Fermi level to molecule levels as in the case of metal contacts, we notice that with GNS there are essentially no conducting states related to OPE3. And thus GNS starts conducting for voltages above 1 V when the main LUMO peaks are included in the bias window. To confirm such trend an analysis of contact DOS is performed. An additional analysis of molecular PDOS should also be performed in a future work to additionally confirm the considerations just made.

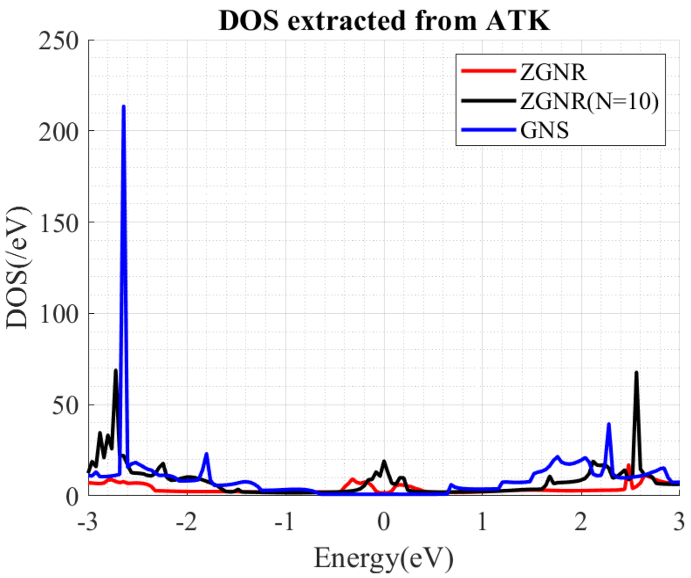

Figure 7.6: Device Denssity of States(DDOS) for Graphene Based Electrodes

In figure 7.6 the graphene contact DOS are reported. To better investigate their intriscic features they are analyzed in terms of composing orbitals in figures 7.7, 7.8.

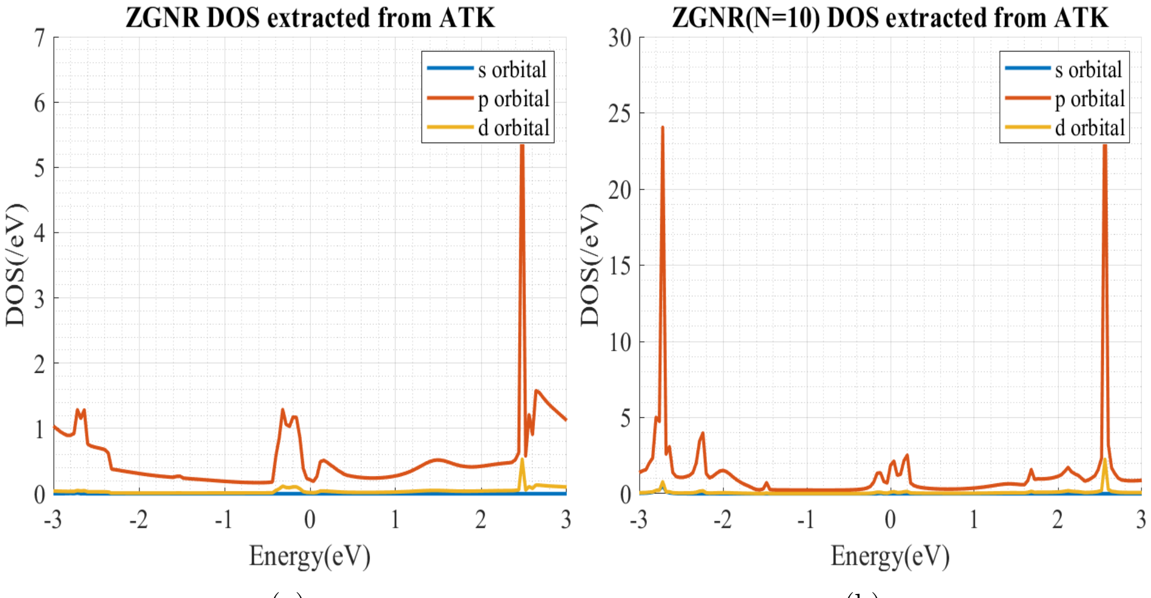

(a) (b)

Figure 7.7: Orbital Contribution for ZGNR N=4 (a) and ZGNR N=10 (b) Electrodes

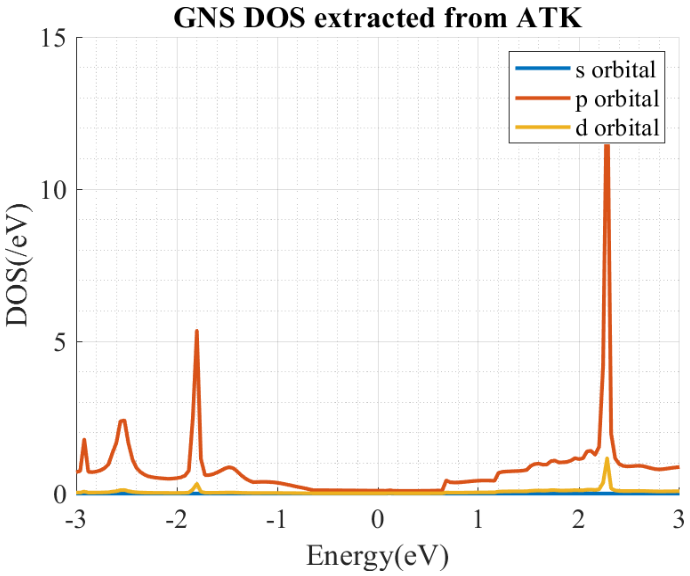

Figure 7.8: Orbital Contribution for GNS

By comparing the DOS of figures 7.7. and 7.8 with the transmission spectra reported previously, it is evident that the transmission in the case of graphene electrodes is dominated by the contact p-type orbitals. Indeed, their DOS are very well matching the transmission spectra shapes, beside an amplification factor due to transmission probability of these states. In the case of ZGNR 4 and ZGNR 10 there are p-type states close to Fermi level, that are transmitting as evident in the transmission spectra. Instead, in GNS case such p-type states are not present. Additional analysis about the total DOS of the system and the molecular PDOS contributions should be performed in future works to understand the origin of the electron states close to Fermi level in the ZGNR cases, that are not present in an semi-infinite graphene contact (GNS).

Now, the orbitals will be visualized for HOMO level at equilibrium.

ZGNR(N=4)

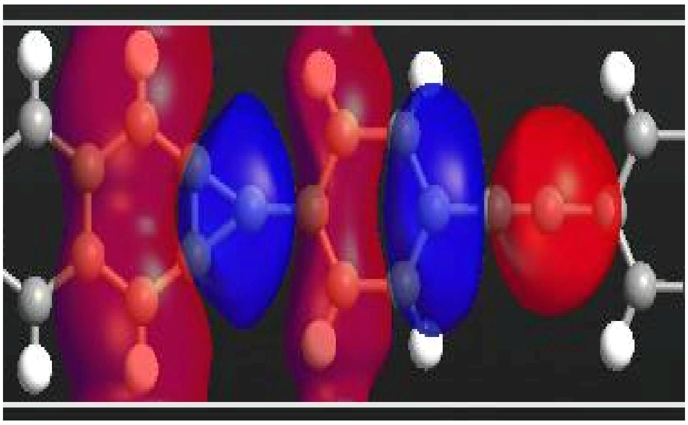

Figure 7.9: HOMO Level

ZGNR(N=10)

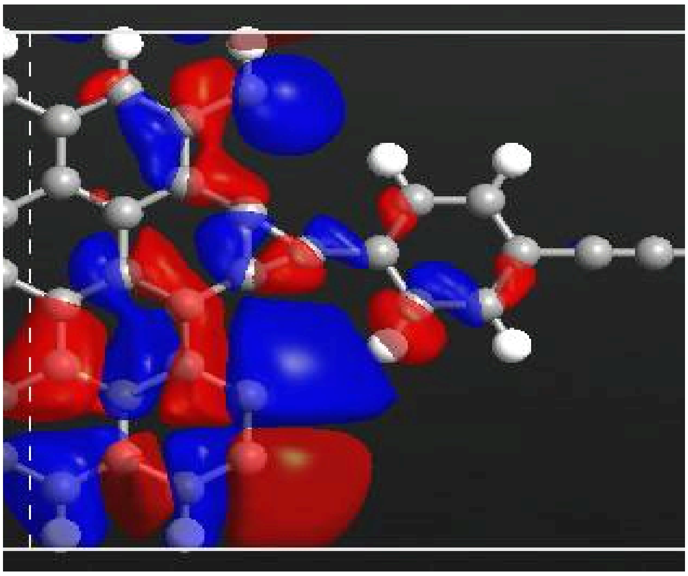

Figure 7.10: HOMO Level

GNS

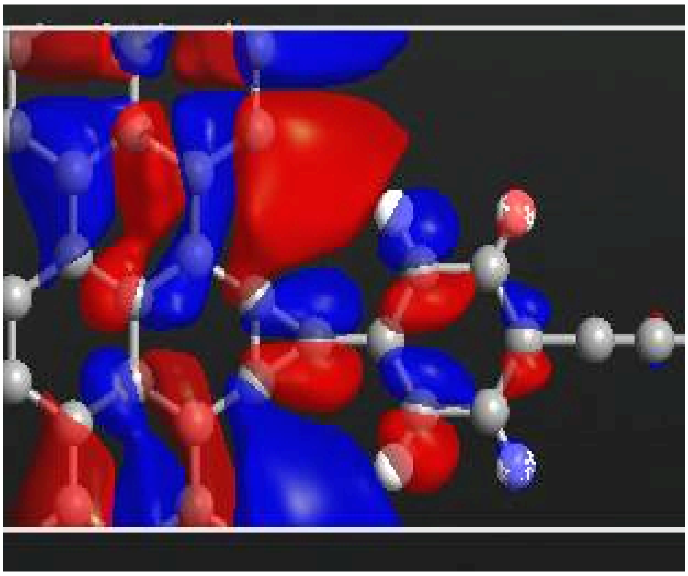

Figure 7.11: HOMO Level

From an orbital analysis (figures 7.9, 7.10, 7.11) it is evident that the p-type shape of the orbitals is dominant in all the considered types of graphene contacts. In addition, there is good conjugation and delocalization of orbitals between the graphene contacts and the OPE3 molecule. This is in agreement with the principle of maximum overlap of orbitals. Additional analyses should be performed to clarify the different delocalization and conjugation in the three cases. Nevertheless, the greater conjugation/delocalization explain also the greater current that is obtained w.r.t. metal electrodes, at least for small bias and for ZGNR 4 and ZGNR 10 cases (related to states close to Fermi level).

For a better visualization of the available states PDOS was also calculated which gives a representation of the available states resolved in space and energy.

The plots for PDOS also complement the IV curve as we can see from the following plots.

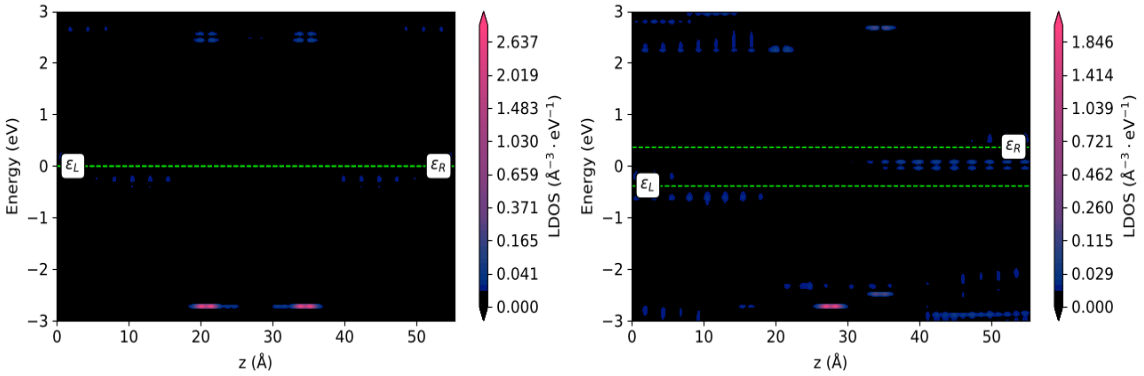

(a)

(b)

Figure 7.12: PDOS for ZGNR (N=4) Electrodes for a bias of 0V (a) and 0.6V (b)

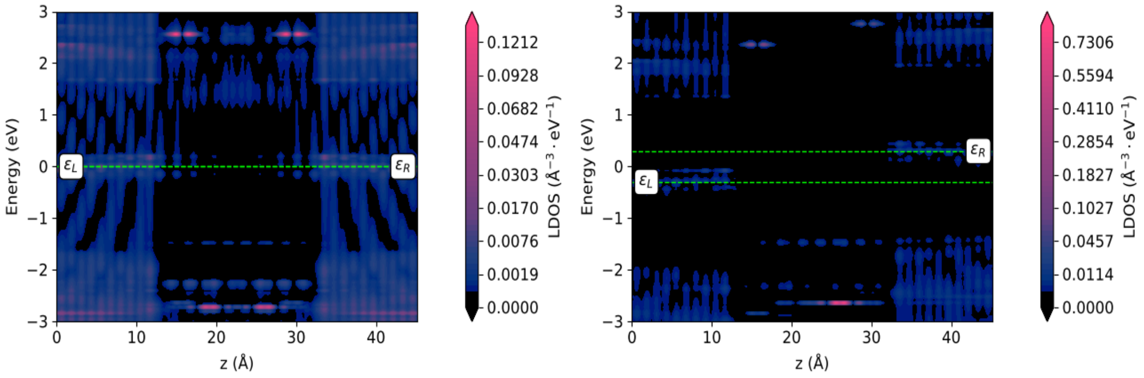

(a)

(b)

Figure 7.13: PDOS for ZGNR (N=10) Electrodes for a bias of 0V (a) and 0.6V (b)

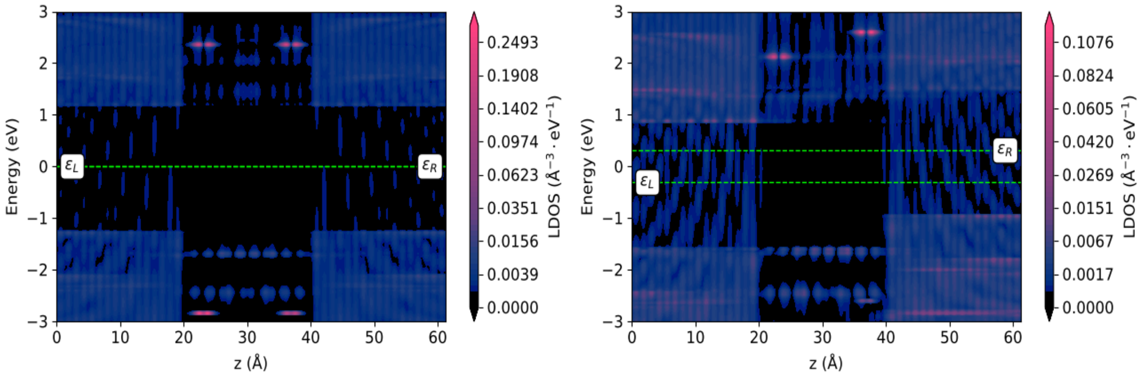

(a)

(b)

Figure 7.14: PDOS for GNS Electrodes for a bias of 0V (a) and 0.6V (b)

The PDOS inspection (figures 7.12, 7.13, 7.14) shows that for ZGNR 4 and ZGNR 10 the electrode states are dominating the transmission, since there are negligible states within the gap between the electrodes, so no relevant molecule state is conducting. The only possibility is that contact states are provoking the coherent tunneling through the molecular breakjunction, and because of the good conjugation of orbitals, no destructive interference of transmission states occurs, and thus the electron are coherently and successfully transmitted from source to drain. This matches again the considerations of before regarding the origin of the transmission states close to Fermi level for the ZGNR 4 and ZGNR 10 cases. Notice that again in the electrodes the PDOS are periodic in space, meaning that also in the graphene electrodes there are periodic Bloch states. In the case of GNS, the absence of transmission states close to Fermi energy is confirmed by the smaller number of electron contact (left and right regions) states in the PDOS, that are one order of magnitude less w.r.t. ZGNR 4 and ZGNR 10 cases. This further confirm the smaller current obtained with GNS for voltages below 1 V (in the plot the considered voltage is 0.6 V).

2 2TT

Just like in the previous cases first the device configuration is shown here for graphene based electrodes.

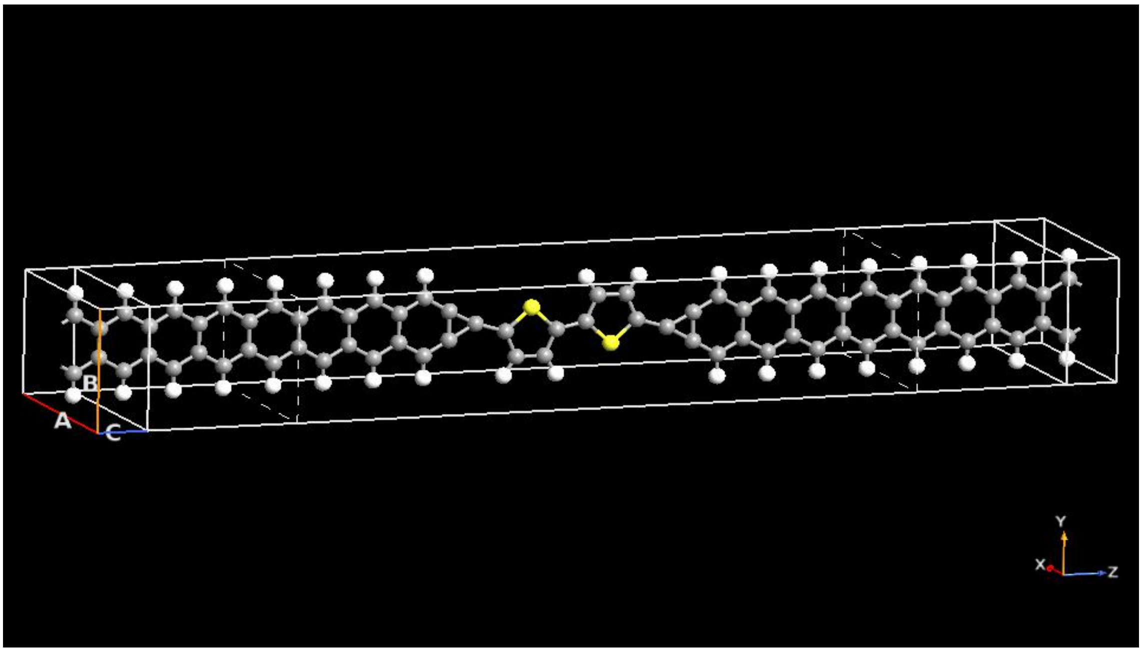

Figure 7.15: Configuration for ZGNR (N = 4) based electrodes

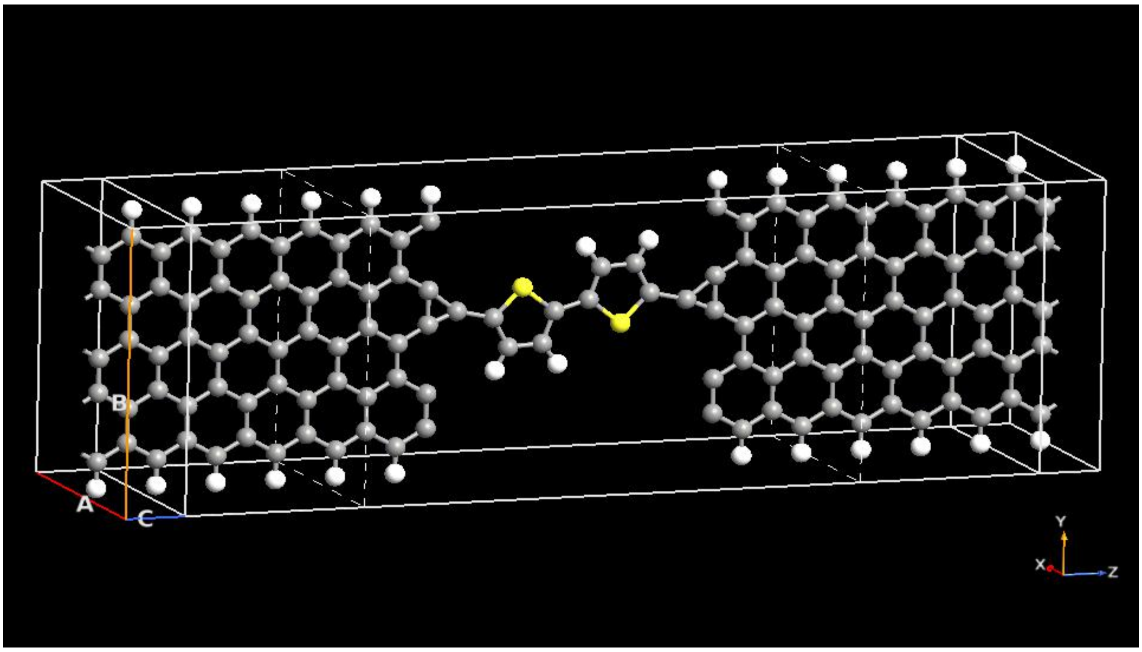

Figure 7.16: Configuration for ZGNR (N = 10) based electrodes

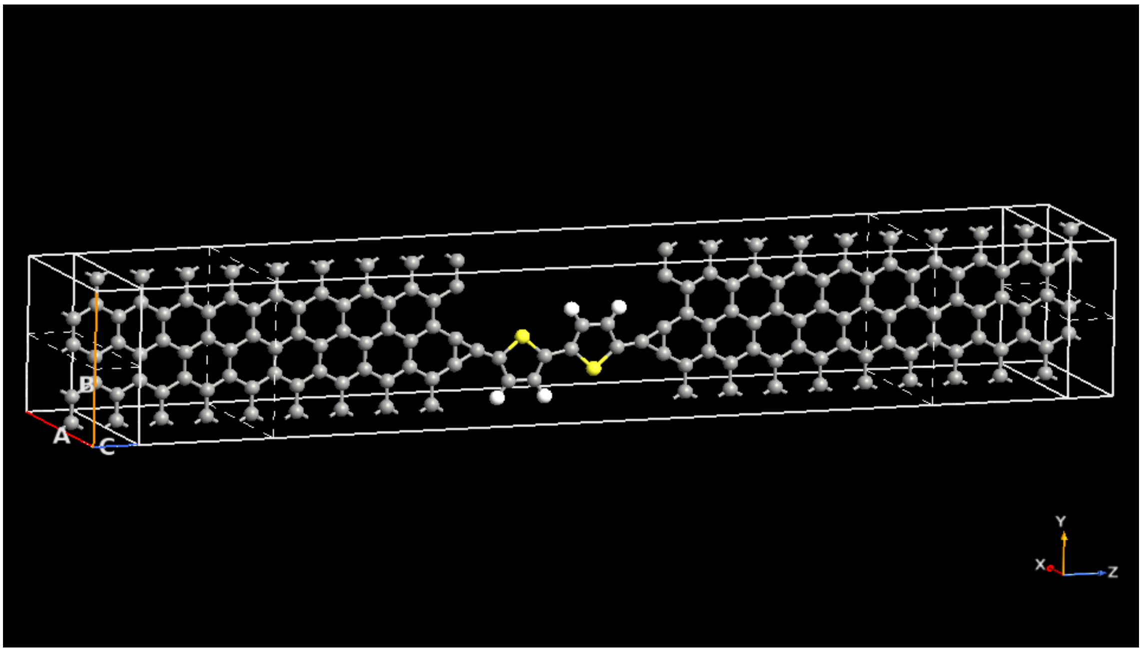

Figure 7.17: Configuration for GNS based electrodes

In the case of 2TT, very same considerations hold in the case of ZGNR 4, ZGNR 10 and GNS electrodes. The transmission spectra, their relation to contact DOS and PDOS and finally the obtained I(V) curves can be explained in a similar fashion w.r.t. OPE3 case. This is again a confirmation of the fact that the already pointed out features are a fingerprint of graphene electrodes over the total system transport, and the role of the considered molecule (2TT vs OPE3) is probably minor, especially in the GNS case. In the following such plots are reported. Comments are avoided for the sake of brevity.

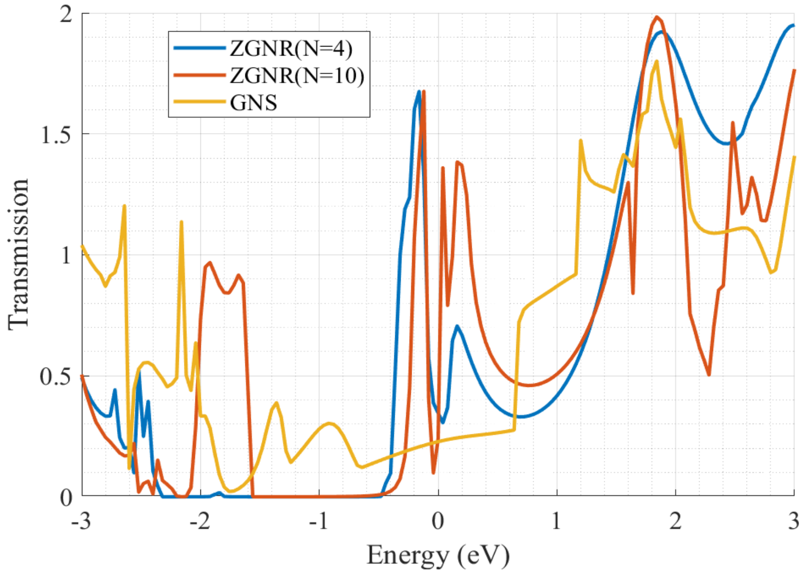

Figure 7.18: Transmission Spectrum for Graphene Based Electrodes

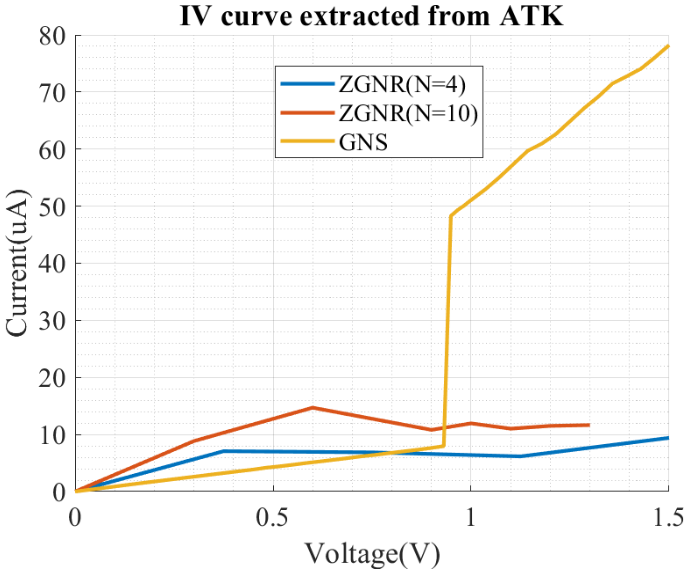

Figure 7.19: IV Curve for Graphene Based Electrodes

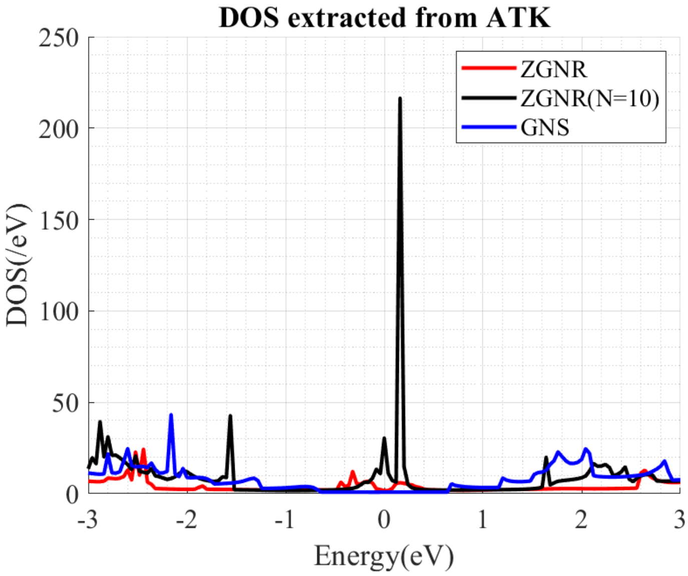

Figure 7.20: Device Denssity of States(DDOS) for Graphene Based Electrodes

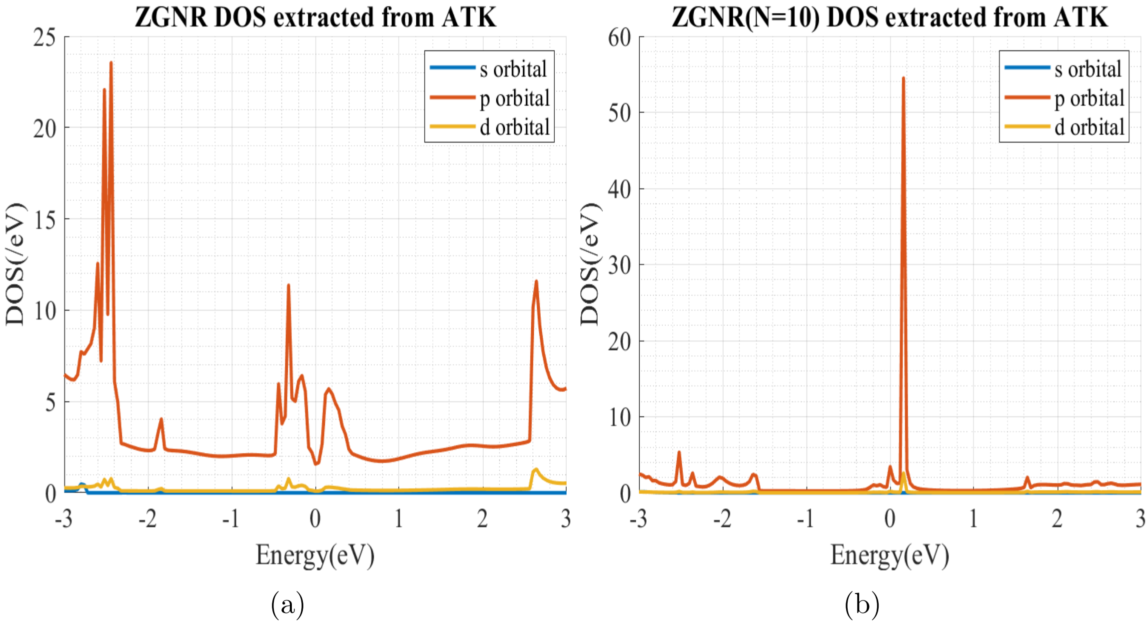

(a) (b)

Figure 7.21: Orbital Contribution for ZGNR N=4 (a) and ZGNR N=10 (b) Electrodes

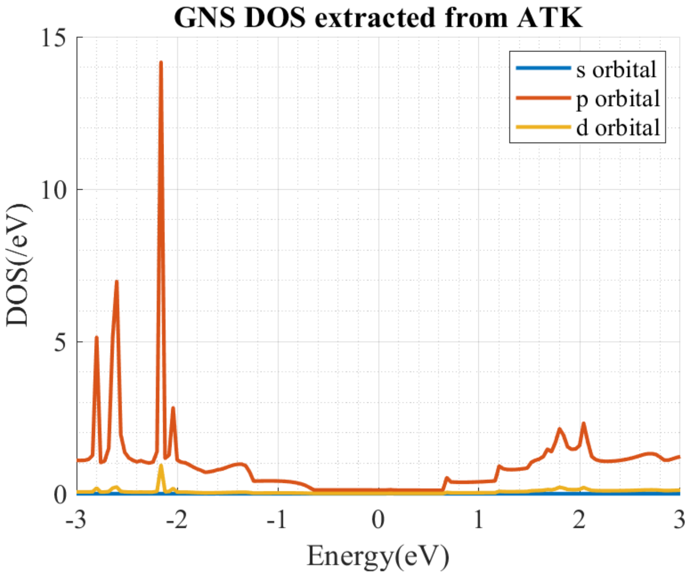

Figure 7.22: Orbital Contribution for GNS

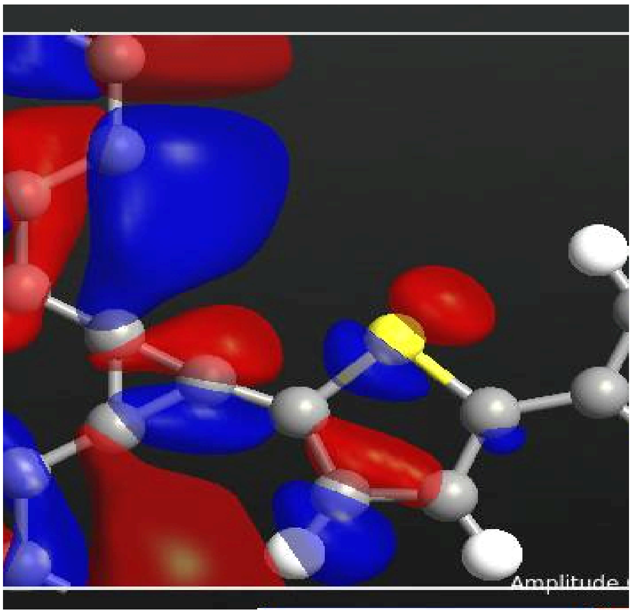

Figure 7.23: HOMO Level for ZGNR(N=4) at equilibrium

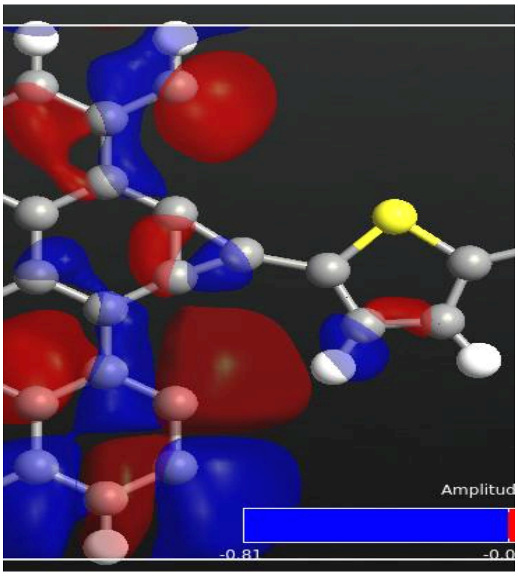

Figure 7.24: HOMO Level for ZGNR(N=10) at equilibrium

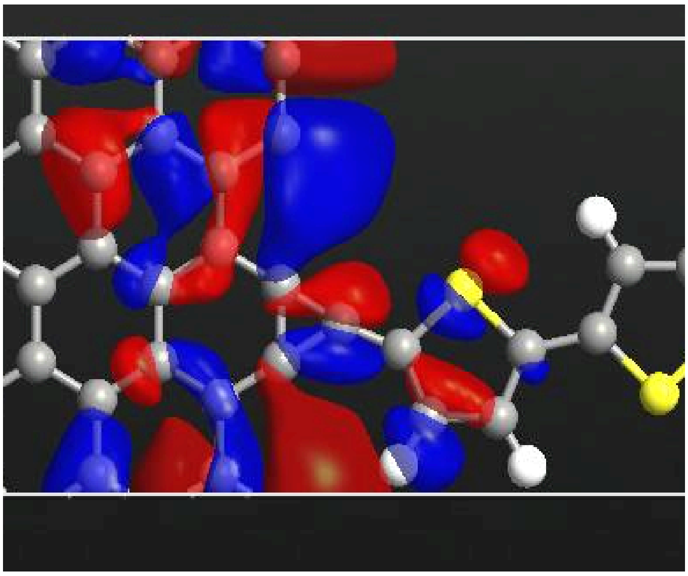

Figure 7.25: HOMO Level for GNS at equilibrium

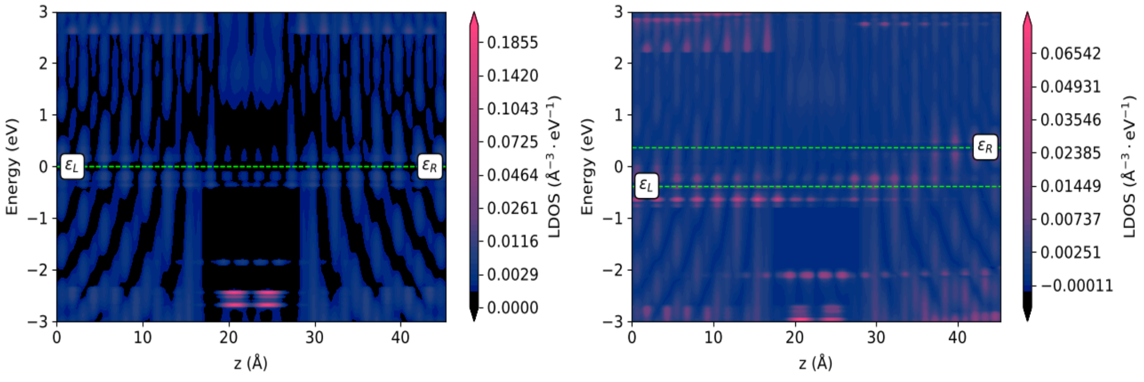

(a) (b)

Figure 7.26: DOS for ZGNR (N=4) Electrodes for a bias of 0V (a) and 0.6V(b)

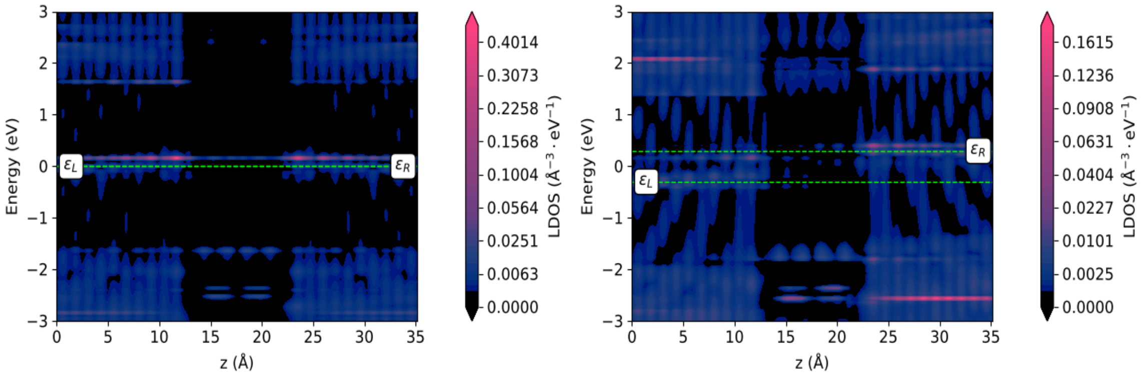

(a) (b)

Figure 7.27: DOS for ZGNR (N=10) Electrodes for a bias of 0V (a) and 0.6V(b)

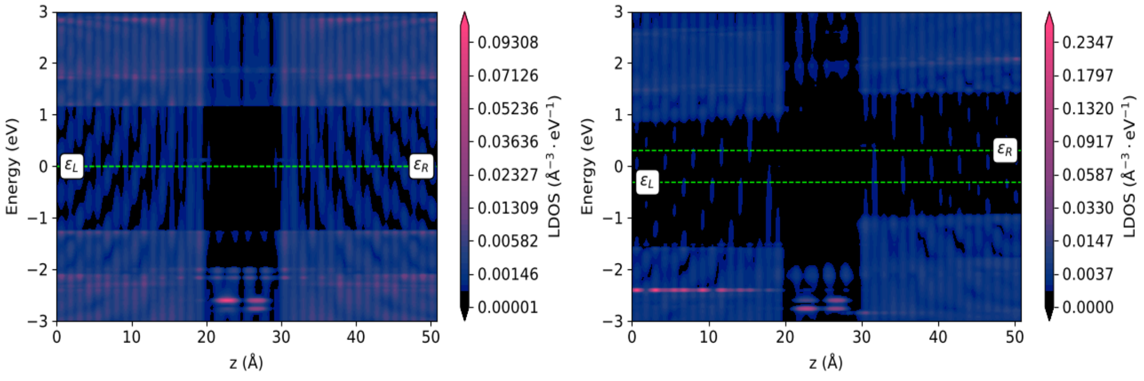

(a) (b)

Figure 7.28: DOS for GNS Electrodes for a bias of 0V (a) and 0.6V (b)

3 Metal vs Graphene Electrodes

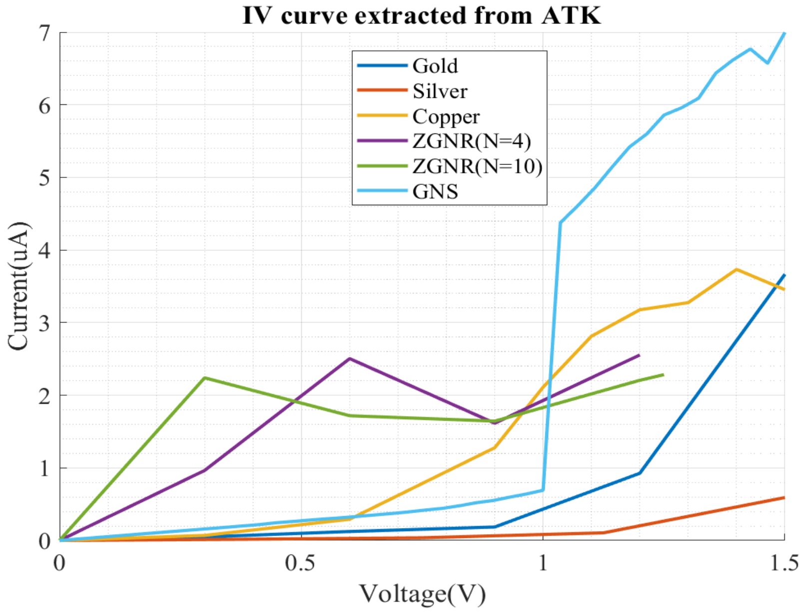

Figure 7.29: IV Curve for all types of electrodes for OPE3 channel

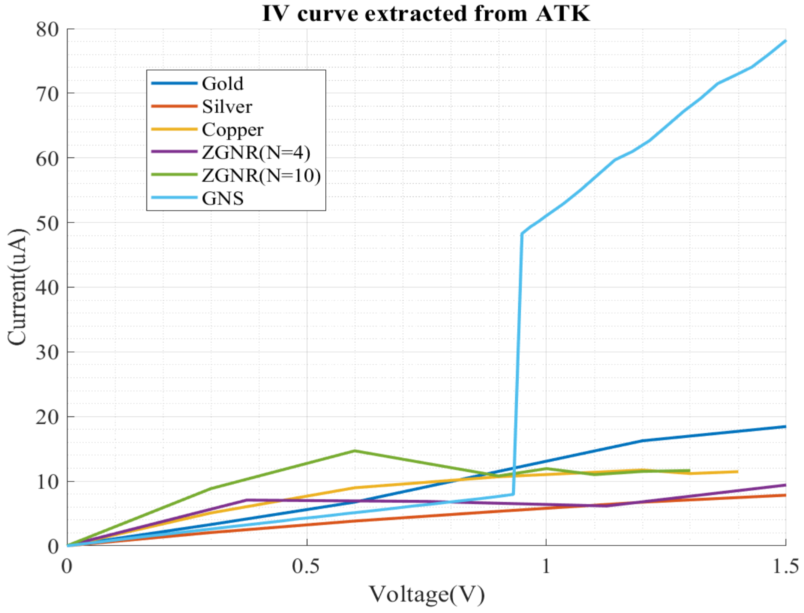

Figure 7.30: IV Curve for all types of electrodes for 2TT channel

From the IV curves (figure 7.29,7.30) we can see that for graphene based electrodes we have higher ON current than the metal based electrodes. This is due to added benefit the electrons get from having a molecular wire made completely of carbon atoms. Electrons need face many obstacles when hopping from one type of material to another. But, when we have a graphene electrode we have a partially homogeneous (in terms of atoms) molecular wire with electrode and channel made of organic molecule (i.e. mainly carbon atoms). This gives the benefit to electrons to move from the left electrode to the right thus producing better current flow. This also evident from the above two graphs where it can been seen that for OPE3 based wire the graphene based electrodes have visibly very distinct high current. But for 2TT although greater they are not well separated as in the case of OPE3. OPE3 based wire is compeletly carbon based whereas 2TT has sulphur atoms in it. And an overall lower low current in OPE3 compared to 2TT might due to the larger length of the OPE3.

Chapter 8

Conclusions

Molecular electronics has gone from a theoretical studies to experimental studies within the past two decades. And with the limitations of CMOS technology arriving soon molecular devices are needed now more than ever. The central molecule and electrode materials play an crucial role in controlling the behaviour of molecular devices.

The research work done in this thesis was focused on using graphene (which has shown tremendous application) as an electrode for a molecular wire and comparing its conduction properties with the traditional metal based electrodes. Through this work the reader is introduced to the first principles used for atomic level simulation of molecular devices. Some basic theory on graphene and its fabrication is also provided.

Finally, the goal of the thesis was realized. Firstly, a study of conduction properties for metal based electrodes was performed. The metal and graphene based electrodes showed difference in the current values with the former showing low values than the later. This can be attributed to natural conjugation path is created between the carbon based electrodes and the carbon based channel.

The case of graphene was studied using its zigzag nanoribbon form with two different widths(N=4 and 10) and then the peculiar case of graphene nanosheets was simulated. ZGNRs showed a negative differential resistance which can be helpful in developing crucial electronic components. Graphene nanosheets showed a sudden increase in the current values for both the OPE3 and 2TT case.

Further work is needed to conclude if this behaviour is unique to molecular wires based on graphene nanosheet electrodes. This rather unexpected behaviour has been an interesting outcome of this thesis.

In summary, the main outline of this thesis work is that the electrode fingerprint is always present in transport through molecular juntions. In particular, in the case of metal electrodes, the specific considered molecule is strongly determining the transport features at low bias, because in that bias range the conducting states are attributable mainly to the specific molecule used as channel. Instead, at higher bias, the transport seems dominated by electrode states.

In the graphene electrode case, instead it seems that the molecule has always a minor role in conduction. Indeed, in all cases (ZGNR 4, ZGNR 10, GNS) all the transmission states are attributable mainly to electrode states, either at low bias or at high bias.

The reason of that should be probably found in the different type of wavefunction conjugation in the case of metal or graphene contacts. With metal contacts there is less orbital conjugation due to d-type vs p-type orbital mismatch in the contact and in the molecule (only organic molecules are considered in this work). Instead, with graphene electrodes there is always a good orbital conjugation between contacts and molecule, likely due to dominant p-type orbitals in graphene and in the molecule. Additional analysis concerning also transmission states may be performed in future works to confirm these results.

Chapter 9

Bibliography

[1] Tsutsui, M.; Taniguchi, M. Sensors 2012, 12, 7259-7298.

[2] Moore, G. E. Electronics 1965, 38, 114−117.

[3] https://www.tsmc.com/english/dedicatedFoundry/technology/logic/l_3nm

[4]Song, H.; Reed, M. A.; Lee, T. Adv. Mater. 2011, 23, 1583-1608.

[5] Metzger, R. M. J. Mater. Chem 2008, 18, 4364-4396.

[6] Mann, B. Kuhn, H. J. Appl. Phys. 1971, 42, 4398–4406.

[7] Aviram, A.; Ratner, M. A. Chem. Phys. Lett. 1974, 29, 277−283.

[8] Metzger, R. M. Nanoscale 2018, 10, 10316-10332.

[9] Joachim, C.; Gimzewski, J. K.; Aviram, A. Nature 2000, 408, 541.

[10] Reed, M. A. Science 1997, 278, 252−254.

[11] Xu, B.; Tao, N. J. Science 2003, 301, 1221−1223.

[12] Cui, X. D.; Primak, A.; Zarate, X.; Tomfohr, J.; Sankey, O. F.; Moore, A. L.; Moore, T. A.; Gust, D.; Harris, G.; Lindsay, S. M. Science 2001, 294, 571-574.

[13] Haiss, W.; van Zalinge, H.; Higgins, S. J.; Bethell, D.; Ho¨benreich, H.; Schiffrin, D. J.; Nichols, R. J. J. Am. Chem. Soc. 2003, 125, 15294−15295.

[14] Ratner, M. Nat. Nanotechnol 2013, 8, 378-381.

[15] https://www.tomshardware.com/news/tsmcs-wafer-prices-revealed-300mm-wafer-at-5nm-is-nearly-dollar17000

[16] Helmut Eschring. The Fundamentals of Density Functional Theory. 1996. Springer.

[17] Hohenberg, P. and Kohn W. Inhomogeneous electron gas. Physical review, 136(3B): p. B864–B871.

[18] Kohn, W. and Sham, L. J. Self-consistent equations including exchange and correlation effects. Physical Review, 1965. 140(4A): p. A1133–A1138.

[19] Born, M. and Oppenheimer, R. On the quantum theory of molecules. Annalen der Physik, 1927. 84(20): p. 1–32.

[20] Parr, R.G. and Y. Weitao, Density-functional theory of atoms and molecules. Oxford University Press, USA. Vol. 16. 1994.

[21] Gross, E. K. and R. M. Dreizler, Density functional theory. Springer, 1995.

[22] Levy, M. Electron densities in search of Hamiltonians. Physical Review A, 1982. 26(3): p. 1200–1208.

[23] Lieb, E. H. Thomas-Fermi and related theories of atoms and molecules. Reviews of Modern Physics, 1981. 53(4): p. 603–641.

[24] Axel, D. Becke. Density-functional exchange-energy approximation with correct asymptotic behavior. Physical Review A, 1988. 38(6): p. 3098–3100.

[25] David, C. L. and Perdew, J. P. The exchange-correlation energy of a metallic surface. Solid State Communications, 1975. 17(11): p. 1425–1429.

[26] Hammer, B.; Hansen, L. B.; Nørskov, J. K. Improved dsorption energetics within density-functional theory using revised perdew-burke-ernzerhof functionals. Physical Review B, 1999. 59(11): p. 7413–7421.

[27] Richard M. Martin. Electronic structure: basic theory and practical methods. Cambridge university press, 2004.

[28] Ceperley, D. M. and Alder, B. Ground state of the electron gas by a stochastic method. Physical Review Letters, 1980. 45(7): p. 566–569.

[29] Perdew, J. P. and Zunger, A. Self-interaction correction to density-functional approximations for many-electron systems. Physical Review B, 1981. 23(10): p. 5048–5079.

[30] R. Q. Hood, M. Y. Chou, A. J. Williamson, G. Rajagopal and R. J. Needs. Quantum Monte Carlo investigation of exchange and correlation in silicon. Phys. Rev. Lett. 1997. 78(17): p. 3350–3353.

[31] R. Q. Hood, M. Y. Chou, A. J. Williamson, G. Rajagopal and R. J. Needs. Exchange and correlation in silicon. Physical Review B, 1998. 57(15): p. 8972–8982.

[32] Car, R. Quantitative Structure[U+2010]Activity Relationships. 2002. 21(2): p. 97–104.

[33] Fulde, P. Electron Correlations in Molecules and Solids. 1995. Springer.

[34] Hedin, L. and S. Lundqvist, Effects of electron-electron and electron-phonon interactions on the one-electron states of solids. Solid State Physics, 1970. 23: p. 1–181.

[35] Vosko, S. H.; L. Wilk, and M. Nusair, Accurate spin-dependent electron liquid correlation energies for local spin density calculations: a critical analysis. Canadian Journal of Physics, 1980. 58(8): p. 1200–1211.

[36] Perdew, J. P., K. Burke, and M. Ernzerhof, Generalized gradient approximation made simple. Physical Review Letters, 1996. 77(18): p. 3865–3868.

[37] Perdew, J. P.; Ruzsinszky, A; Tao, J; Staroverov, V. N.; Scuseria, G. E.; Csonka, G. I. Prescription for the design and selection of density functional approximations: More constraint satisfaction with fewer fits. The Journal of Chemical Physics, 2005. 123(6): p. 062201–062209.

[38] W. Y. Kim, Y. C. Choi, S. K. Min, Y. Cho, and K. S. Kim. Application of Quantum Chemistry to Nanotechnology: Electron and Spin Transport in Molecular Devices. Chem. Soc. Rev., 38:2319–2333, 2009.

[39] M. D. Ventra. Electrical Transport in Nanoscale Systems. Cambridge University Press, 2008.

[40] M. Büttiker, Y. Imry, R.Landauer, and S.Pinhas. Generalized Many-Channel Conductance FormulaWith Application to Small Rings. Phys. Rev. B, 31:6207–6215, 1985.

[41] S. Datta. Electronic Transport in Mesoscopic Systems. Cambridge University Press, 1995.

[42] H. Haug and A.P. Jauho. Quantum Kinetics in Transport and Optics of Semiconductors. Springer-Verlag Berlin, 1996.

[43] A. Champagne, A. N. Pasupathy, and D. C. Ralph, to be published (2004).

[44] Metzger, R. M. Chem. Rev. 2015, 115, 5056-5115.

[45] Ruoff, R. S.; Kadish, K. M.; Boulas, P.; Chen, E. C. M. J. Phys. Chem. 1995, 99, 8843−8850.

[46] Jia, C.; Guo, X. Chem. Soc. Rev. 2013, 42, 5642-60. 23. Silvia, K. J. Phys. Condens. Matter 2011, 23, 013001.

[47] K. S. Novoselov, A. K. Geim, S. V. Morozov, D. Jiang, Y. Zhang, S. V. Dubonos, I. V. Grigorieva, and A. A. Firsov. Electric Field Effect in Atomically Thin Carbon Films. Science 306, 666–669 (2004).

[48] J. Moser, A. Barreiro, and A. Bachtold. Current-induced cleaning of graphene. Applied Physics Letters 91, 163513 (2007).

[49] A. A. Balandin, S. Ghosh, W. Bao, I. Calizo, D. Teweldebrhan, F. Miao, and C. N. Lau. Superior Thermal Conductivity of Single-Layer Graphene. Nano Letters 8, 902–907 (2008).

[50] F. Schwierz. Graphene transistors. Nature Nanotechnology 5, 487–496 (2010).

[51] R. R. Nair, P. Blake, A. N. Grigorenko, K. S. Novoselov, T. J. Booth, T. Stauber, N. M. R. Peres, and A. K. Geim. Fine Structure Constant Defines Visual Transparency of Graphene. Science 320, 1308 (2008).

[52] C. Lee, X. Wei, J. W. Kysar, and J. Hone. Measurement of the Elastic Properties and Intrinsic Strength of Monolayer Graphene. Science 321, 385 (2008).

[53] K. S. Novoselov, V. I. Fal'ko, L. Colombo, P. R. Gellert, M. G. Schwab, and K. Kim. A roadmap for graphene. Nature 490, 192–200 (2012).

[54] L. Yang, C.-H. Park, Y.-W. Son, M. L. Cohen, and S. G. Louie. Quasiparticle Energies and Band Gaps in Graphene Nanoribbons. Physical Review Letters 99, 186801 (2007).

[55] M. I. Katsnelson. Graphene: Carbon in Two Dimensions. Cambridge: Cambridge University Press, 2012.

[56] R. Saito, G. Dresselhaus, and M. S. Dresselhaus. Physical Properties of Carbon Nanotubes. Imperial College Press, 1998.

[57] A. H. Castro Neto, F. Guinea, N. M. R. Peres, K. S. Novoselov, and A. K. Geim. The electronic properties of graphene. Reviews of Modern Physics 81, 109–162 (2009).

[58] P. R. Wallace. The Band Theory of Graphite. Physical Review 71, 622–634 (1947).

[59] S. Reich, C. Thomsen, and J. Maultzsch. Carbon Nanotubes: Basic Concepts and Physical Properties. Wiley-VCH Verlag GmbH Co. KGaA, 2007.

[60] K. Nakada, M. Fujita, G. Dresselhaus, and M. S. Dresselhaus. Edge state in graphene ribbons: Nanometer size effect and edge shape dependence. Physical Review B 54, 17954–17961 (1996). 169

[61] K. Wakabayashi, K.-i. Sasaki, T. Nakanishi, and T. Enoki. Electronic states of graphene nanoribbons and analytical solutions. Science and Technology of Advanced Materials 11, 054504 (2010).

[62] M. Fujita, K. Wakabayashi, K. Nakada, and K. Kusakabe. Peculiar Localized State at Zigzag Graphite Edge. Journal of the Physical Society of Japan 65, 1920–1923 (1996).

[63] Geim, Andre K., and Philip Kim. "Carbon wonderland." Scientific American 298.4 (2008): 90-97.

[64] Norimatsu, Wataru, and Michiko Kusunoki. "Epitaxial graphene on SiC 0001: advances and perspectives." Physical Chemistry Chemical Physics 16.8 (2014): 3501-3511

[65] http://www.iue.tuwien.ac.at/phd/ayalew/node20.html [Online].

[66] Arnoult, William J., and Rex B. McLellan. "The solubility of carbon in rhodium ruthenium, iridium and rhenium." Scripta Metallurgica 6.10 (1972): 1013-1018.

[67] Zhang, Yi, Luyao Zhang, and Chongwu Zhou. "Review of chemical vapor deposition of graphene and related applications." Accounts of chemical research 46.10 (2013): 2329-2339.

[68] http://www.graphenea.com/pages/cvd-graphene [Online].

[69] Wang X, Dai H. 2010. Etching and narrowing of graphene from the edges. Nature Chem. 2(8):661-665.

[70] Abramova V, Slesarev AS, Tour JM. 2013. Meniscus-Mask Lithography for Narrow Graphene Nanoribbons. ACS Nano. 7(8):6894-6898.

[71] Genorio B, Lu W, Dimiev AM, Zhu Y, Raji AO, Novosel B, Alemany LB, Tour JM. 2012. In Situ Intercalation Replacement and Selective Functionalization of Graphene Nanoribbon Stacks. ACS Nano. 6(5):4231-4240.

[72] Kosynkin DV, Lu W, Sinitskii A, Pera G, Sun Z, Tour JM. 2011. Highly Conductive Graphene Nanoribbons by Longitudinal Splitting of Carbon Nanotubes Using Potassium Vapor. ACS Nano. 5(2):968-974.

[73] M. Y. Han, J. C. Brant, and P. Kim. Electron Transport in Disordered Graphene Nanoribbons. Physical Review Letters 104, 056801 (2010).

[74] L. Grill, M. Dyer, L. Lafferentz, M. Persson, M. V. Peters, and S. Hecht. Nanoarchitectures by covalent assembly of molecular building blocks. Nature Nanotechnology 2, 687–691 (2007).

[75] J. Cai, P. Ruffieux, R. Jaafar, M. Bieri, T. Braun, S. Blankenburg, M. Muoth, A. P. Seitsonen, M. Saleh, X. Feng, K. Müllen, and R. Fasel. Atomically precise bottom-up fabrication of graphene nanoribbons. Nature 466, 470–473 (2010).

[76] P. B. Bennett, Z. Pedramrazi, A. Madani, Y.-C. Chen, D. G. de Oteyza, C. Chen, F. R. Fischer, M. F. Crommie, and J. Bokor. Bottom-up graphene nanoribbon field-effect transistors. Applied Physics Letters 103, 253114 (2013).

[77] M. Kolmer, A. A. Ahmad Zebari, J. S. Prauzner-Bechcicki, W. Piskorz, F. Zasada, S. Godlewski, B. Such, Z. Sojka, and M. Szymonski. Polymerization of Polyanthrylene on a Titanium Dioxide (011)-(2 × 1) Surface. Angewandte Chemie International Edition 52, 10300–10303 (2013).

[78] R. M. Jacobberger, B. Kiraly, M. Fortin-Deschenes, P. L. Levesque, K. M.

McElhinny, G. J. Brady, R. Rojas Delgado, S. Singha Roy, A. Mannix, M. G. Lagally, P. G. Evans, P. Desjardins, R. Martel, M. C. Hersam, N. P. Guisinger, and M. S. Arnold. Direct oriented growth of armchair graphene nanoribbons on germanium. Nature Communications 6, 8006 (2015).

[79] A. Narita, X. Feng, Y. Hernandez, S. A. Jensen, M. Bonn, H. Yang, I. A. Verzhbitskiy, C. Casiraghi, M. R. Hansen, A. H. R. Koch, G. Fytas, O. Ivasenko, B. Li, K. S. Mali, T. Balandina, S. Mahesh, S. De Feyter, and K. Müllen. Synthesis of structurally well-defined and liquid-phase-processable graphene nanoribbons. Nature Chemistry 6, 126–132 (2014).

[80] Ferry Prins,Amelia Barreiro, Justus W. Ruitenberg, Johannes S. Seldenthuis,Nuria Aliaga-Alcalde, Lieven M. K. Vandersypen, and Herre S. J. van der Zant. Room-Temperature Gating of Molecular Junctions Using Few-Layer Graphene Nanogap Electrodes. Nano Lett. 2011, 11, 11, 4607–4611

[81] The Graphene Council. (2020, June 10). How to Perform Liquid-Phase Exfoliation on Graphene. AZoNano. Retrieved on November 30, 2021 https://www.azonano.com/article.aspx?ArticleID=5471.

[82] Yudong He, Huanli Dong, Tao Li1, Chengliang Wang, Wei Shao, Yajie Zhang, Lang Jiang and Wenping Hu1. Graphene and graphene oxide nanogap electrodes fabricated by atomic force microscopy nanolithography. Appl. Phys. Lett. 97, 133301 (2010)

[83] Søren Smidstrup et. al., QuantumATK: An integrated platform of electronic and atomic-scale modelling tools, 2020 J. Phys.: Condens. Matter 32 015901

[84] Das, B., Abe, S., ”Designing Cyclophane-Based Molecular Wire Sensors”. The Journal of Physical Chemistry B, 2006, 110(47), 23806-23811. doi:10.1021/jp064916p

[85] Jie Li, Yi Zhou, Leining Zhang and Hui Li, Characteristic electron transport on pyridine-linked molecular devices with graphene nanoribbons electrodes and gold electrodes, Phys.Chem.Chem.Phys., 2016, 18, 28217

Appendix A

Cyclophane (pCp) based Molecular Sensor

1 -S Anchor

The gas sensor that was simulated is based on paracyclophane (pCp) based molecule placed in between two gold electrodes. The anchor group used here is thiol gold bonds (-S-Au). There is a change in conductance when chromium atom is placed in between the molecule. This changes the IV curve thus helping in detection of the metal ion.

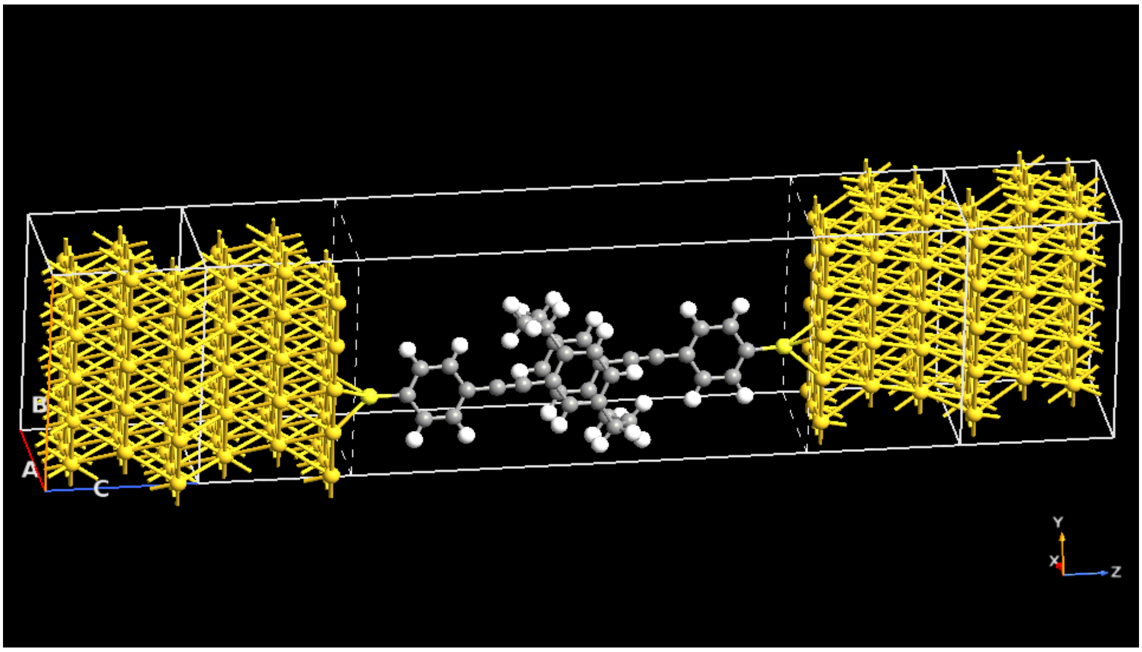

Figure A.1: Initial geometry for PcP based Chromium(Cr) sensor with -S as anchor atom

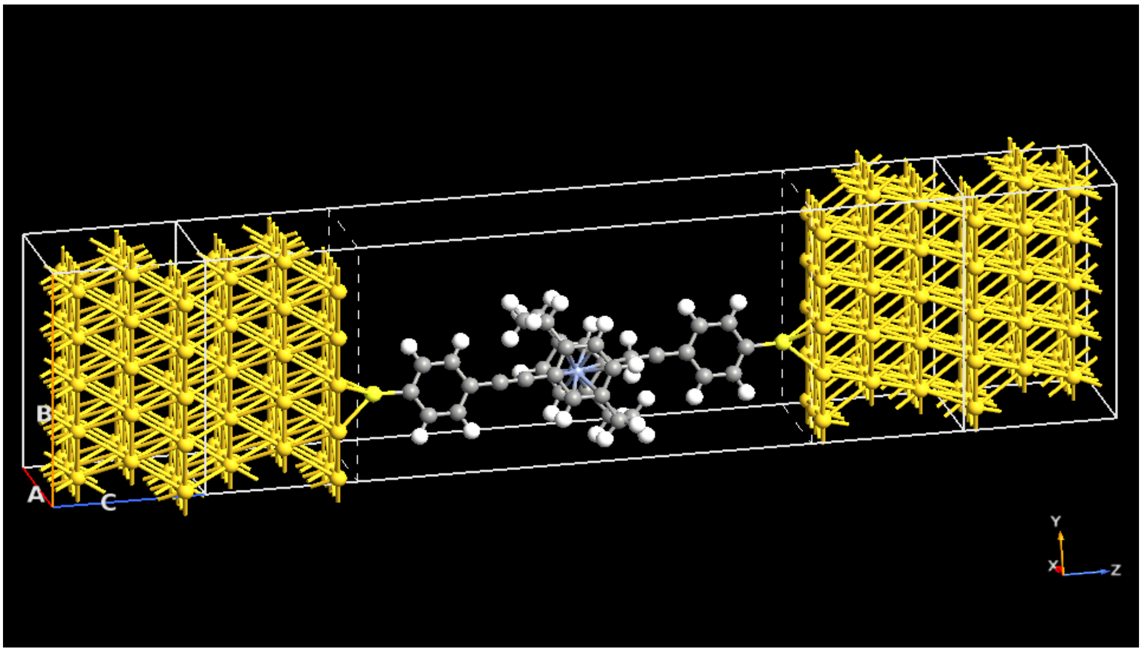

Figure A.2: Final geometry for PcP based Chromium(Cr) sensor with -S as anchor atom

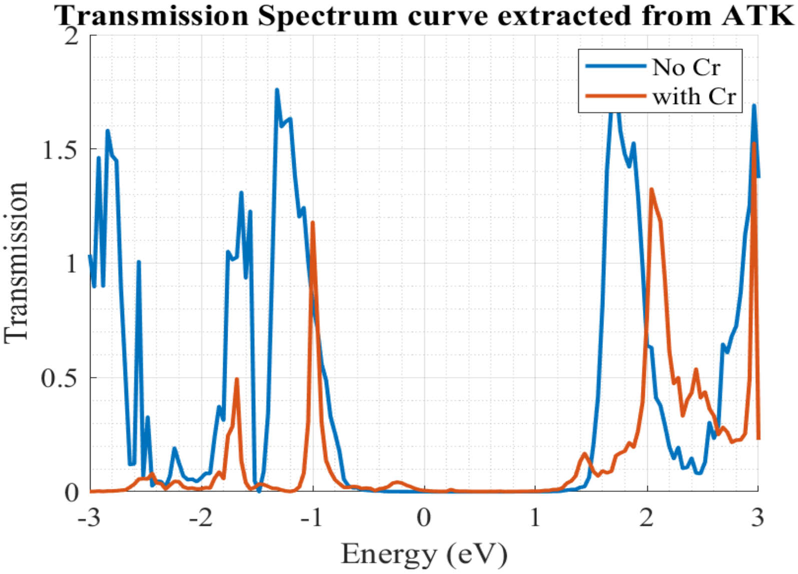

Figure A.3: Tranmission Spectrum of the device with and without chromium

From the transmission spectrum we can notice a change in HOMO-LUMO Gap (HLG). The peaks are present in both cases only the energy at which they occur is different for the two cases. Next, the IV curve is shown below,

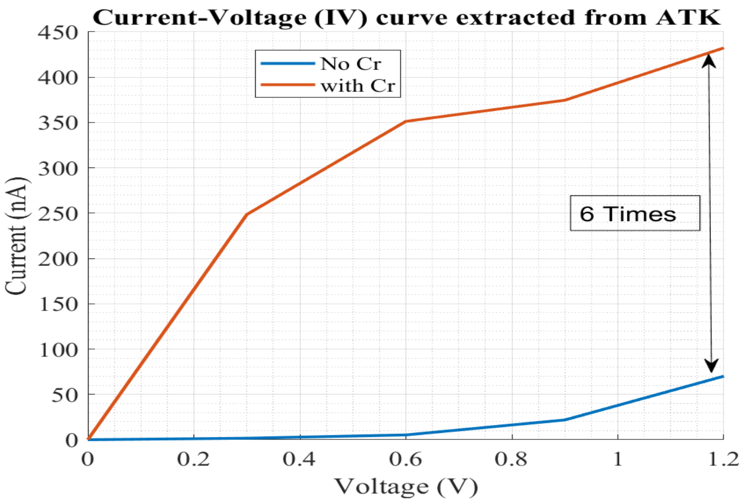

Figure A.4: IV Characteristics of the device with and without chromium

It is clear from the plot an enhancement of current is achieved by introducing a Cr ion. We can say by the introduction of Cr ion we have a more stable central molecule which results in high current when compared to No Cr case.

2 -SCH2 Anchor

As a next exercise, the anchoring group was changed to $(-CH_2 - S - Au)$. The geometry of the deivce is shown in the next plots.

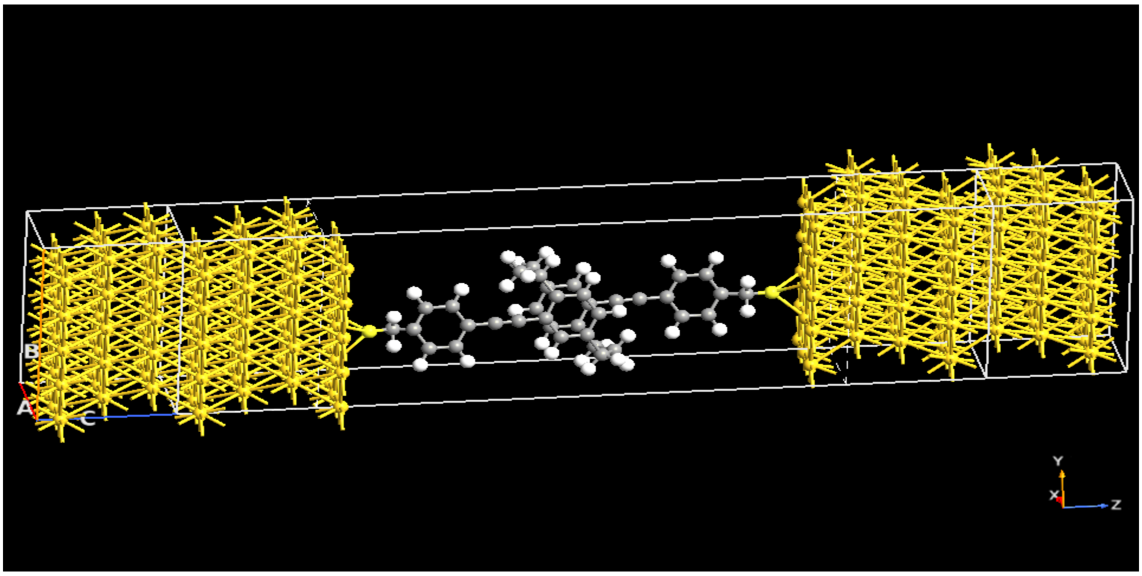

Figure A.5: Initial geometry for PcP based Chromium(Cr) sensor with $-SCH_2$ as anchor atom

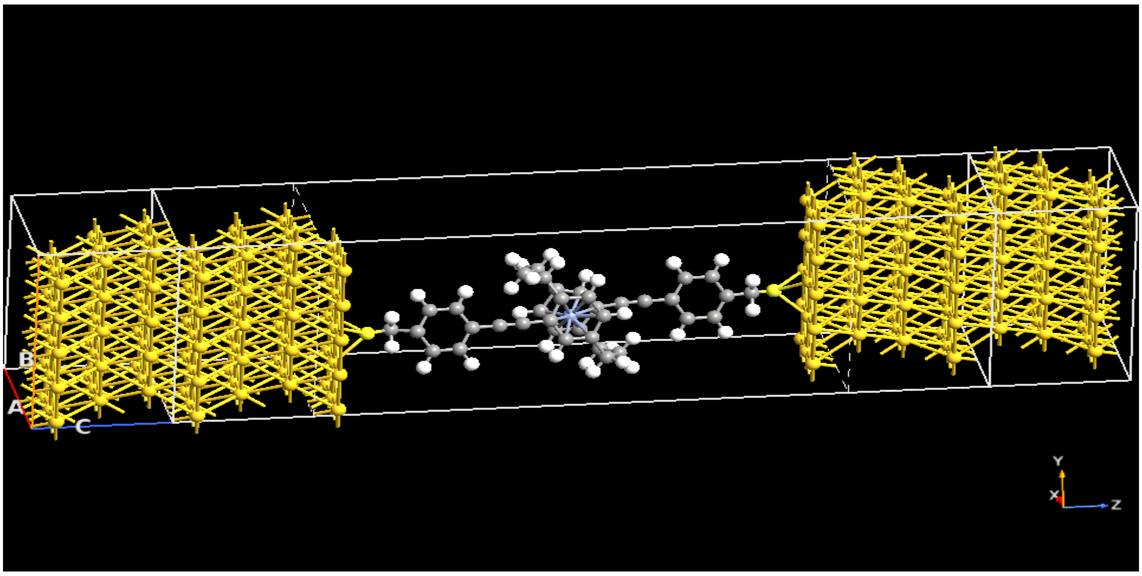

Figure A.6: Final geometry for PcP based Chromium(Cr) sensor with $-SCH_2$ as anchor atom

The transmission spectrum was then plotted for both the geometries,

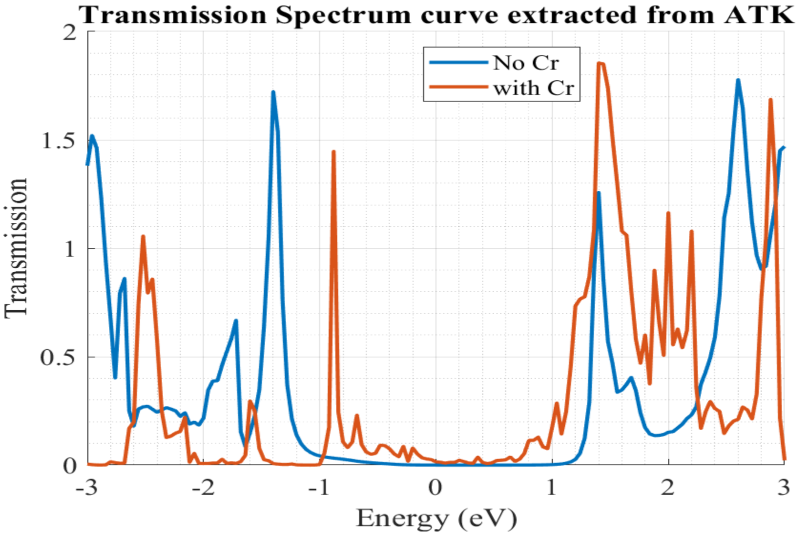

Figure A.7: Transmission Spectrum of the device with and without chromium

Just as we have seen in the previous case there is a change in HLG. But, the difference here is higher separation for the TS peaks in the negative energy region which leads to a very low HLG gap.

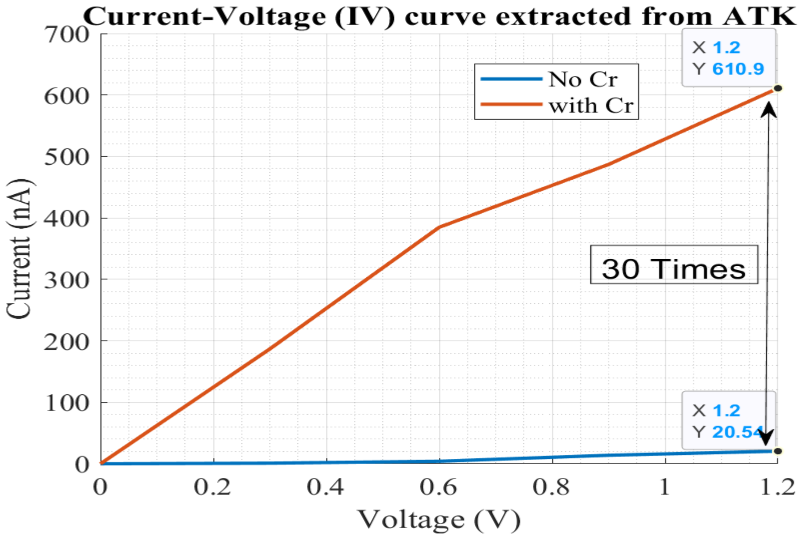

Figure A.8: IV Characteristics of the device with and without chromium

As we would expect very large current amplification is seen here. We can say that adding a $-CH_2$ group plays a negative role in conduction when No Cr ion is present and with the addition of Cr ion the conduction properties are improved as we saw in last case but $-CH_2$ group plays a positive role in increasing the conduction properties of the system. Since this was just an exercise no further work was done to further investigate this new structure which made Cr ion detection much better.

Appendix B

Electron Transport of Pyridine Linked Molecular Wire

The geometries reported here are all taken from the reference paper mentioned in the main text. Matching results were obtained for all cases expect for the graphene nanosheet case as it was mentioned in the main text. Five types of electrodes were used which are shown in following plots along with all the images of relevant quantities.

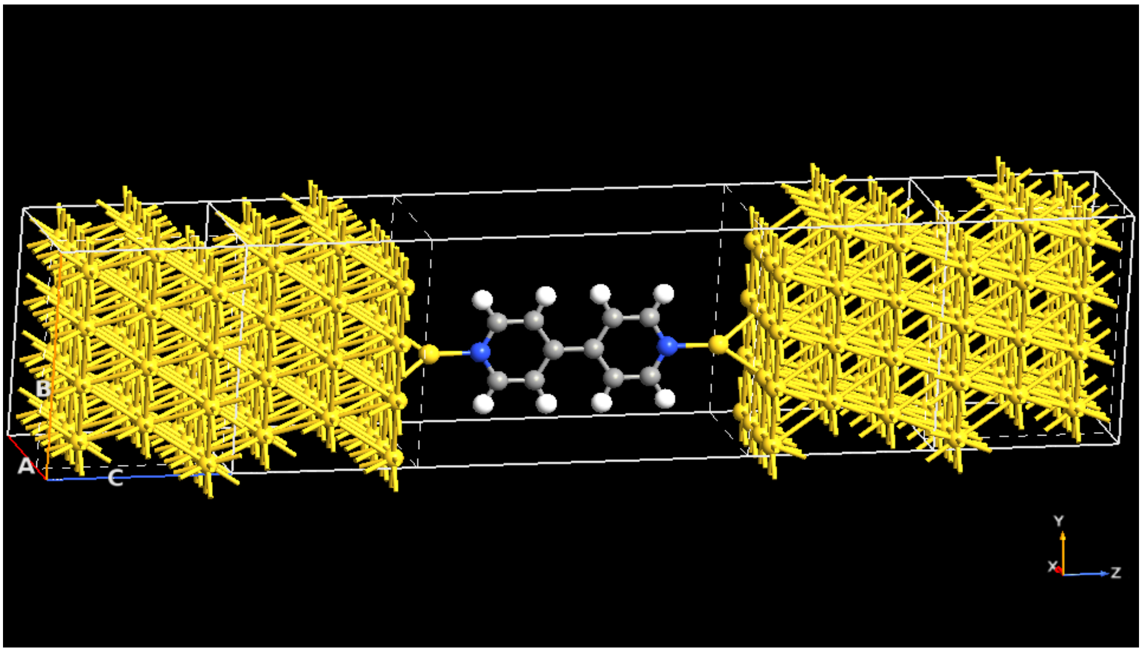

Figure B.1: Configuration for Gold Electrodes taken from QuantumATK

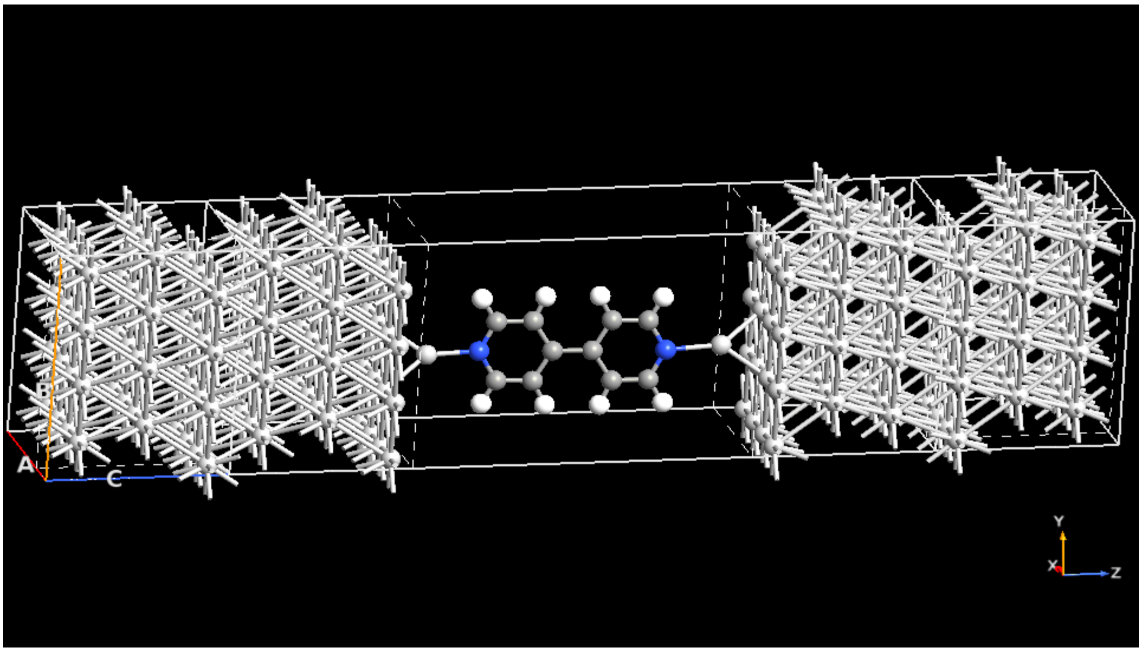

Figure B.2: Configuration for Silver Electrodes taken from QuantumATK

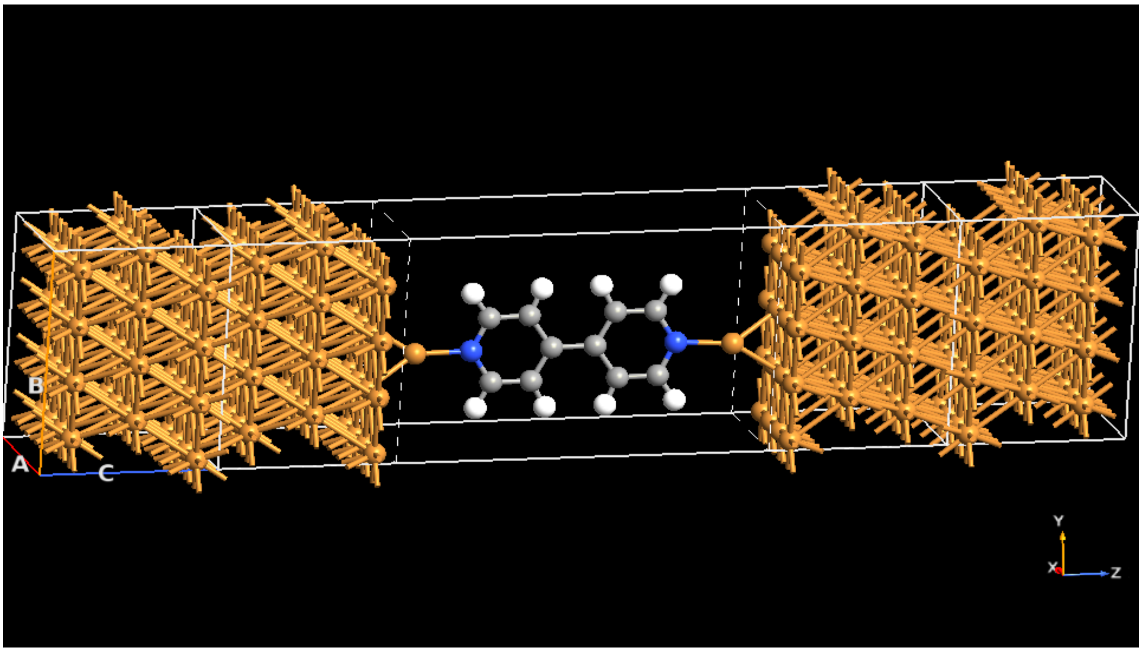

Figure B.3: Configuration for Copper Electrodes taken from QuantumATK

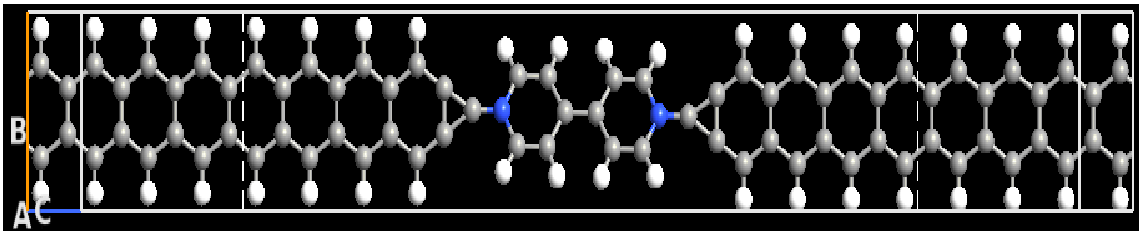

Figure B.4: Configuration for ZGNR Electrodes taken from QuantumATK

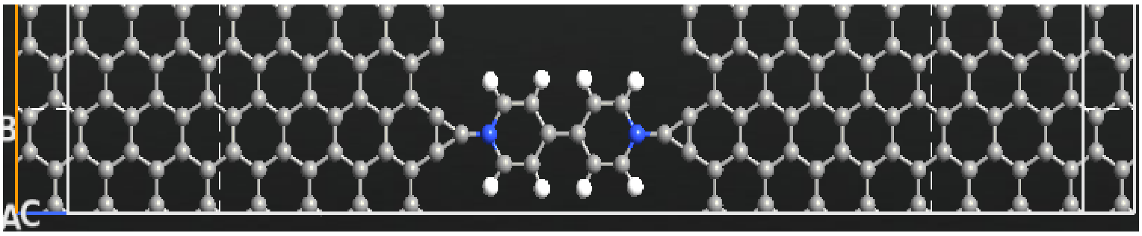

Figure B.5: Configuration for GNS Electrodes taken from QuantumATK

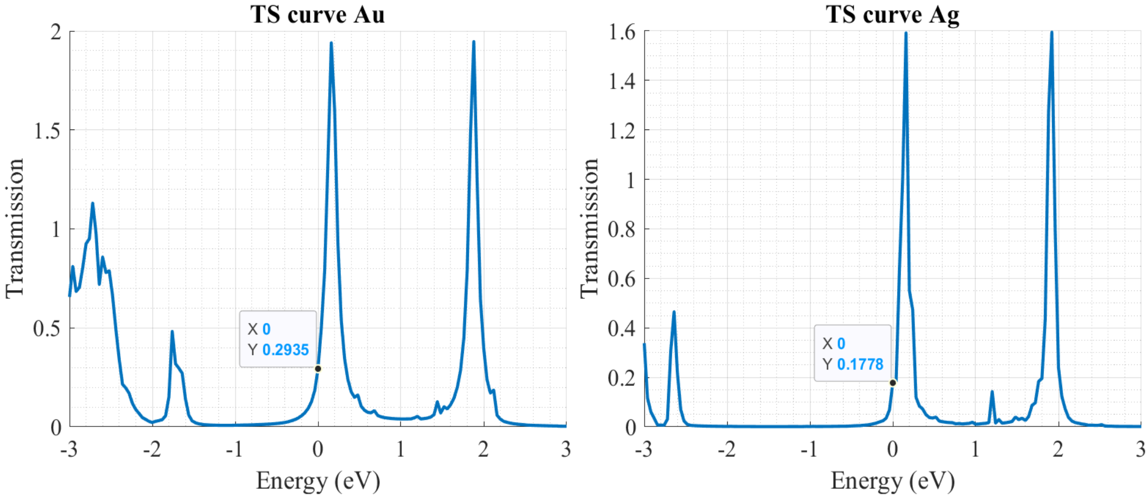

(a)

(b)

Figure B.6: Transmission Spectrum for Gold(a) and Silver(b)

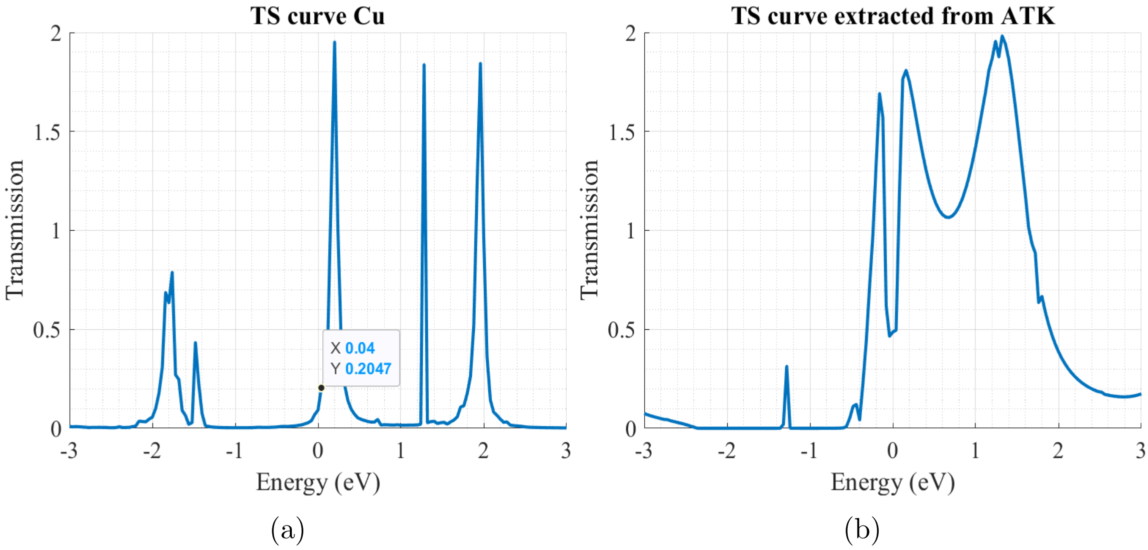

Figure B.7: Transmission Spectrum for Copper(a) and ZGNR(b)

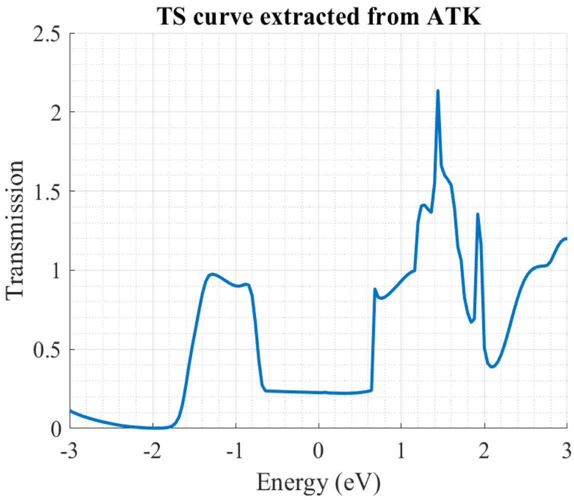

Figure B.8: Transmission Spectrum for GNS

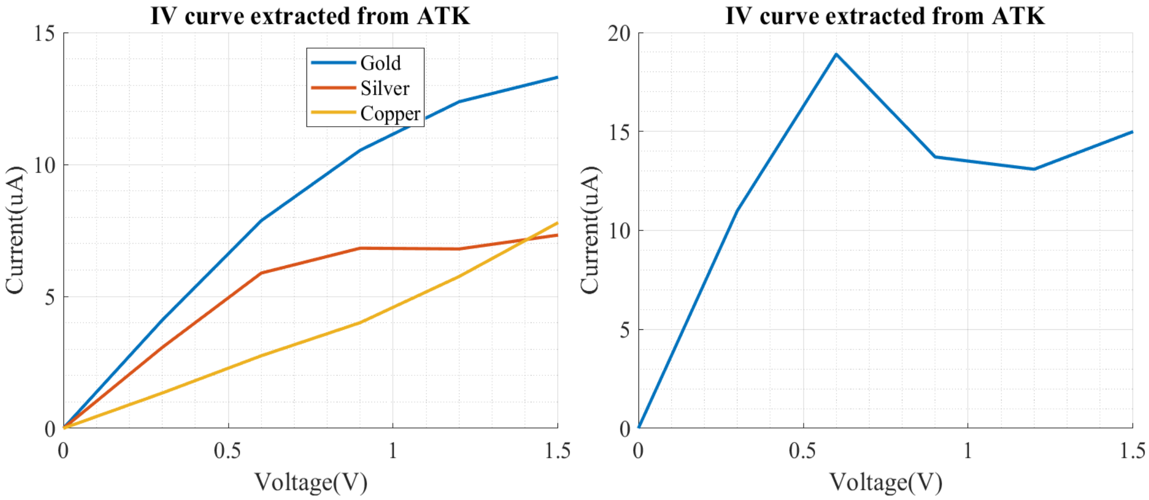

(a) Metal Electrodes (b) Zigzag Graphene Nanoribbon (ZGNR)

Figure B.9: IV Characteristics

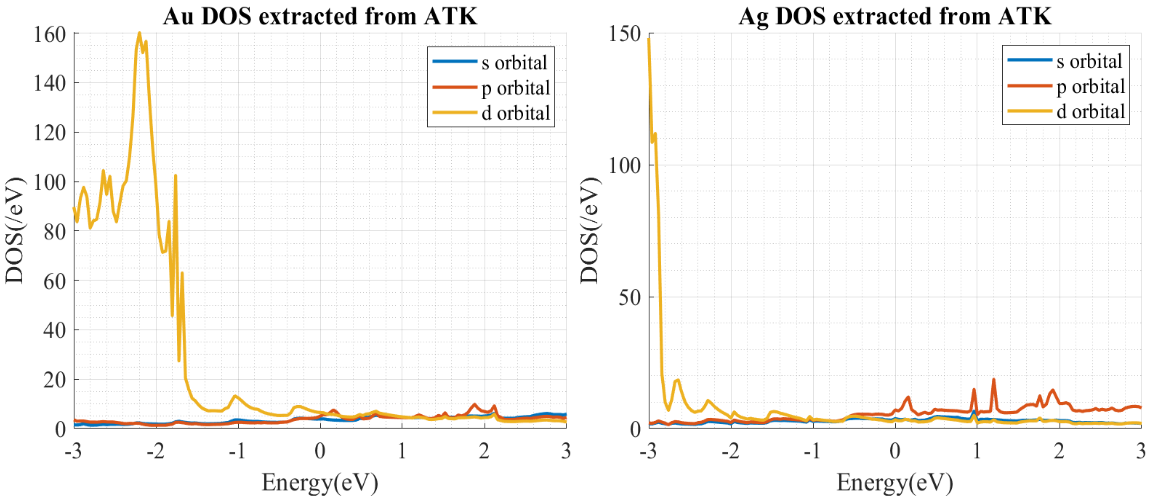

(a) (b)

Figure B.10: DDOS with Orbital Contribution for for Gold(a) and Silver(b)

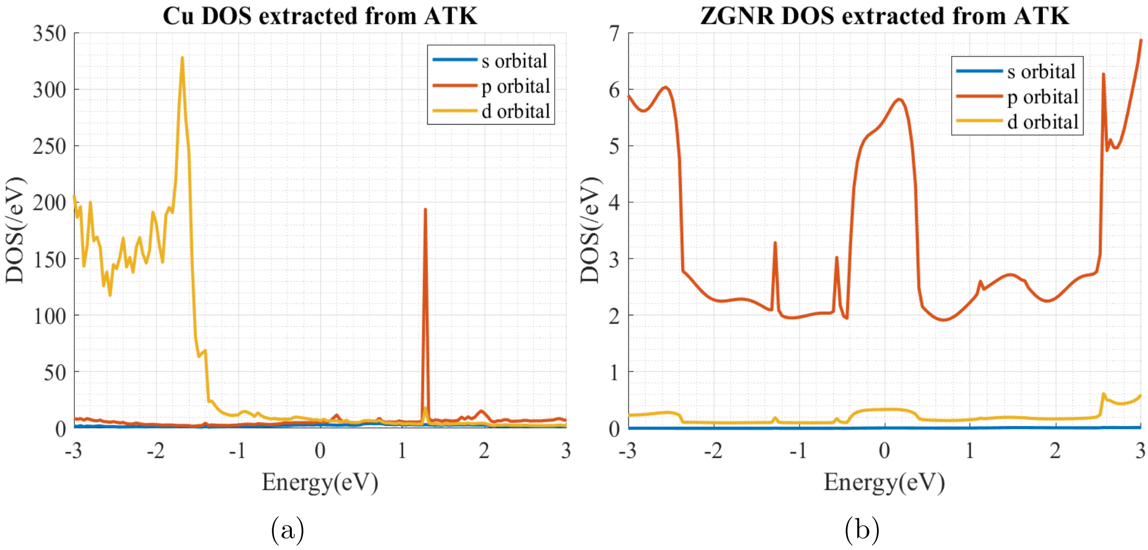

(a) (b)

Figure B.11: DDOS with Orbital Contribution for for Copper(a) and ZGNR(b)

Appendix C

Additional Images

1 Metal-based Electrodes

1.1 OPE3

Transmission Spectrum:

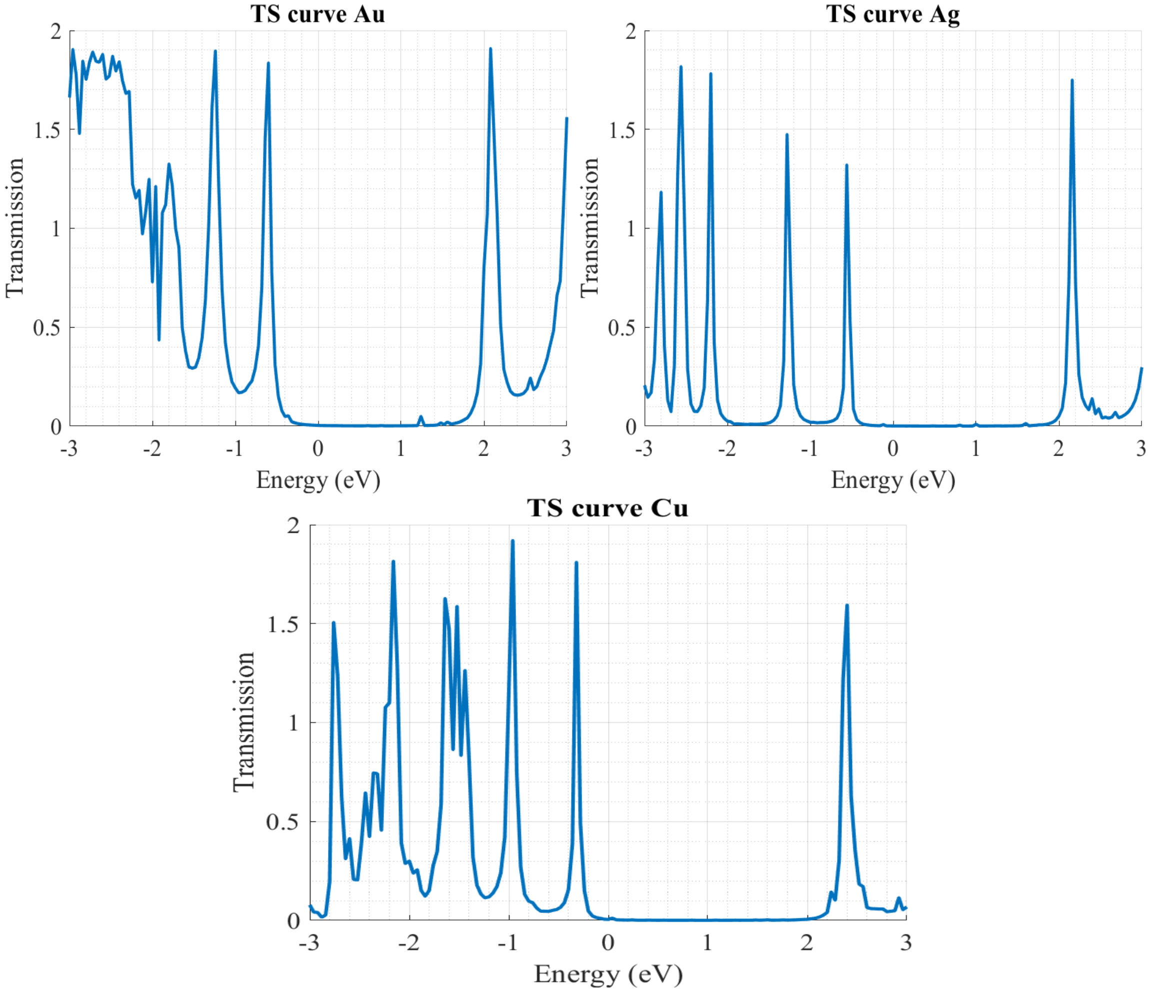

Figure C.1: Transmission Spectrum for individual metal electrodes gold(a), silver(b), copper(c)

Orbitals

At 0.6V

Gold Electrodes

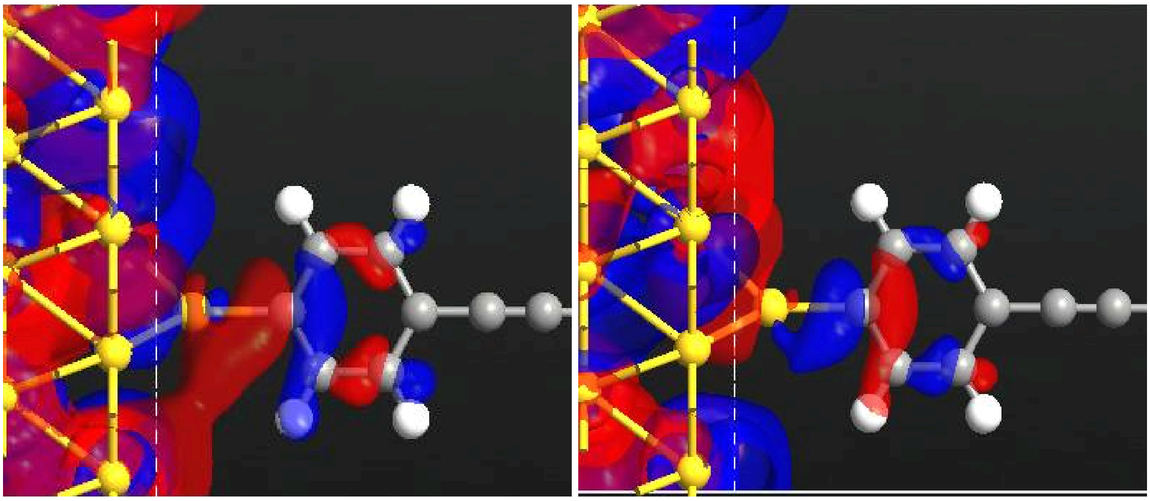

(a) HOMO Level

(b) HOMO+1 Level

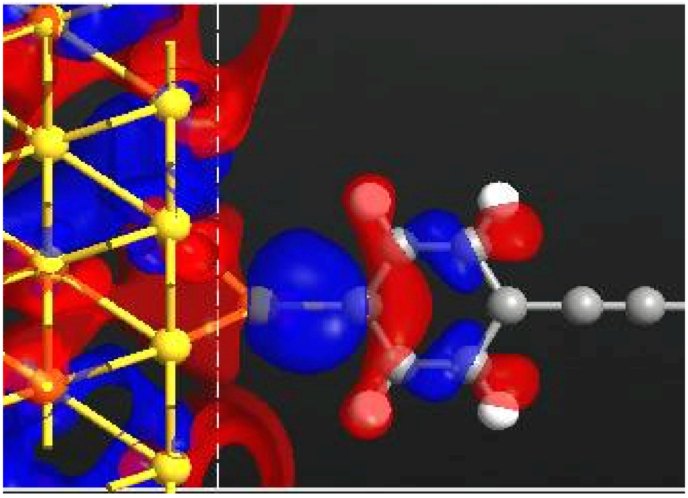

(c) HOMO+2 Level

Figure C.2: Eigen States at the left contact for Gold Electrode

Silver Electrodes

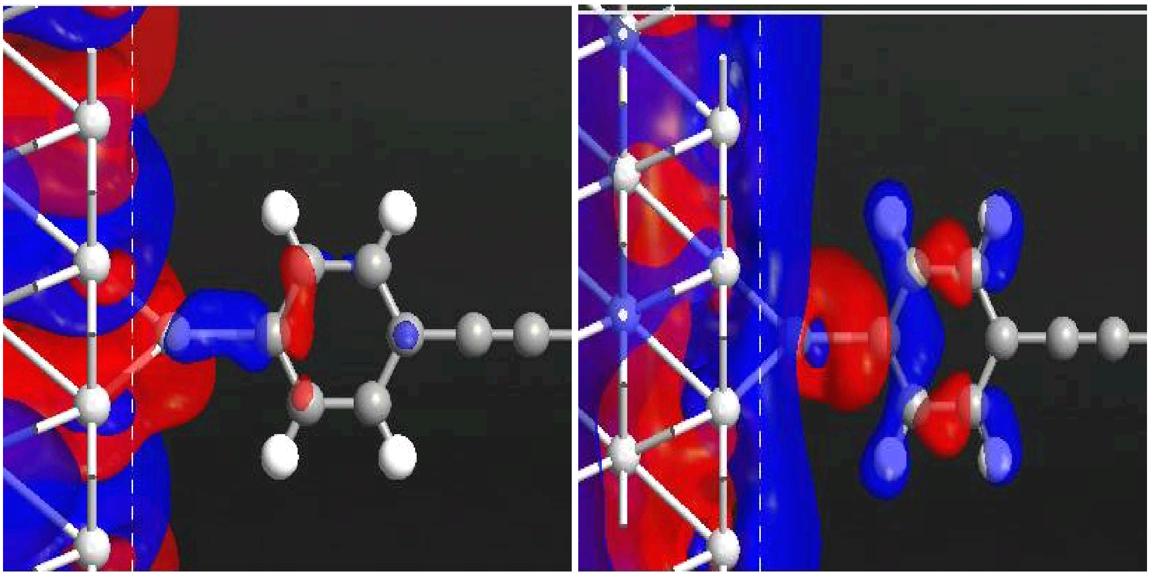

(a) HOMO Level (b) HOMO+1 Level

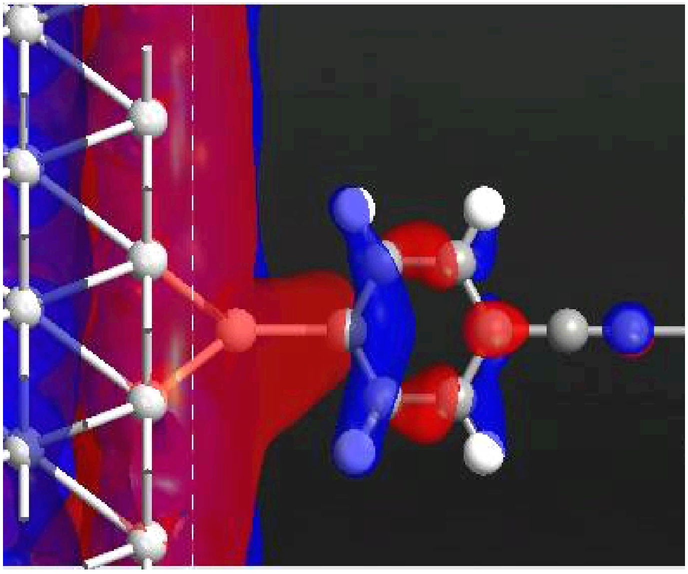

(c) HOMO+2 Level

Figure C.3: Eigen States at the left contact for Silver Electrode

Copper Electrodes

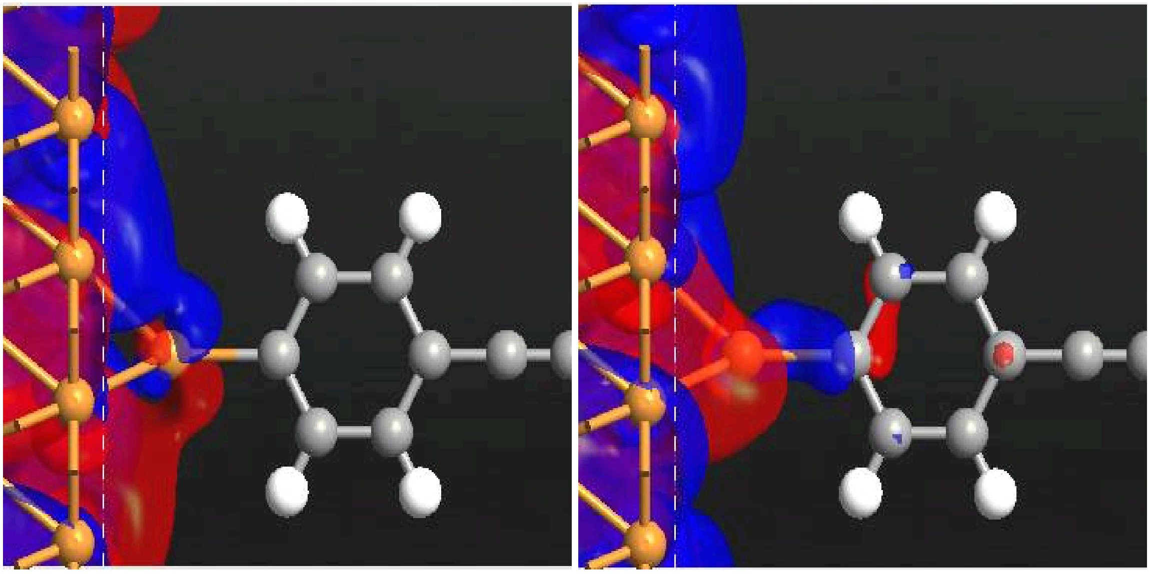

(a) HOMO Level (b) HOMO+1 Level

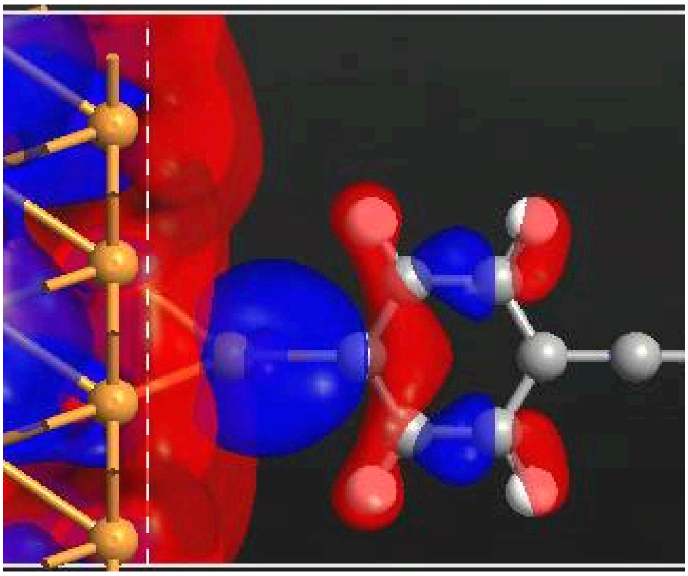

(c) HOMO+2 Level

Figure C.4: Eigen States at the left contact for Copper Electrode

At 1.2V

Gold Electrode

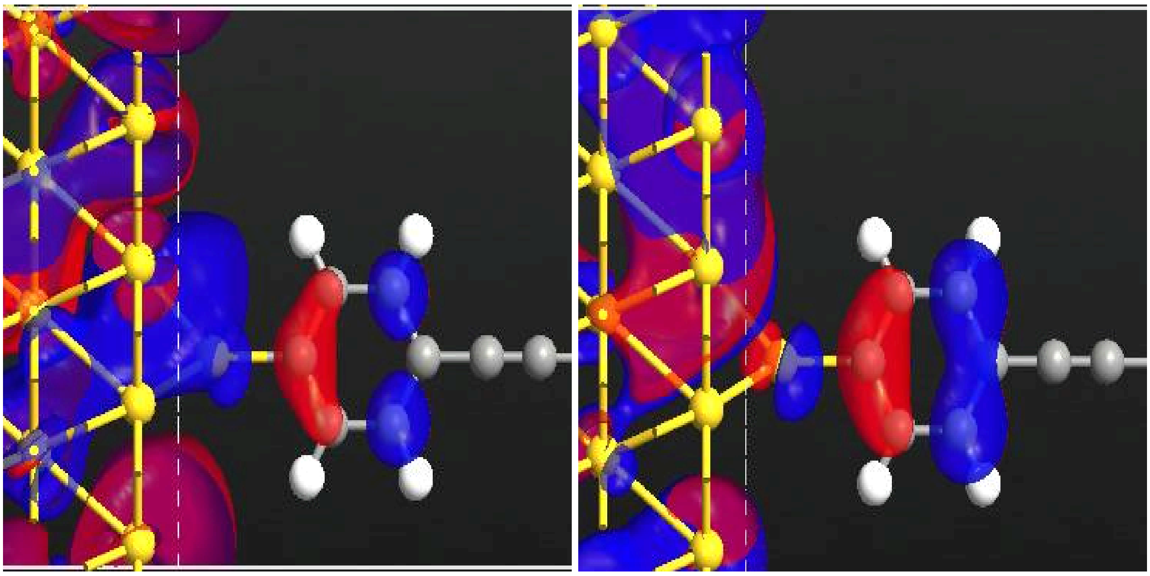

(a) HOMO Level

(b) HOMO+1 Level

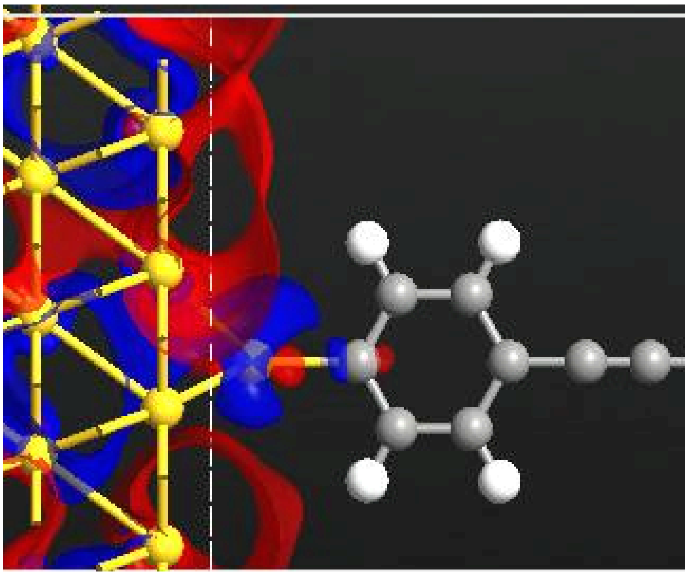

(c) HOMO+2 Level

Figure C.5: Eigen States at the left contact for Gold Electrode

Silver Electrode

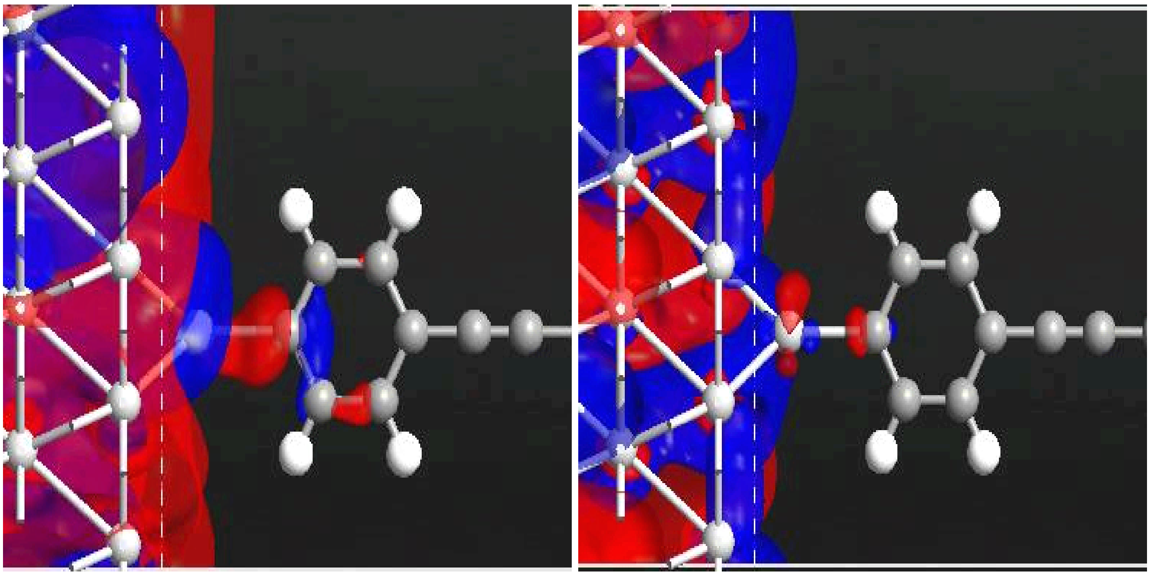

(a) HOMO Level (b) HOMO+1 Level

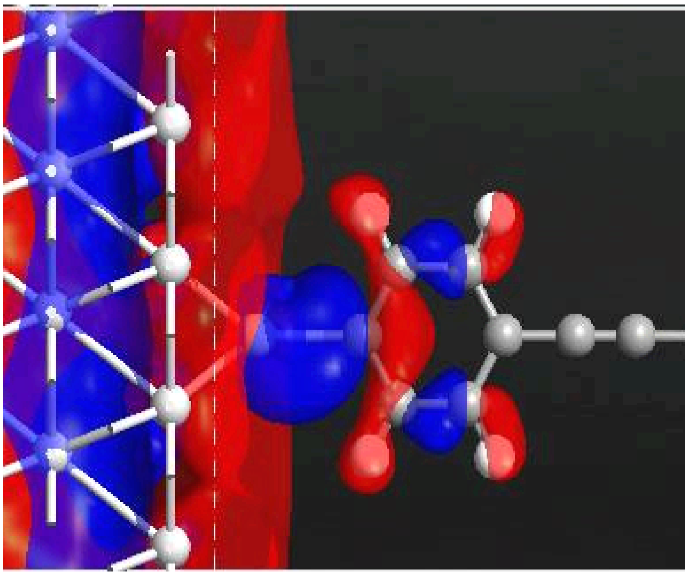

(c) HOMO+2 Level

Figure C.6: Eigen States at the left contact for Silver Electrode

Copper Electrode

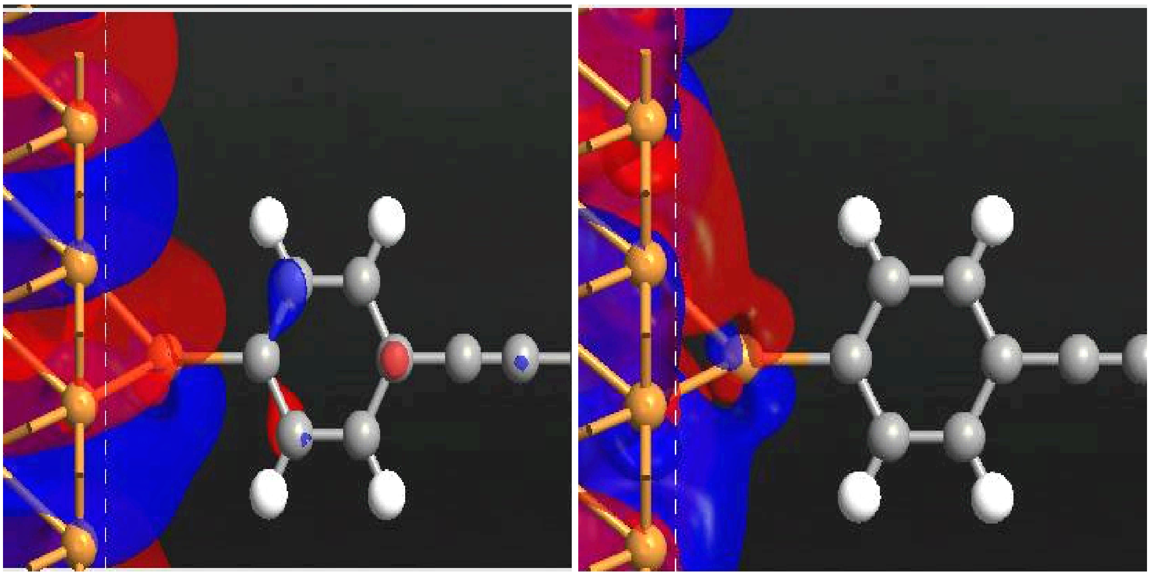

(a) HOMO Level (b) HOMO+1 Level

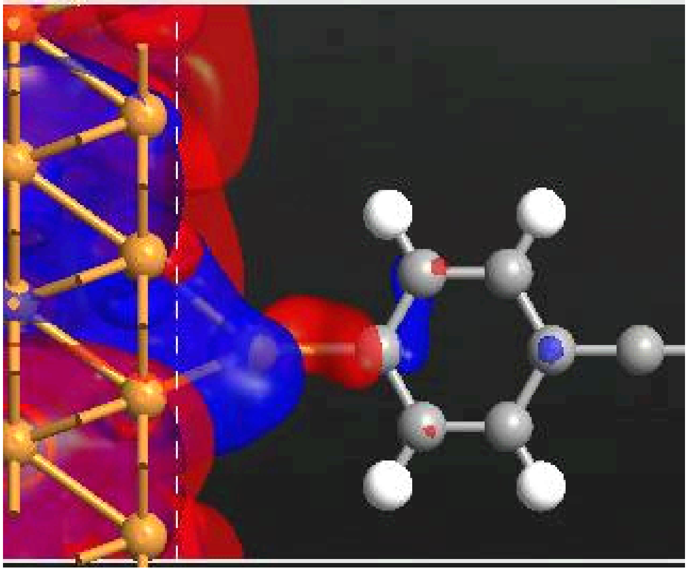

(c) HOMO+2 Level

Figure C.7: Eigen States at the left contact for Silver Electrode

1.2 2TT

Transmission Spectrum

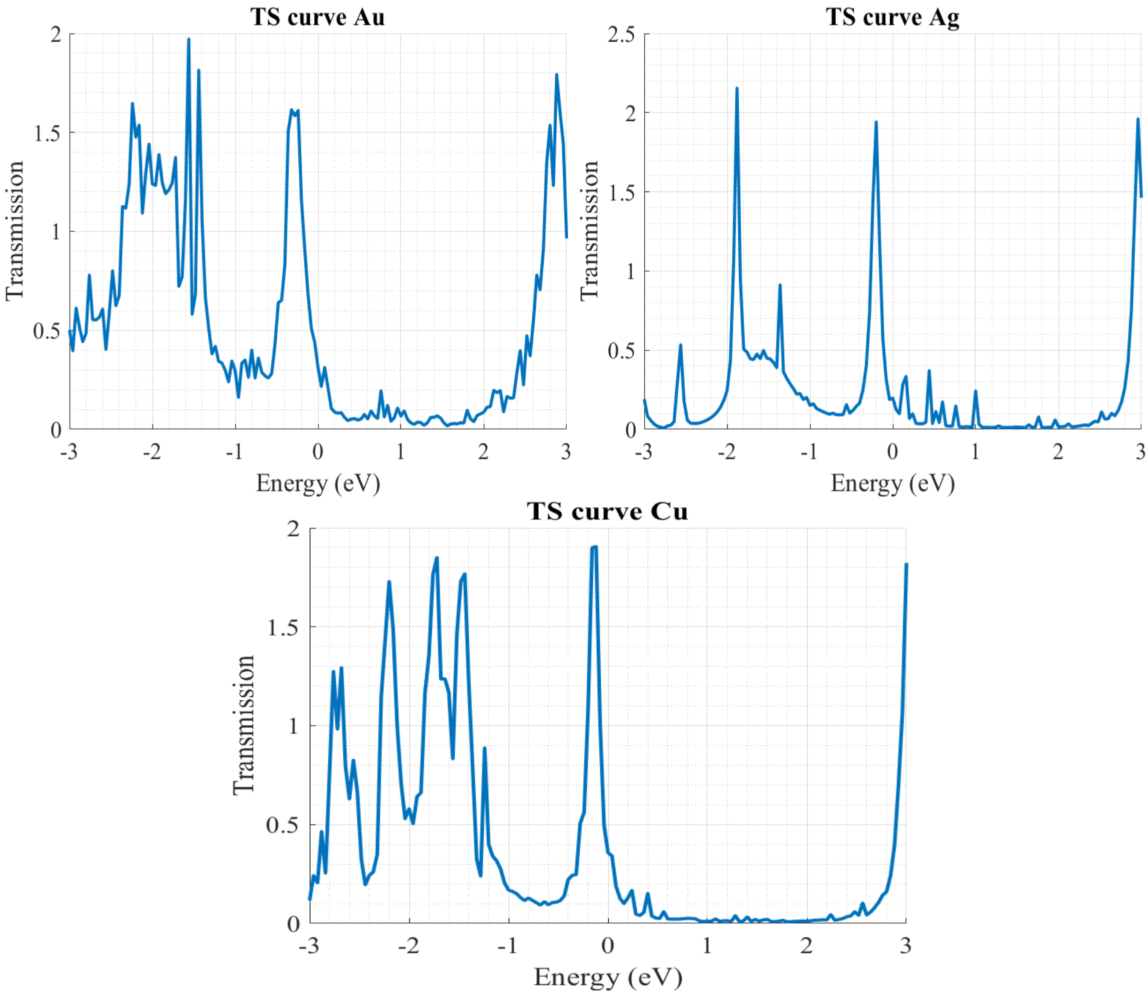

Figure C.8: Transmission Spectrum for individual metal electrodes gold(a), silver(b), copper(c)

Orbitals

At 0.6V

Gold Electrodes

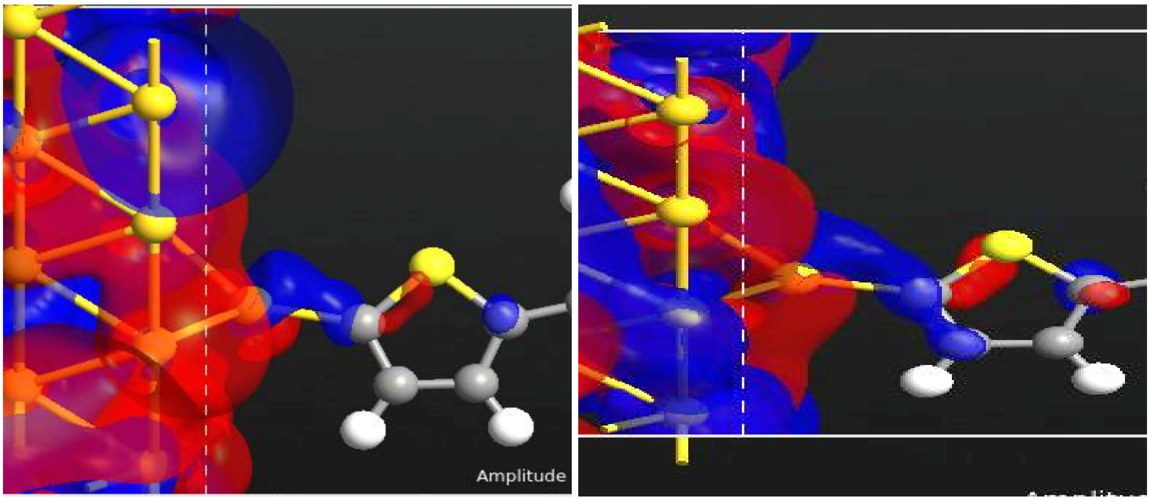

(a) HOMO Level (b) HOMO+1 Level

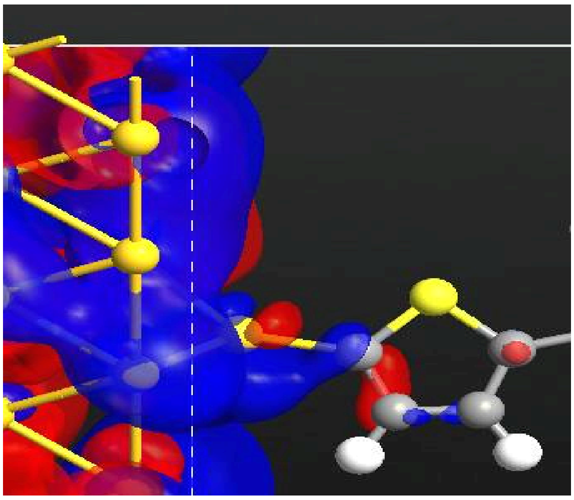

(c) HOMO+2 Level

Figure C.9: Eigen States at the left contact for Gold Electrode

Silver Electrodes

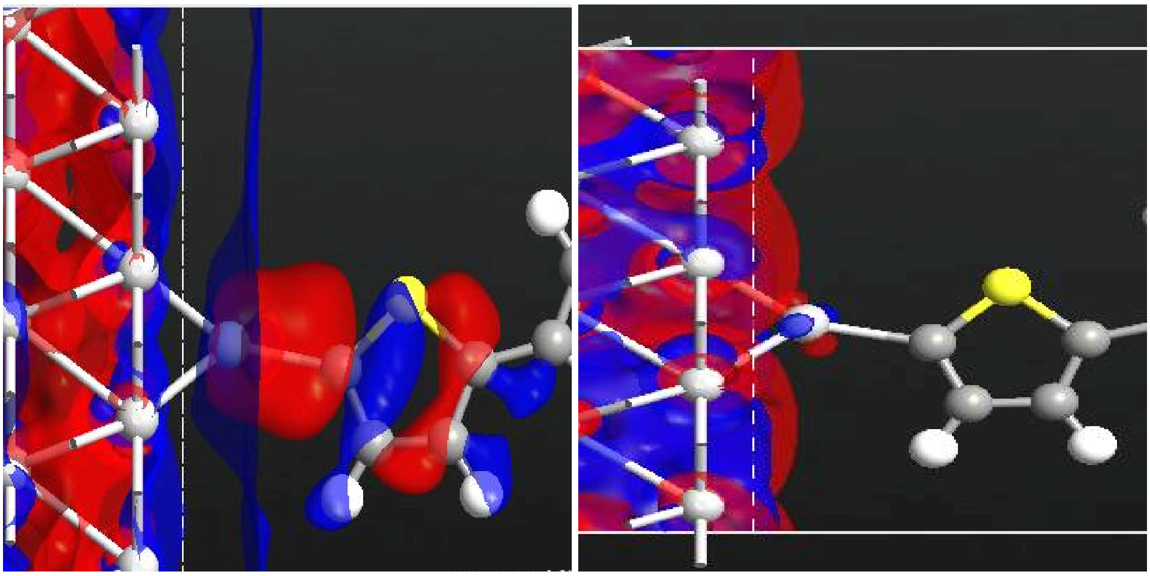

(a) HOMO Level (b) HOMO+1 Level

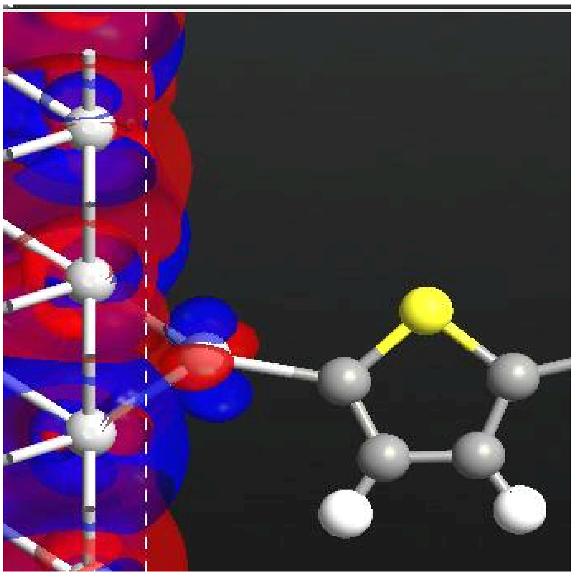

(c) HOMO+2 Level

Figure C.10: Eigen States at the left contact for Silver Electrode

Copper Electrodes

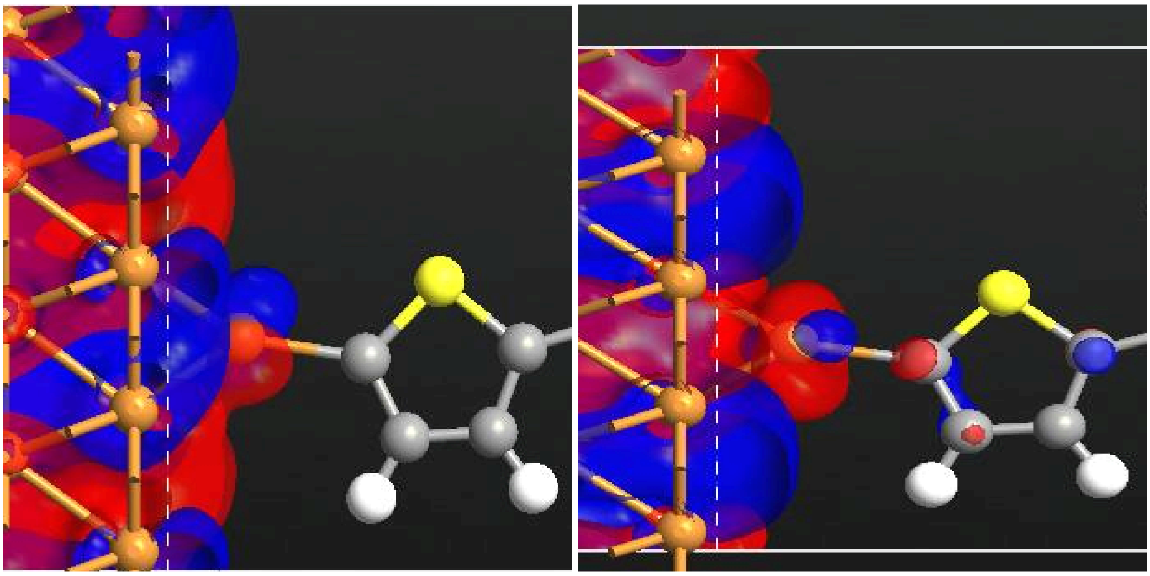

(a) HOMO Level (b) HOMO+1 Level

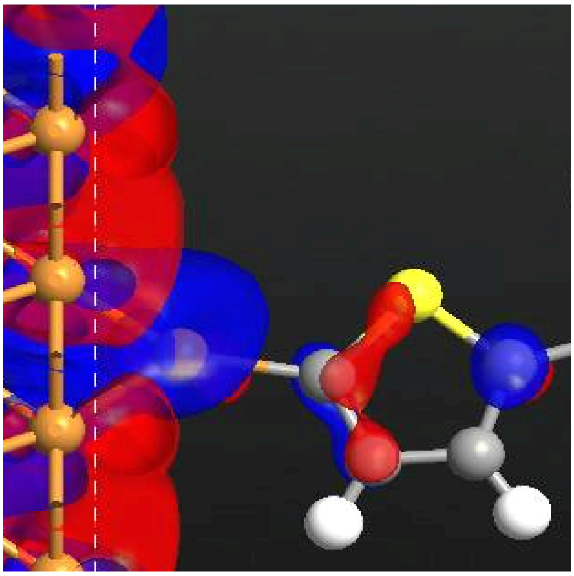

(c) HOMO+2 Level

Figure C.11: Eigen States at the left contact for Copper Electrode

At 1.2V

Gold Electrode

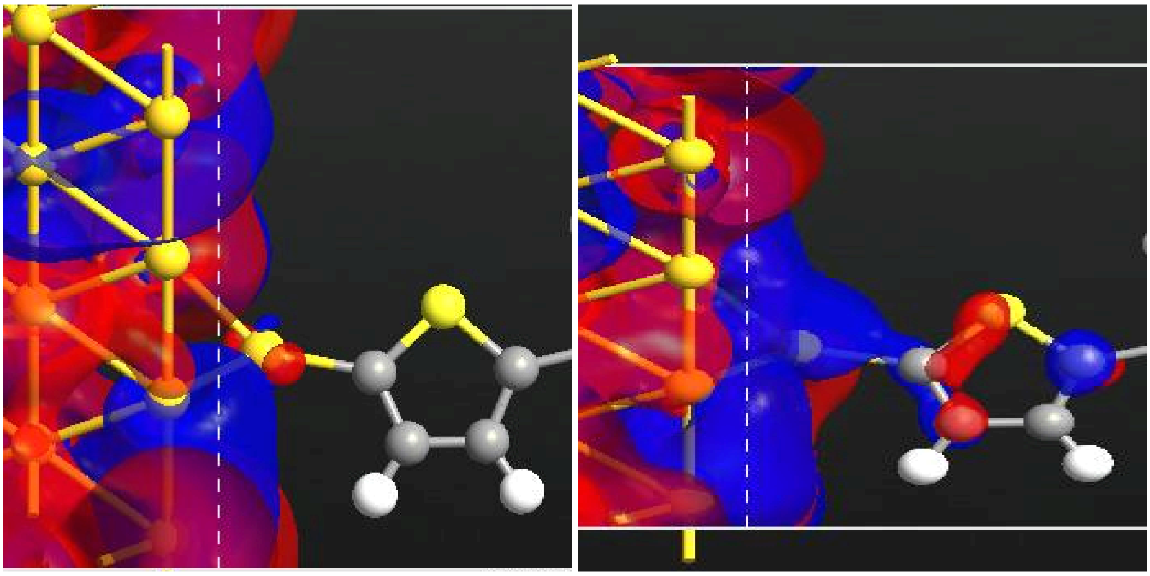

(a) HOMO Level (b) HOMO+1 Level

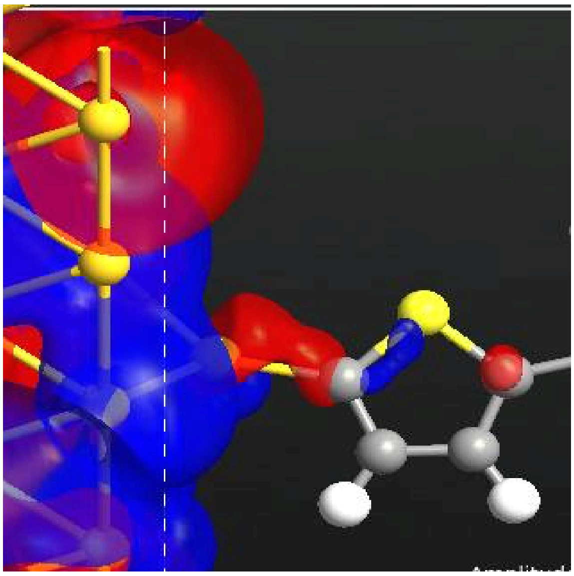

(c) HOMO+2 Level

Figure C.12: Eigen States at the left contact for Gold Electrode

Silver Electrode

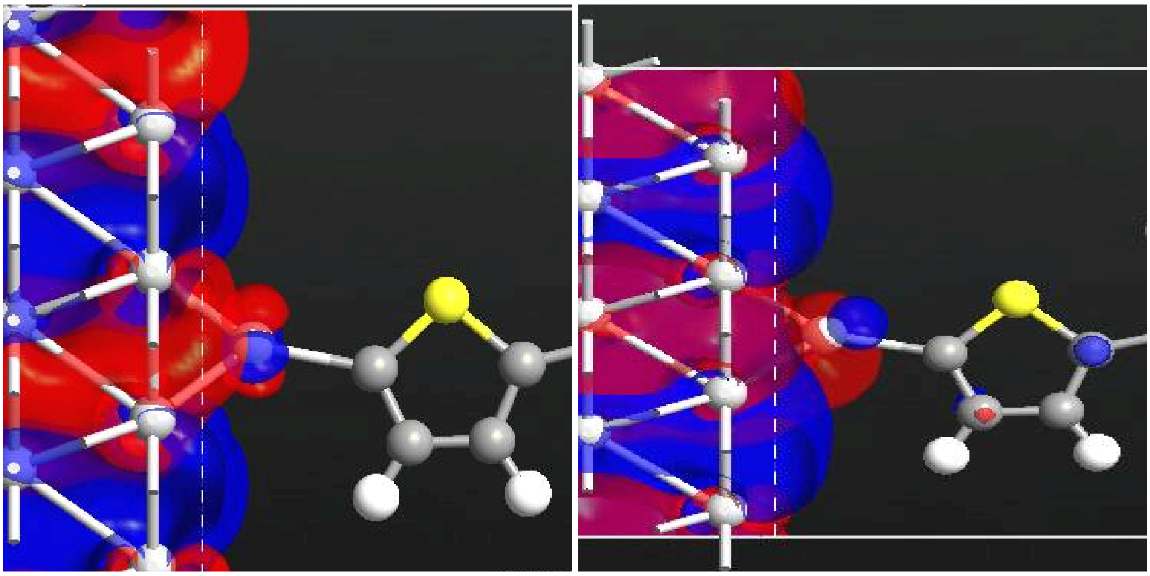

(a) HOMO Level (b) HOMO+1 Level

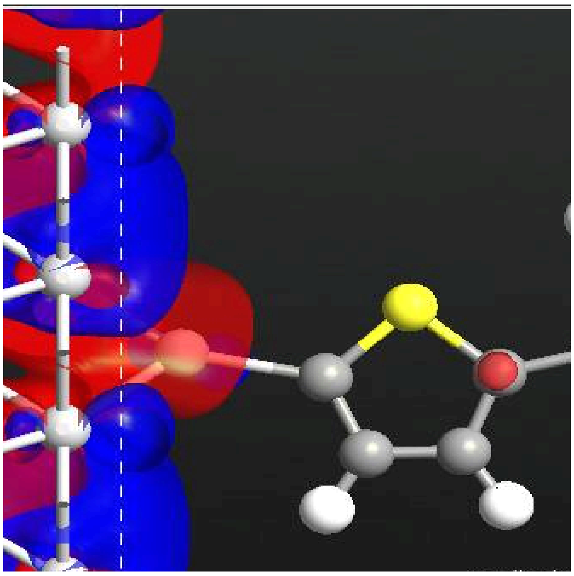

(c) HOMO+2 Level

Figure C.13: Eigen States at the left contact for Silver Electrode

Copper Electrode

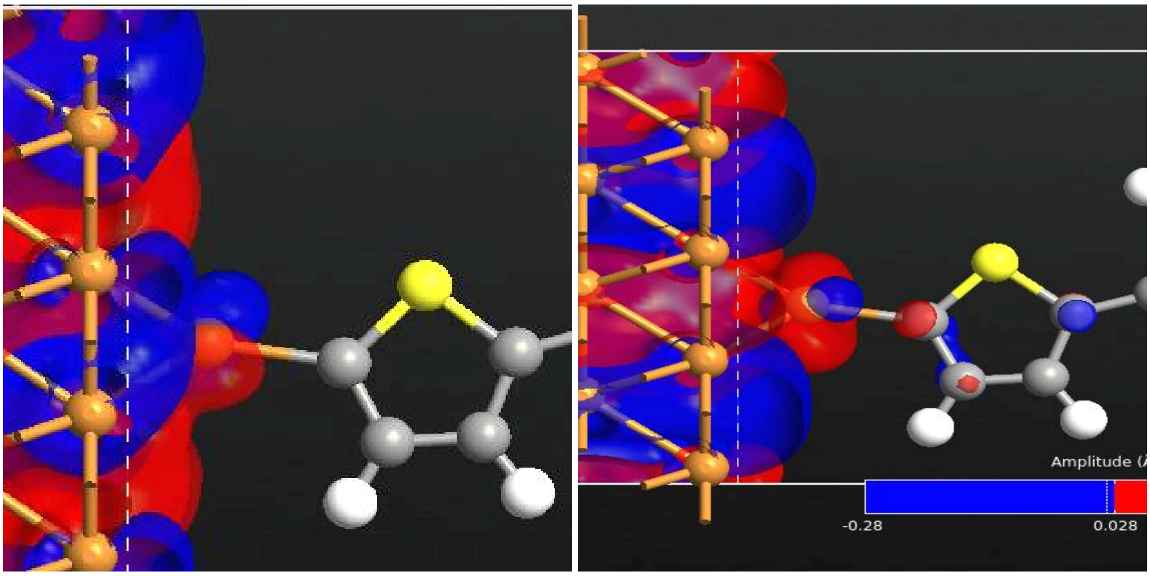

(a) HOMO Level (b) HOMO+1 Level

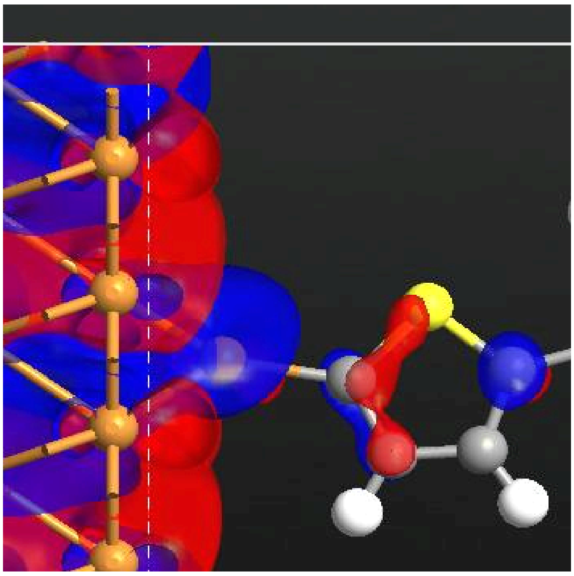

(c) HOMO+2 Level

Figure C.14: Eigen States at the left contact for Copper Electrode

2 Graphene-based Electrodes

2.1 OPE3

PDOS

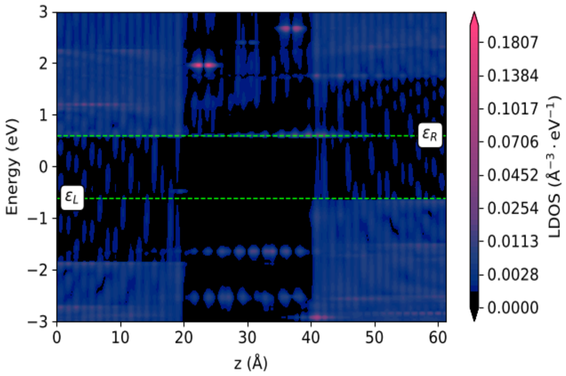

Figure C.15: PDOS for GNS Electrodes for a bias of 1.2V

2.2 2TT

PDOS

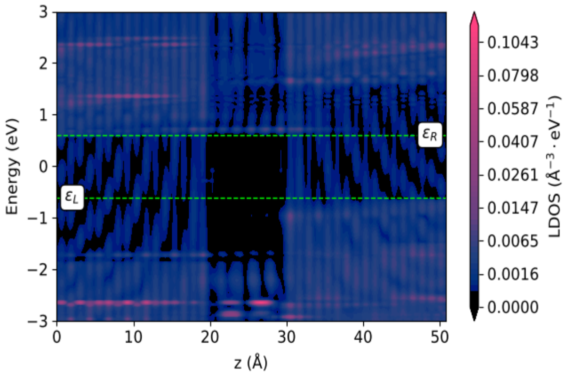

Figure C.16: PDOS for GNS Electrodes for a bias of 1.2V